

https://dspace.org/

Effects of diamond grain size on magnetic properties of the cobalt phase in PCD compacts

Ngwekhulu, Tsholofelo Themba

2018

https://hdl.handle.net/10539/27232

Ngwekhulu, Tsholofelo Themba (2018) Effects of diamond grain size on magnetic properties of the cobalt phase in PCD compacts, University of the Witwatersrand, Johannesburg, <http://hdl.handle.net/10539/27232>

Downloaded from a DSpace repository. https://dspace.org/

EFFECTS OF DIAMOND GRAIN SIZE ON MAGNETIC PROPERTIES OF THE COBALT PHASE IN PCD COMPACTS

By

Tsholofelo Themba Ngwekhulu

A Dissertation submitted to the Faculty of Science, University of the Witwatersrand, Johannesburg, in fulfilment of the requirements for the degree of Master of Science (Physics)

October 2018

DECLARATION

I declare that this dissertation is my own, unaided work. It is being submitted for the Degree of Master of Science at the University of Witwatersrand, Johannesburg. It has not been submitted before for any degree or examination in any other University.

Tsholofelo Themba Ngwekhulu

---------- day of----------2018

DEDICATION

I dedicate this work to my lovely wife Morakana, kids and my mother Joyce. Your support is greatly appreciated thank you.

I love you all

ABSTRACT

This research was aimed at a broad description of polycrystalline diamond (PCD) compacts sintering and effects of metal sintering aid infiltration into PCD. It concerned an investigation into the influence of diamond grain size on metal phase magnetic properties in PCD. In particular, a relationship between magnetic parameters and PCD microstructure has been investigated.

The polycrystalline diamond (PCD) table utilized for investigation comprised diamond grains, which were non-magnetic, a metal phase (cobalt), which was the only ferromagnetic part in the material and WC which was non-magnetic and which moved into PCD during cobalt infiltration. Sintered PCD compacts having mean grain sizes of 4.5 μm, 13 μm and 25.3 μm were assessed respectively. The PCD tables without the substrate material were prepared by Electron Discharge Machining (EDM) and characterized by means of Scanning Electron Microscopy (SEM), Image Analysis (IA) and Inductively Coupled Plasma Atomic Emission Spectroscopy (ICP-AES). Magnetic saturation and coercive field strengths were resolved using KOERZIMAT 1.097 and KOERZIMAT CS 1.096 measuring systems.

Strong correlation was seen between the metal phase content and magnetic saturation and also in cobalt mean-free path and coercivity. The analysis demonstrated that the shape and size of the specimen has no impact on the magnetic saturation parameter, and further investigation showed that increasing the grain size of the non-magnetic diamond phase decreases the number of magnetic domains of a metallic cobalt phase, but increases the coercive force. In WC-Co coercivity is high when WC grains are fine.

The research has demonstrated that the diamond starting particle size has substantial impact on the metallic phase microstructure and magnetic properties in general. Additionally, the results demonstrated that PCD made with fine diamond particles has greater PCD density as a function of metal content in comparison to coarser diamond particles showing a higher volume fraction of metallic cobalt due to the fact that the former includes much smaller average number of contact points and thus much higher contact stresses, and furthermore has greater surface to volume ratio as well as a lower packing density. Characterisation results have demonstrated a strong correlation and showed that

changing the grain size of the non-metallic phase has significant impact on the subsequent microstructure and material properties of the PCD.

ACKNOWLEDGEMENTS

I would like to extend my sincere thanks to the following people and organisations for their valuable support, knowledge and contributions throughout this work. I have received many suggestions, criticism and guidance that lead me to the completion of this research work.

Special thanks to my supervisor **Prof S.R. Naidoo** for your mentorship throughout this research work. Without your advice and helpful suggestions this work would have been impossible. I would also like to thank you for giving me the opportunity to carry out this research under your guidance.

Many thanks go to my co-supervisors, **Prof I. Sigalas** and **Dr D.J. Whitefield**, for your guidance and encouragement to finish this work through invaluable suggestions. I thank Prof Sigalas for nagging me to write up this dissertation. Your expertise and knowledge made me believe I can exceed my expectations.

I would also like extend special thanks to Dr Humphrey Sithebe for your support and guidance. Thanks to Element Six for providing me with laboratory resources and materials used in this research.

The research funding obtained from **DST-NRF Centre of Excellence in Strong Materials** (CoE – SM) is greatly acknowledged and appreciated.

Many thanks to my colleagues at **Element Six**, Amrith, Maqhawe, and Dr Thembinkosi Shabalala for your valuable assistance, comments and laughs we shared. The material characterisation team (Itumeleng, Yvonne, Zandi, William and Maggie), I thank you for the assistance with material preparation and characterisation analysis work. You were a great team to work with.

Thanks to **Prof Dave Billing** from Wits school of Chemistry for your assistance with XRD analysis work and training. I greatly thank you for your time and effort.

To my beloved wife **Morakana**, I say thank you for your support, love, and confidence you have shown in me throughout my studies.

TABLE OF CONTENTS

DEDICATION ..... **iii**

Abstract ..... **iv**

Acknowledgements ..... **vi**

List of Figures ..... **xiii**

List of Tables ..... **xviii**

List of Abbreviations and Symbols ..... **xix**

Chapter 1 Introduction **1**

1.1. Introduction 1

Chapter 2 Literature review **4**

2.1. History and Properties of Diamond 4

2.2. Structure & Properties of Diamond 5

2.2.1. Crystallographic structure of diamond 5

2.2.2. The Diamond Crystallization of (The Carbon Phase Diagram) 5

2.2.3. Diamond/graphite equilibrium line 7

2.2.4. Physical Properties of Diamond and Graphite 8

2.2.5. Chemical Properties of Diamond 9

2.2.6. Elastic properties of Diamond 9

2.2.7. Mechanical Properties of Diamond and PDC 9

2.3. Synthesis of Diamond 10

2.4. Polycrystalline Diamond Compacts (PDC) 10

2.4.1. Early development of PDC compacts 11

2.4.2. Industrial applications of PCD compacts 12

2.5. Mechanisms Involved in PDC Manufacturing Process 12

2.5.1. Diamond Powder Quality 12

2.5.2. PDC Sintering 14

2.6. Liquid Phase Sintering and Metal Phase Infiltration in PCD Compacts 24

2.6.1. Liquid Phase Sintering overview 24

2.6.2. Primary re-arrangement 26

2.6.3. Solution re-precipitation (Secondary re-arrangement) 26

2.6.4. Final pore removal, and coarsening 27
2.6.5. Liquid phase sintering typical microstructure 28
2.6.6. Contact angle in liquid phase sintering of PCD 28
2.6.7. Dihedral Angle in Liquid phase sintering 29
2.6.8. Volume Fraction in LPS 30
2.6.9. Grain Shape 30
2.6.10. Contiguity in LPS 31
2.6.11. Metal phase Infiltration (spreading and rearrangement) 32
2.6.12. Cobalt mean free path 34
2.6.13. Effect of the cobalt content in PCD 35
2.6.14. Grain boundary, inclusions and dislocations in PCD structures 35
2.7. Mechanical properties of PCD 36
2.7.1. Transverse Rupture Strength 36
2.7.2. Hardness of PCD 37
2.7.3. Density 38
2.7.4. Fracture toughness (K_{1C}) 38
2.8. Relationship of structure to properties in polycrystalline diamond 39
2.8.1. Influence of particle size on the strength of PCD materials 39
2.8.2. Effect of particle size distribution on the strength of PCD materials 40
2.8.3. Effect of microstructural homogeneity on the strength of PCD materials 40
2.9. Magnetism 40
2.9.1. Different types of magnetism 41
2.9.2. Magnetic Dipoles 44
2.9.3. Ferromagnetism 44
2.9.4. The Temperature Influence on Magnetic Behaviour 45
2.9.5. Magnetic Saturation 46
2.10. Coercivity 46
2.11. Magnetic Domains 49
2.11.1. Development of domain theory 49
2.11.2. Domain Structure 50
2.11.3. Domain Size 51
2.11.4. The Grain Structure 52
2.12. Cobalt 52
2.12.1. Ancient History of Cobalt 52

2.12.2. Metallic Cobalt and Cobalt alloys 52
2.12.3. Physical properties of Cobalt.....53
2.12.4. Chemical Properties of cobalt 54
2.12.5. Composition of Cobalt material 54
2.12.6. Production of Cobalt.....55
2.12.7. Magnetic properties of Cobalt 56
2.12.8. Applications of cobalt 57
2.13. Material Characterization of PCD 58
2.13.1. Scanning electron microscope (SEM) 58
2.13.2. Scanning Process and Image Formation 59
2.13.3. Detection of Secondary Electrons 60
2.13.4. Detection of Backscattered Electrons 60
2.13.5. X-Ray Diffraction Technique 61

Chapter 3 Research Objectives 62

3.1. Main Objective.....62
3.2. Detailed Objectives:.....62
3.3. Important Questions 62
3.4. Hypotheses 63

Chapter 4 Experimental methodology 64

4.1. Starting powders composition and their characterization 64
4.1.1. Constituents diamond powder composition 64
4.1.2. Mixed Diamond Powder Ratios 64
4.2. Precomposite assembly and Synthesis of PCD compacts 65
4.2.1. Pre-composite assembly and outgassing.....65
4.2.2. Capsule Assembly 65
4.2.3. Sintering.....65
4.3. Sintered PCD compact processing.....66
4.4. Sintered PCD Characterisation 67
4.4.1. Sample Preparation (EDM Cutting and Polishing) 67
4.4.2. Scanning Electron Microscopy (SEM).....67
4.4.3. Image Analysis.....67
4.4.4. Powder X-Ray Diffraction (PXRD) analysis.....67
4.4.5. Magnetic Properties Facility Set-up and Measurement Method 69

4.4.6. Determination of Density 71
4.4.7. Derivation of Metal Content of PCD 71

Chapter 5 Experimental Results 72

5.1. Constituents Diamond Powder Characterization 72
5.3. Resultant product after sintering 77
5.4. Characterisation of sintered PCD compacts 77
5.4.1. Micrographs of sintered PCD compacts 77
5.4.2. Image Analysis Results 78
5.4.3. X-Ray Diffraction Results of sintered PCD disks 78
5.4.4. Cobalt and tungsten content analysis measured by ICP 79
5.4.5. Metal phase content 79
5.4.6. Dissolved Tungsten content 80
5.4.7. Graphical representation of grain size and tungsten. 81
5.4.8. Magnetic Properties results 81
5.4.9. Saturation Magnetization 82
5.4.10. Coercive Field Strength 82
5.4.11. Density Measurements Results 83

Chapter 6 Discussion of results 85

6.1. Introduction 85
6.2. Characterization of diamond powders 85
6.2.1. Diamond charge mixes and grade selection 85
6.2.2. Characterization of sintered PCD 86
6.2.3. Grain Size vs Magnetic saturation 89
6.2.4. Relationship between grain size and coercivity 91
6.2.5. Correlation between grain size and Cobalt content 91
6.2.6. Comparison of metal phase MFP and coercivity 92
6.2.7. Comparison of MFP and Grain Size of PCD 93
6.2.8. MFP versus Co (IA) 94
6.2.9. Magnetic Saturation versus Co content 95
6.2.10. The XRD analysis 96
6.2.11. Interrelationship of test results to microstructure of the material 97
6.3. Structure and Magnetism 98

6.3.1. Correlation between the coercivity and the grain size measured by SEM image analysis. 99
6.3.2. Relationship of microstructure to average grain size of diamond 99
6.3.3. Magnetic coercivity vs cobalt content 101
6.3.4. Image Analysis results 102

Chapter 7 Conclusion 104

References 107

LIST OF FIGURES

Figure 1: The figure shows complete PDC [10]. 2

Figure 2: Correlation of the crystal structures of zinc blende with wurtzite [15]. 5

Figure 3: Phase diagram of carbon and graphite [18].....6

Figure 4: Schematic diagram of the direct conversion of graphite to diamond [19]. 7

Figure 5: Catalytic HPHT Synthesis [18]. 8

Figure 6: Early PDC diamond layer and substrate [26].....11

Figure 7: Schematic diagram showing the relationship between the grain size of diamond before and after sintering [10]. 13

Figure 8: PDC sintering schematic trajectory [29].....14

Figure 9: Selective dissolution of diamond grains in infiltrating Co causing.....15

Figure 10: Diagram of the sintering of PDC materials [30]. 16

Figure 11: SEM micrographs of a polished section showing interface and bulk of PCD [10].....17

Figure 12: Representation of process taking place during cold compaction [11].....18

Figure 13: Graph representation of densification taking place during cold compaction [29]. 19

Figure 14: Illustration of rearrangement and fragmentation of polycrystalline particles leading to secondary rearrangement [29]. 19

Figure 15: Schematic representation of diamond grains deformation under HPHT [29]. 20

Figure 16: Porosity versus temperature during hot compaction at 5.5GPa [29].....21

Figure 17: Pore size change during hot compaction as temperature is increased which maintain pressure at 5.5GPa [29]. 22

Figure 18: Change in specific resistance of diamond compacts with sintering temperature [29].....23
Figure 19: Micrograph of ceramic material sintering stages process when temperature increases. Left: Initial stage sintering, middle: Microstructure after sintering for two hours at 1250°C (Less porosity than initial stage), and right: the microstructure after sintering for two hours at 1450°C [32].....23
Figure 20: Critical Parameters and Processes in Liquid Phase Sintering [29].....25
Figure 21: Contact angle in a solid/liquid/vapour system space [42].....29
Figure 22: Figure of dihedral angle in a solid/liquid system [42].....30
Figure 23: Grain shape change as fully density is reached during LPS [31].....31
Figure 24: Phase diagram showing cobalt melt line and LPS of PCD sintered Structures [18].....33
Figure 25: Microstructure changes during conventional sintering, starting from mixed powders to fully dense sintered compact [31].....34
Figure 26: Cobalt content in PCD layers as a function of grain size [35].....35
Figure 27: TRS of Polycrystalline Diamond layers as a function of grain size [25].....37
Figure 28: Diagram of PCD test specimen used for fracture toughness test [35].....39
Figure 29: Schematic diagram of showing atomic dipole structure with/without an external magnetic field for a paramagnetic material [51].....42
Figure 30: Schematic illustration of the flux density *B* against the magnetic field strength *H* for diamagnetic and paramagnetic materials [51].....43
Figure 31: Schematic diagram of the mutual configuration of atomic dipoles for a ferromagnetic material [51].....45
Figure 32: The area contained within the hysteresis loop has energy units and denotes the energy consumed during one complete reversal of the magnetization and

back. A large hysteresis loop is desirable in hard permanent magnets, while the opposite applies to electrical transformer cores [60]. 48
Figure 33: Alignment of domains in metals (a) before magnetization and (b) after magnetization [62]. 49
Figure 34: Flow diagram of the production of cobalt powders and granules [69]. 56
Figure 35: Influence of grain size and Co content on the abrasion resistance of WC-Co [69]. 57
Figure 36: Schematic representation of an SEM [79]. 59
Figure 37: Malvern Mastersizer 2000 for particle size analysis. 64
Figure 38: Process steps during sintering [47]. 66
Figure 39: PXRD D2 phaser Bruker desktop [81]. 68
Figure 40: Magnetic Saturation Measuring Equipment Components. 69
Figure 41: Components of coercivity Measurement equipment. 70
Figure 42: Constituent Diamond Grade PSD. 72
Figure 43: Micrographs of (a) G02, (b) G04, (c) G06, (d) G12, (e) G22, and (f) G30 constituent grades. 73
Figure 44: Particle size distribution of spherical cobalt. 74
Figure 45: Micrographs of spherical cobalt. 74
Figure 46: PSD of 3 different mixed diamond powders. 75
Figure 47: Micrographs of fine ((a) and (b)), medium ((c) and (d)) and coarse ((e) and (f)) diamond powders. These micrographs were captured at 1000x and 2000x magnification respectively for each size. 76
Figure 48: Sintered PCD compact. 77
Figure 49: XRD spectrums of fine, medium, and coarse grain diamond tables. 79
Figure 50: Cobalt content given by ICP in Wt % versus diamond grain size. 80
Figure 51: Dissolved Tungsten content in PCD of each variant given by ICP in wt%. 81

Figure 52: Saturation magnet versus grain size of each variant. 82
Figure 53: Coercivity results versus grain size of each variant. 82
Figure 54: Grain size versus Co content from derived densities. This includes the effect of heavy WC in the PCD table as were clearly shown by XRD analysis. 84
Figure 55: Micrograph of fully sintered PCD compact [10].....87
Figure 56: XRD Spectrum of all three diamond powders.....88
Figure 57: Relationship between magnetic saturation and diamond grain size after sintering. 90
Figure 58: Relationship between coercivity and diamond grain size after sintering. 91
Figure 59: Relationship between ICP, IA and derived cobalt content and diamond grain size after sintering. The derived value was calculated using Archimedes immersion density values. 92
Figure 60: Correlation of coercivity and Co mean free path (MFP) (µm). 93
Figure 61: Relationship between MFP and diamond grain size. 94
Figure 62: Relationship between MFP and Co (IA) content after sintering. 95
Figure 63: Relationship between magnetic saturation and ICP cobalt content after sintering. 96
Figure 64: Relationship between coercivity and diamond grain size after sintering. 98
Figure 65: Relationship between coercivity and image analysis diamond grain size after sintering. 99
Figure 66: The relationship between cobalt calculated by IA and diamond grain size after sintering. 100
Figure 67: Influence of the composition of the metal binder on the porosity and the volume fraction of the binder of the (W,Ti)C–Co and (W,Ti)C–Ni cemented carbides [86].....101

Figure 68: Relationship between coercivity and cobalt content from ICP after sintering. 102

LIST OF TABLES

Table 1: Physical properties of diamond and graphite at standard temperature and pressure....8
Table 2: Diamond and graphite structural properties [14]....9
Table 3: Elastic properties of diamond. 9
Table 4: Properties of diamond and PCD [22]. 10
Table 5: XRD parameters used to analyse the samples....68
Table 6: Constituent Diamond Powder particle size distribution. 72
Table 7: Diamond Powder Particle sizes Composition. 75
Table 8: Image Analysis results of PCD 78
Table 9: Cobalt phase content as a function of grain size 79
Table 10: Tungsten phase content as a function of grain size....80
Table 11: Summary of magnetic properties of each variant 81
Table 12: Density measurements results 83
Table 13: Summary of magnetic properties of PCD tables. 97

LIST OF ABBREVIATIONS AND SYMBOLS

PCD	=	Polycrystalline Diamond
PDC	=	Polycrystalline diamond compact
SEM	=	Scanning Electron Microscopy
XRD	=	X-Ray Diffraction
GPa	=	gigapascal
HPHT	=	high pressure, high temperature
MPa	=	mega Pascal
Pa	=	Pascal
UHP	=	ultra-high pressure
IA	=	image analysis
EDM	=	electrical discharge machine
θ	=	theta
ρ	=	density
μ	=	mu
μm	=	micrometre
OD	=	Outside Diameter
NDT	=	Non Destructive Testing
LPS	=	Liquid Phase Sintering
LP	=	Liquid Phase
LMP	=	Liquid Metallic phase
hcp	=	hexagonal close packed
FCC	=	face-centred cubic
cBN	=	cubic boron nitride
PCBN	=	polycrystalline cubic boron nitride
XRF	=	X-Ray Fluorescence
DRL	=	Diamond Research Lab
EDS	=	Electrical Dispersive Spectroscopy
FWHM	=	Full Width at half Maximum
WC	=	Tungsten Carbide
Mag Sat	=	Magnetic Saturation
SAIP	=	South African Institute of Physics

CHAPTER 1 INTRODUCTION

1.1. Introduction

Diamond has been known for more than 3000 years, and it is valued for its cosmetic magnificent appearance subsequent to polishing. It has the largest electronic energy gap among the group IV elemental semiconductors. Its introduction into industrial applications required understanding of a broad range of properties, for example, thermal expansion coefficient, thermal conductivity, hardness and chemical affinity for other elements. This learning information was utilized as part of the making of diamond composites with other materials [1].

Diamond tools of different shapes and sizes are harder to produce simply from cutting and forming of diamond, as a result of its high hardness. The Vickers hardness of diamond is more than 40 GPa and consequently it is known as a "Super hard" material [2]. The high hardness of this material can be ascribed to the highly directional covalent bonds by which the carbon atoms are held together and additionally to the high density of these bonds. Capitalizing on these properties and in particular on the hardness of diamond, grit of this material was combined with a metallic “bond” phase to make diamond grinding wheels and diamond saw segments. These are used extensively in stone working and metal grinding. Taking this process further, fine diamond particles were sintered together at High Pressures and High Temperatures (HPHT) with the help of a metallic Liquid Phase Sintering (LPS) to produce Polycrystalline Diamond Compact (PDC) in which diamond is the majority phase and residual metal from the LPS process is the minority one. The resulting compacts have easier shape flexibility, and in addition increased fracture toughness when compared to single crystalline diamond.

On the other hand, excessive amounts of the cobalt phase in the sintered PDC cause the physical properties of the sintered compact to deteriorate at temperatures exceeding 700 ^{o}C [3] because of diamond catalytic graphitization. Micro-cracking and chipping occur because of the thermal stress generated by the difference between thermal expansion coefficients of diamond and the residual cobalt phase [4-6]. Development and application of PDC has generated a strong drive to overcome complex problems related to dependably mounting PDC on a drill bit and to accelerated thermal wear during application.

In this work, liquid phase sintering was employed with cobalt acting as a LPS aid to progress direct bonding of the diamond grains [5]. The result of this process was PDC which was the primary object of the investigation of this research work.

PDC cutters have fundamentally added to the enormously enhanced economics and efficiencies of the oil and gas drilling industry for over 40 years and continue to be an integral part of modern technology. Since its introduction in the 1970's, PDC is widely used in the oil and gas industry for rock drilling. It is additionally utilized broadly as part of the manufacturing industry in applications, for example, non-ferrous metal drilling and machining [7-9]. The figure below shows sintered PDC cutters of different sizes.



Figure 1: The figure shows complete PDC [10].

The substrates in Figure 1 provide backing for the diamond layer and allows the compact to be attached to a bit through brazing. Furthermore, the cobalt phase melts from the substrates when the temperature reaches that of melting point of Co and infiltrates the diamond powder, and expediting the diamond-to-diamond intergrowth by improving the bonding kinetics between grains.

PCD compacts are ferromagnetic at room temperature due to the presence of the fcc cobalt metallic phase in both the PCD and the WC-Co substrate. This property is valuable in Non-Destructive Testing (NDT) of a PCD compact as it gives data that relates to the

microstructure of the material. The same applies to the substrate, for which the magnetic saturation and coercivity are measured. PCD disks are typically cut and prepared into different shapes and dimensions for the particular applications by laser cutting and EDM (Electrical Discharge Machining) cutting. This will allow the characterization of PCD with ease as well as the impact different grades of diamond powder have on magnetic saturation and coercivity of cobalt phase after sintering which are the objectives of this study.

This dissertation starts with a review of diamond and PCD compacts, which will be introduced in Chapter 2 and furthermore incorporates the step by step clarification of PCD sintering process. The research objectives are summarized in Chapter 3. Chapter 4 presents experimental techniques and the equipment used. The results of the investigation are detailed in Chapter 5 and the discussion of results and the relationships of various parameters that were correlated and attempt to model results follow in Chapter 6. Conclusion and future work suggestions are included in Chapter 7 with the references in Chapter 8.

CHAPTER 2 LITERATURE REVIEW

2.1. History and Properties of Diamond

Diamond has been perceived as having exceptional properties for a few thousand years. Traces of it being utilized in industry as a tool can be followed back to 300 BC. During that time, diamond stones were used for etching. In 150 BC, early deposits of diamond were found in India and an export trade was set up with China for diamond-tipped imprinting tools that were utilized in cutting hard limestone. Other applications of diamond industrialization slowly developed until 18th and 19th centuries [11].

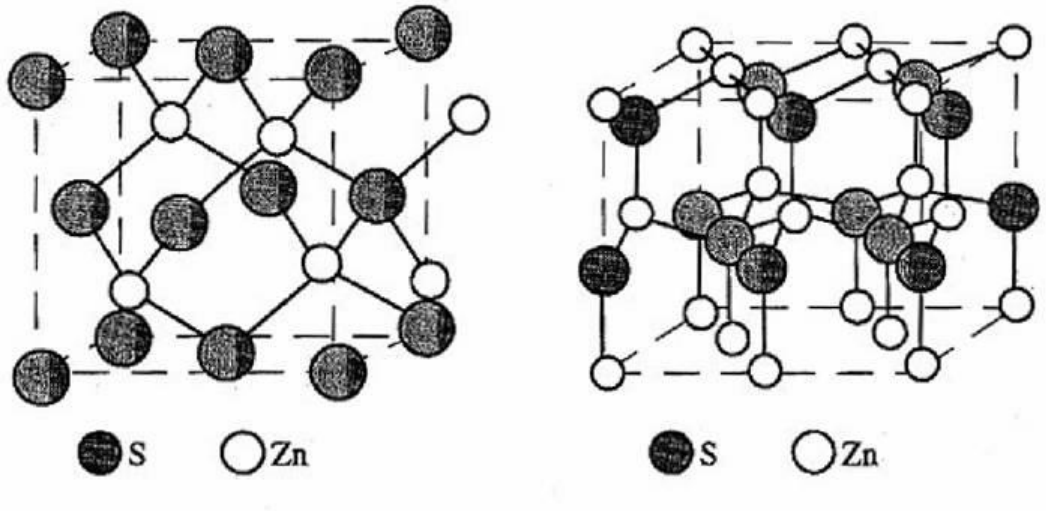
Diamond comprises light carbon atoms held together by strong covalent chemical bonds in high density. This gives rise to numerous extreme properties. The hardness of diamond is affected by its purity, crystalline perfection and orientation. Natural single crystalline type diamonds in their original as-grown form is an octahedron bounded by {111}. The superior physical and chemical properties of diamond make it a prominent engineering material suitable for scientific and technological applications. This is explained in detail in section 2.2.1 and 2.2.2 [8].

Diamond has the highest elastic modulus and thermal conductivity of all known materials. It does, however, show a few shortcomings, which are its poor fracture toughness, high chemical affinity to ferrous materials at elevated temperatures and low thermal stability past 700 °C in air. The thermal constraints and additionally the thermal conductivity of PCD are for the most part dependant on diamond grain sizes and metal phase content and the mechanical properties of PCD is dominated by the strength and quality of the diamond-diamond bonds [12]. Diamond has high thermal conductivity due to the diamond bond stiffness and the diamond structure, which give rise to a high acoustic velocity and an exceptionally high Debye temperature of θ_D = 2000 K. Since diamond is an electrical insulator, heat is conducted by lattice waves (phonons). These phonons are scattered by various mechanisms depending on temperature [13].

2.2. Structure & Properties of Diamond

2.2.1. Crystallographic structure of diamond

Carbon atoms in diamond have tetrahedral coordination, with covalent bonds between every atom and its four closest neighbours. Diamond is made up of two interpenetrating FCC lattices where the origins of two FCC sub lattices lie at (0, 0, 0) and (1/4, 1/4,1/4). This essentially forms the common zinc blende structure as shown in fig 2(a). The hexagonal wurtzite lattice structure (fig 2(b)) serves as an alternative structure and was predicted as a possible diamond polymorph by Ergun and Alexander [14].



(a) Zinc blende (b) Wurtzite

Figure 2: Correlation of the crystal structures of zinc blende with wurtzite [15].

2.2.2. The Diamond Crystallization of (The Carbon Phase Diagram)

Since Tennant explained that diamond is an allotrope of carbon in 1797 [16], numerous endeavours were undertaken to crystallize diamond using different carbonaceous starting materials. It was just a century and a half later that effective synthesis processes were demonstrated [16]. Figure 3 illustrates the carbon phase diagram showing the region of catalytic diamond HPHT synthesis. The same pressure and temperature conditions are used for the sintering of diamond powders to form PDC cutters. Figure 3 shows that graphitization is expected for the sintering parameters used in this work In this figure, it is observed that, due to the proximity to the region where graphite is stable, and that to overcome this effect a higher sintering time is necessary to reconvert graphite into diamond [17].

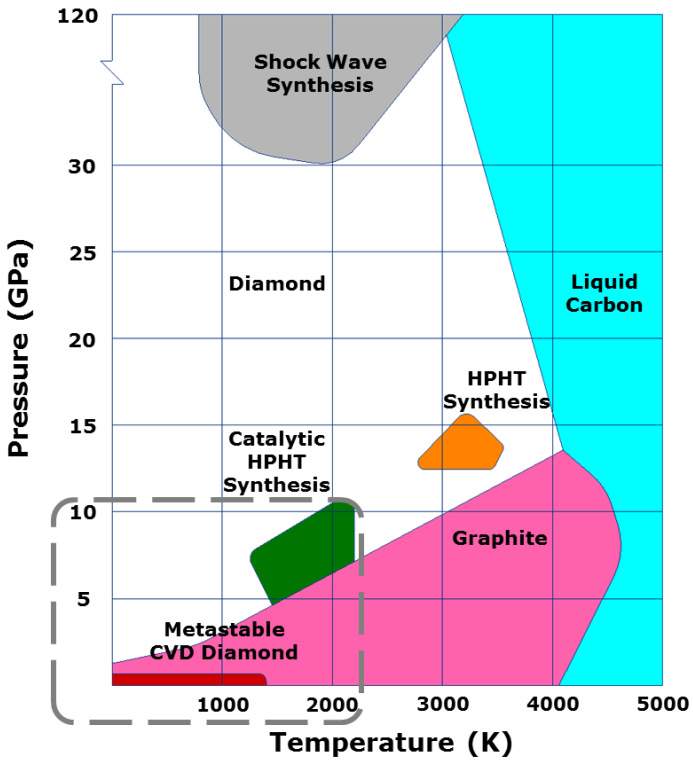


Figure 3: Phase diagram of carbon and graphite [18].

The diamond and graphite relationship is a thermodynamic and kinetic one, as it is shown on the phase diagram of carbon in Figure 3. At ordinary temperatures and pressures, diamond is a couple of electron volt (eV) less stable than graphite, and the way that diamond exists at all is because of the activation barrier for conversion between the two phases. There is no simple mechanism for this transformation thus changing diamond into graphite, or the other way around, requires as much energy as destroying the entire lattice and rebuilding it [16]. Figure 4 shows the direct conversion of graphite into diamond.

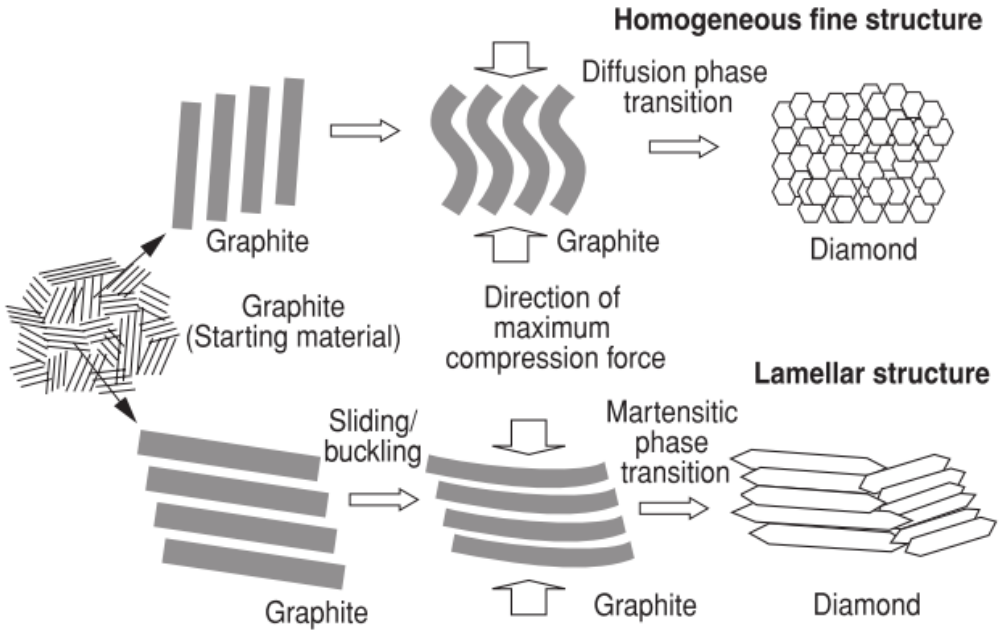


Figure 4: Schematic diagram of the direct conversion of graphite to diamond [19].

It follows that when diamond is formed it can't return to graphite at ambient conditions due to the kinetic energy of atoms which is so small compared to the energy barrier which is very high. In this case diamond is said to be metastable, since it is kinetically stable, not thermodynamically stable. Diamond is found to be the more stable of the two types of carbon [17].

2.2.3. Diamond/graphite equilibrium line

The diamond/graphite equilibrium line position has precisely been determined by the thermodynamic calculations that were measured for the physical properties of diamond and graphite in the temperature that ranges from ≈ 27 to ≈ 927 °C and by trials on synthesis or graphitization of diamond [17]

High pressures are required to permit diamond processing in its stability zone to keep any carbon parts from decaying into graphite. This is demonstrated in Figure 5 where the processing region is shown to be above the Berman Simon line in the diamond stability zone. At a pressure of 5.5 GPa, the most extreme processing temperature is roughly 1500 ºC, which is adequately over the Co – C eutectic temperature. This is the standard pressure utilized industrially to make cobalt infiltrated polycrystalline diamond.

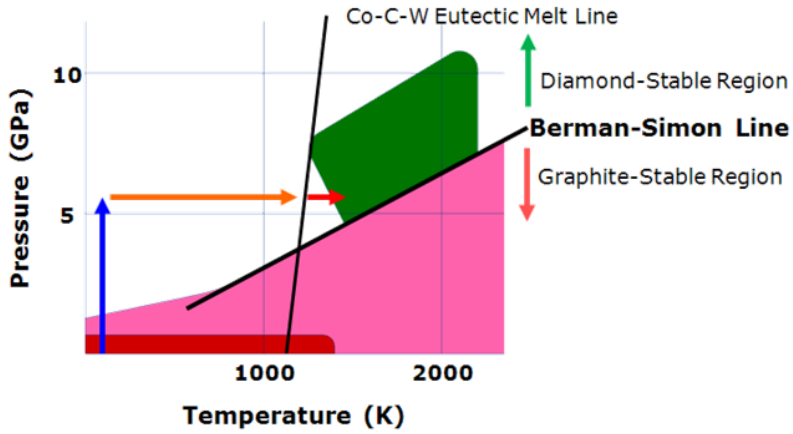


Figure 5: Catalytic HPHT Synthesis [18].

From Figure 5, the crystallization of diamond takes place above the Berman-Simon Line at 5 GPa and at a temperature of 1500 °C.

2.2.4. Physical Properties of Diamond and Graphite

Diamond is composed of carbon together with common impurities such as found in natural diamond, boron and nitrogen. Carbon atoms are bonded in diamond by sp^3 hybridized bonds which are a metastable form of carbon bond, the stable one being the sp^2 graphitic bonding [20]. These two bonding designs are amazingly distinctive and result in an extensive variety in physical and chemical properties between diamond and graphite.

Table 1: Physical properties of diamond and graphite at standard temperature and pressure

Property	**Diamond**	**Graphite**
Atomic Density (cm^{-3})	1.77×10^{23}	1.14×10^{23}
Lattice Structure	Cubic	Hexagonal
Lattice constant (Room Temperature) (nm)	0.3567	a=0.2462, c=0.6708
Bond length (nm)	0.1421	0.1545
Specific Gravity (g cm^{-3})	3.515	2.26
Band Gap (eV)	5.47	-0.04
Thermal conductivity (W/cm-K)	25	30, 0.06

Table 1 shows the properties of diamond and graphite. Diamond has significantly different properties to graphite due to its atomic structure.

Table 2: Diamond and graphite structural properties [14].

Property	Diamond Cubic	Diamond Hexagonal (Lonsdolite)	Graphite
Space Group	O^7;Fd3m	D4;$P6_3$/mmc	D4
Unit Cell Constant (nm)	Cubic a=0.357	a=0.252, c=0.412	a=0.246;c=0.671
Refractive Index	2.417	2.41-2.42	2.717 (667 nm)
Bonding	sp^3	sp^3	sp^2

2.2.5. Chemical Properties of Diamond

Diamond does not react with most forms of chemical attack for the simple reason that diamond has a tightly packed structure of carbon atoms and is therefore not attacked by acids or different chemicals with the exception of those that at high temperatures act as oxidizing agents (for example), molten potassium nitrate [14]. It does however graphitize in air above 600 ^oC, and reacts with ferrous metals.

2.2.6. Elastic properties of Diamond

Table 3 shows the elastic properties of diamond. The diamond stiffness is dependent on the grain size employed.

Table 3: Elastic properties of diamond.

Material	$E(\times 10^{11} Nm^{-2})$	$G(\times 10^{11} Nm^{-2})$	ν	$K(\times 10^{11} Nm^{-2})$
Diamond	11.41	5.53	0.07	4.42

From Table 3, the letter *E* denotes Young's modulus; *G* denotes shear modulus, *K* denotes Bulk modulus and ν is the Poisson's ratio of diamond [21].

2.2.7. Mechanical Properties of Diamond and PDC

Every processing step in the making of PDC has an impact on the mechanical properties of the final product. Accordingly, mechanical properties are utilized as quality control measurements for the PDC manufacturing process. The mechanical properties of diamond and PDC are in Table 4.

Table 4: Properties of diamond and PCD [22].

Property	Diamond	PDC
Density (g/cm^3)	3.52	4.0
Fracture Toughness (MPam$^{0.5}$)	3.4	8
Knoop Hardness (GPa)	57 - 104	50
Young's Modulus (GPa)	964	810
Thermal Expansion ($10^{-6}K^{-1}$)	1.5 – 4.8	4.6
Thermal conductivity 20°C ($Wm^{-1}K^{-1}$)	2200	760
Wear Coefficient	2.1 – 5.5	4

2.3. Synthesis of Diamond

Diamond was first synthesized by ASEA Research facility in Sweden in 1953. Though, this early achievement was never made public at the time. During the year 1954, General Electric (GE) Company which is based in the United States announced that they had successfully synthesized diamond. Later on, diamonds were synthesized at the De Beers Diamond Research Laboratory (DRL) in South Africa by transforming graphite to diamond employing HPHT technology. These three companies used a carbon solvent/metal catalyst system to overcome the high energy barrier [14].

The commercialization of industrialized diamond has been a remarkable contributor to the amazing advances which have transpired during the past 50 years in the diamond tool technology and in the variety of applications in which diamonds are utilized. The business accessibility of synthetic diamond offered two favorable circumstances. The accessibility of industrial diamond was potentially unlimited compared with the restricted amounts of the natural material and, secondly, it presented the chance of engineering diamond materials that would exhibit specific properties suited to specific industrial applications.

2.4. Polycrystalline Diamond Compacts (PDC)

The introduction of polycrystalline diamond (PDC) to the oil and gas industry in the early 1970s was a very important material development [23]. Such materials could be manufactured by changing the mechanical properties and would be utilized in a widespread range of cutting applications and as for wear resistance. PDC is mainly

utilized in the drilling and machining of non-ferrous abrasive materials. Such drilling activities include the drilling of rock in oil and gas exploration, while in machining PDC is used in the manufacturing and engineering activities for the working of aluminium alloys, reinforced plastics, new wear resistant lightweight composite materials, and wood composites [24].

PCD is a strong material because of the infiltrated cobalt content of which without it PCD would be brittle. The fracture and wear properties of single crystal diamonds are highly dependent on orientation. Diamond crystals tend to cleave easily along the (111) crystallographic plane [25]. The fracture toughness of PCD is significantly improved, in comparison to that of a single crystal diamond, by the presence of randomly oriented diamond grains. It is generally prepared under HPHT conditions similar to those used in the commercial manufacture of single crystal synthetic diamond. PCD table comprises diamond grains, which are non-magnetic, a metal phase (ferromagnetic cobalt), (ferromagnetic) and WC which is non-magnetic.

2.4.1. Early development of PDC compacts

Development of PDC was first introduced by GE in the year 1973. These cutters (a compact of diamond on a WC-Co substrate) utilized GE's earlier development of single crystal artificial diamond, to sinter a fine synthetic diamond powder into one compact. The fine powder and a tungsten carbide – cobalt (WC-Co) substrate were loaded into a pressure capsule and subjected to HPHT conditions [7]. Figure 6 illustrates a schematic of the first PDC cutters produced by GE at that time.



Figure 6: Early PDC diamond layer and substrate [26].

2.4.2. Industrial applications of PCD compacts

The recent industrialized diamond business started to expand considerably following the commercial availability of synthetic diamond in the late 1950's. This growth was driven by technological developments in the sawing, drilling and cutting tool industries.

PCD cutters find their primary use in the oil and gas drilling industry as defined edge cutting and sawing tool inserts. PDC also finds applications as wear parts because of high abrasion resistance and hardness. The result is an extended tool life allowing tight tolerances to be achieved and the capability to work efficiently at high cutting speeds and hence give high productivity levels.

PDC cutters have the ability to machine work piece materials which are challenging to machine using any other materials other than PDC. Examples of materials best machined by PCD cutting tools are: wood and wood composites, carbon fibre composites and fibre-glass, rubber and plastic as well as mineral materials, and non-ferrous alloys such as magnesium alloys, aluminium alloys, and brass and copper [27]. PDC materials are also used in automotive industries for machining engine components, gearbox components, and braking systems. They are also used in mining, but at a relatively lower volume when compared to the oil and gas exploration industry.

2.5. Mechanisms Involved in PDC Manufacturing Process

2.5.1. Diamond Powder Quality

Industrially accessible PCD composites have a material composition of up to 95% in diamond volume, with the balance being the Co phase that has infiltrated the diamond powder preform from the substrate. Consequently, the diamond powder raw material quality is extremely important when the consistency of the sintered product and the final properties are determined. Typically, the micron-sized diamond powder utilized as part of PDC assembling and synthesis is a derivative of the industrial diamond powder synthesis process, where grains of average particle sizes between 5 µm and 30 µm are produced mainly for the rock cutting market (e.g. diamond wheels, diamond saw blades, and loose diamond powder) [7].

The primary catalytic system utilized in the process of synthesizing the diamond powder is based on an iron-nickel alloy, while cobalt, originating in the WC-Co substrate, is used for the sintering of diamond powders into PCD. Diamond powder has a wide quality range available on the market. The diamond micron-sized powders utilized in the sintering process are normally prepared by crushing coarser diamond crystals; the initial industrial powder quality affects the quality of the shear cutter raw material powders. Other quality issues concern the diamond powder extraction and cleaning process from the solidified alloy catalyst in which synthesis occurred.

Earlier researchers [28] reported that the grain size of diamond becomes smaller after sintering in the absence of metallic sintering aid and at room temperature. They attribute this phenomenon to crushing of the starting powders by friction among the particles during the pressure-rise stage. To confirm this, diamond particles were observed after pressing at 5.5 GPa. As shown in Figure 7, all powder sizes used in the test were crushed down. The crushing was particularly remarkable in coarser grades and a larger number of crushed fine particles smaller than 1 μm were observed in the crashed powders.

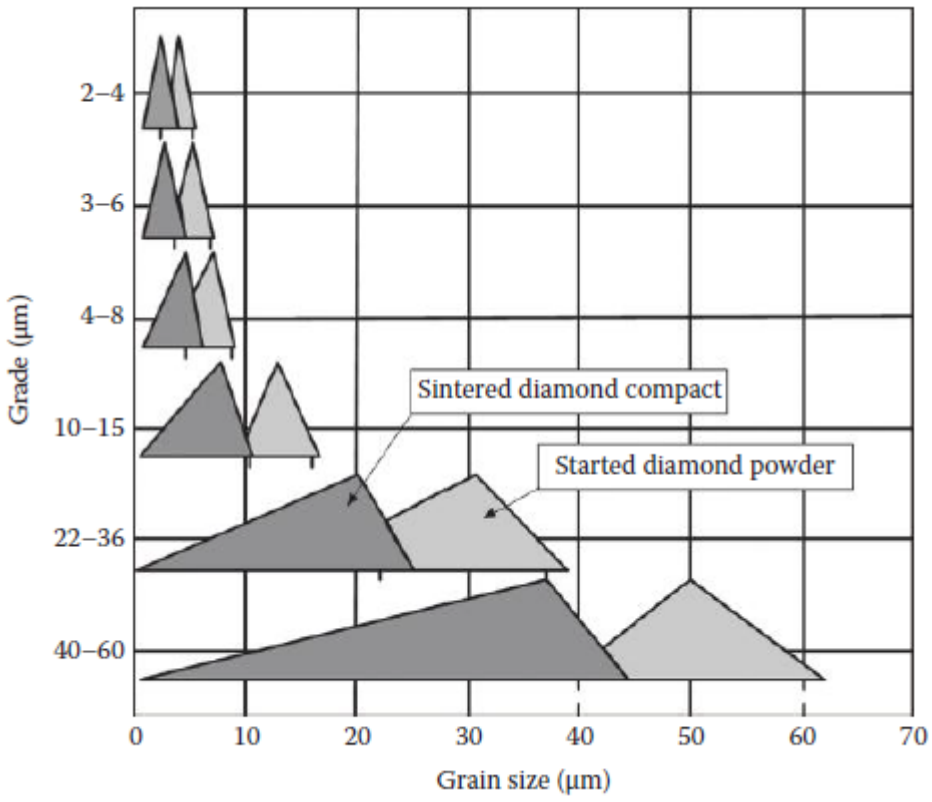


Figure 7: Schematic diagram showing the relationship between the grain size of diamond before and after sintering [10].

2.5.2. PDC Sintering

PDC sintering occurs in the following manner: (i) Cold compaction in which rearrangement and crushing of particles take place, (ii) hot compaction which further crushes and rearranges particles and introduces plastic deformation and densification and (iii) cobalt infiltration which promotes penetration of grain boundaries (and sweeping of diamond surfaces) as well as dissolution and re-precipitation. Figure 8 shows the PDC sintering stages described.

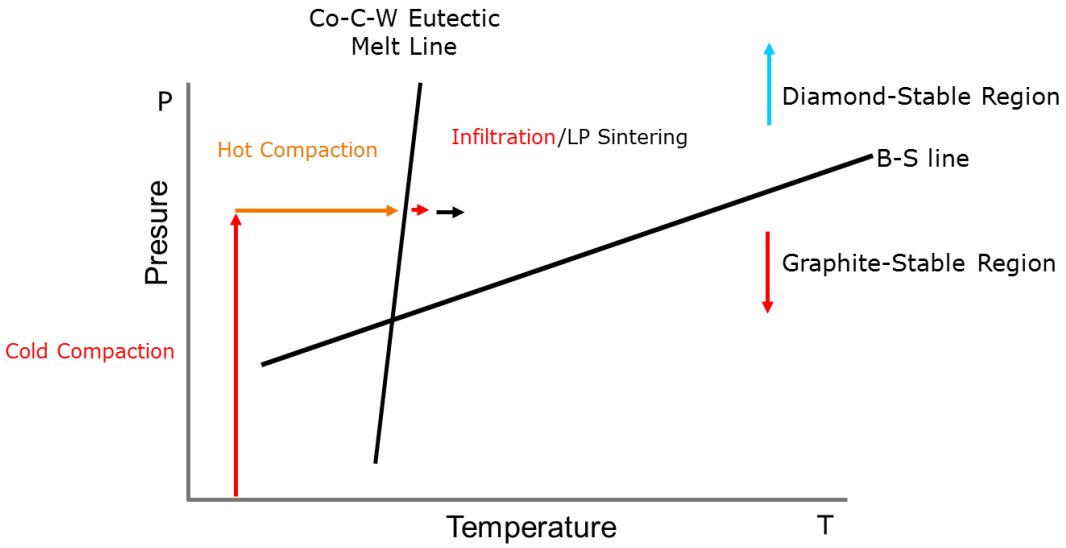


Figure 8: PDC sintering schematic trajectory [29].

When packed particles are exposed to temperatures that are nearing the melting temperature of the LPS aid, they tend to bond together. When the diffusion process speeds up at higher temperatures, the bonding between contacting particles is a result of sintering. Sintering is faster when cobalt particles approach their melting temperature of 1438 °C, but initially it occurs over a range of temperatures [30]. It occurs more rapidly as the size of the particle decreases, due to the fact that diffusion distances are shorter and the free energy of the fine particles is much higher, due to curvature stresses and free surface energy [31].

The process described above relates to liquid phase sintering. In the case of PCD, sintering takes place by means of a solution and precipitation process called Liquid Phase Sintering (LPS). In such a process, a liquid phase sintering aid is used which typically melts at temperatures significantly lower than that of the particles being sintered together.

In such a process parts of the particles dissolve in the liquid phase and are re-precipitated at other places in the preform, possessing lower free energies than the points of initial solution. Through this process the particles bond to each other, since the points of precipitation are typically at the interface between adjacent particles. In the case of PDC, the liquid phase is provided by a cobalt base tungsten alloy, originating from the WC-Co substrate.

Diamond grains next to the interface dissolve and diffuse into the WC-Co substrate to equalise the chemical potential gradient for C; as the temperature is increased Co can dissolve more C, this creates a chemical potential gradient from the diamond side to the WC-Co side. Local loss of diamond next to the interface creates a zone for Co to fill in to dissolve more and more diamond.

This (dissolution of diamond grains at the interface) also results in the so called river marks at the interface, (Figure 9). These river marks resulted from erosion which is the selective dissolution of the diamond particles to achieve equilibrium solubility in the Co throughout the period of the liquid. Co pooling and selective dissolution of diamond grains also take place at the top surface of the diamond layer. Figure 9 shows selective dissolution of diamond grains in infiltrating cobalt causing river marks in the regions next to the interface during PDC sintering.

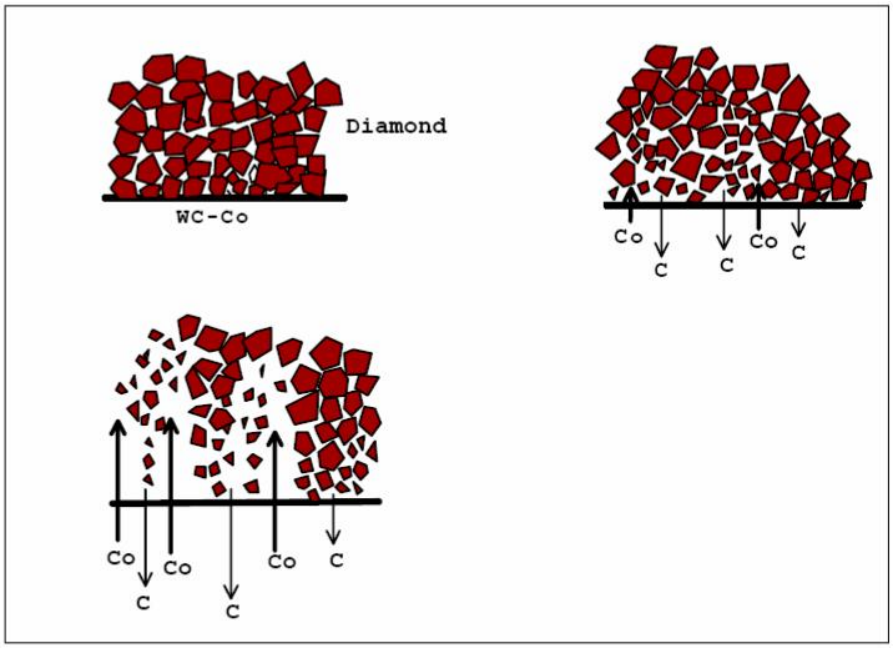


Figure 9: Selective dissolution of diamond grains in infiltrating Co causing. "river marks" in the regions next to interface [29].

The sintering of PDC does not depend on solid state carbon atom diffusion, but on the solution and re-precipitation processes of the carbon atoms into the cobalt base liquid phase sintering aid. It is for this reason that sintering can occur at temperatures equal to the melting point of the Liquid Phase Sintering (LPS) aid, rather than the much higher melting point of diamond. Sintering is the most critical step in the manufacture of a Polycrystalline Diamond Compact (PDC) and the whole sintering process shown in Figure 8 is discussed in section 2.5.2.

Figure 10 shows what occurs during sintering of the PDC materials which further shows what has been shown in Figure 9.

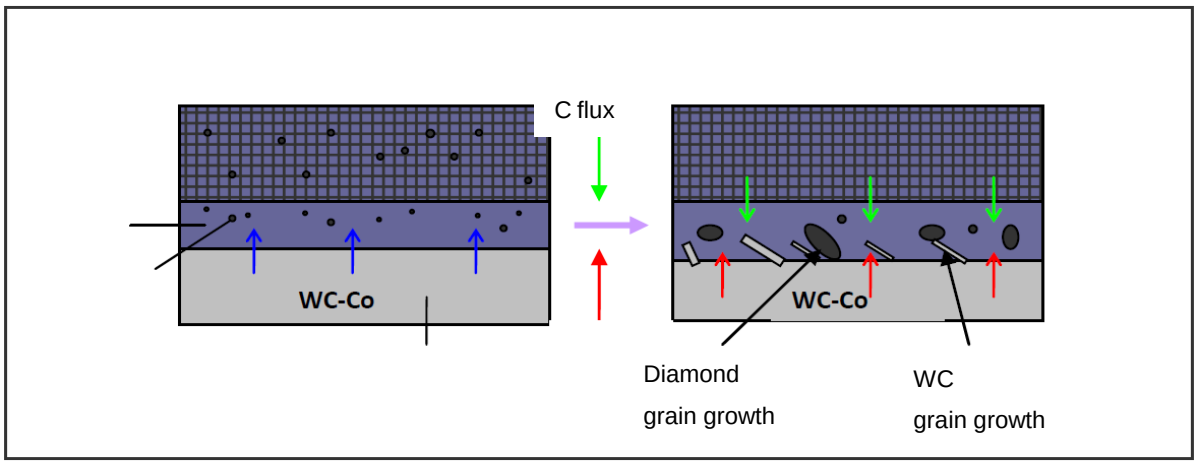


Figure 10: Diagram of the sintering of PDC materials [30].

Figure 11 shows the microstructure of what occurred during sintering of the PDC material. Syndrill is a PCD compact that has been developed for the cutting element in high performance drill bits for oil and gas exploration. It consists of a Polycrystalline Diamond (PCD) top layer which sintered to a WC substrate.

The diamond layer improves the drilling performance through controlled wear and retaining of a sharp cutting edge while the WC substrate delivers a strong and tough support for the diamond layer and enabling attachment of it to the drill bit body by brazing. Light patches of cobalt are likewise noticeable between the diamond grains clearly visible on a micrograph from SEM analysis. Cobalt forms a vital part in this process as a catalyst material in the synthesis of this type of PDC; without it, no new intergrowth would happen between the grains. In addition it is noted in Figure 11 that the boundary between the diamond layer part and its WC support shows intimate bonding in this region.

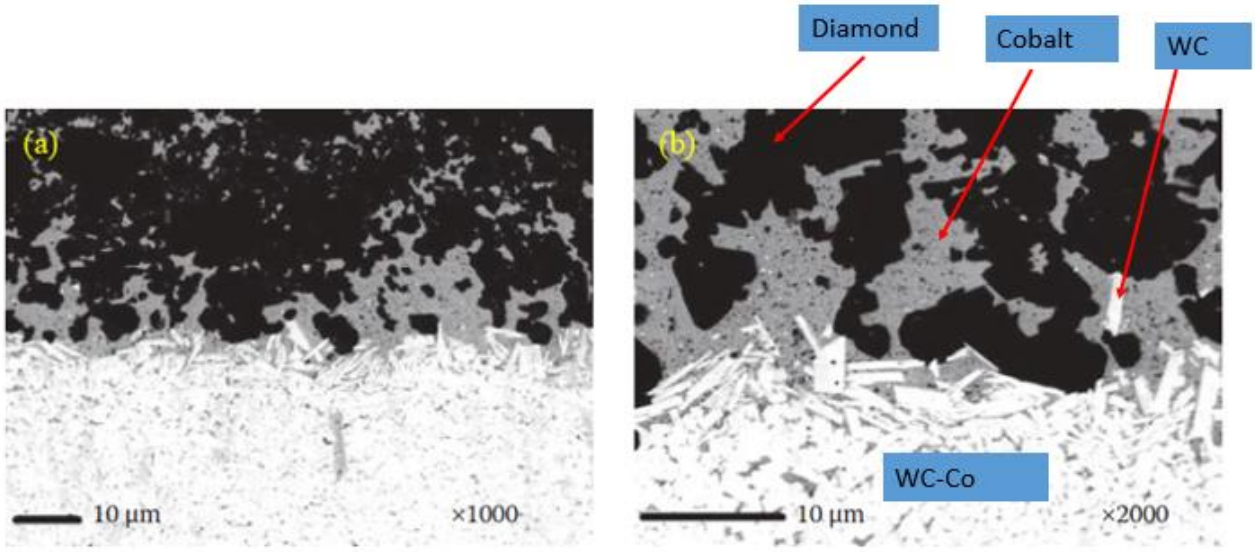


Figure 11: SEM micrographs of a polished section showing interface and bulk of PCD [10].

Cold compaction

Cold compaction occurs when pressure is applied to the PCD material during the sintering process and when the diamond powder preform is still at ambient temperature. Three processes occur during this stage; particle movement, crushing of diamond and filling of voids by fine (10 - 15µm) diamond particles. At a given pressure, coarser (>16 µm) particles are easily crushed than finer particles due to the large void spaces that exist between them. The average particle size changes radically and the Particle Size Distribution (PSD) turns out to be bimodal. The coarser powders' porosity is higher than that observed on finer powders.

The pore size of the coarser powder is longer at a given pressure. As pressure is increased the variances between coarse and fine grains gets smaller. During this stage, the diamond particles crushing significantly moves/changes the particle size distribution to smaller sizes. The end product of cold compaction is a high density diamond powder compact with decreased porosity. Coarse diamond feed responds exceptionally well to cold compaction.

During cold compaction as shown in Figure 12, diamond particles crack and crush when pressures, amplified at the contact points of one diamond particle with another, exceed

the strength of that particle. Shape of the particles, in this sense, plays a role; if they have sharp corners, or are irregular in shape they are more likely to crush than particles having rounder/regular shapes [11].

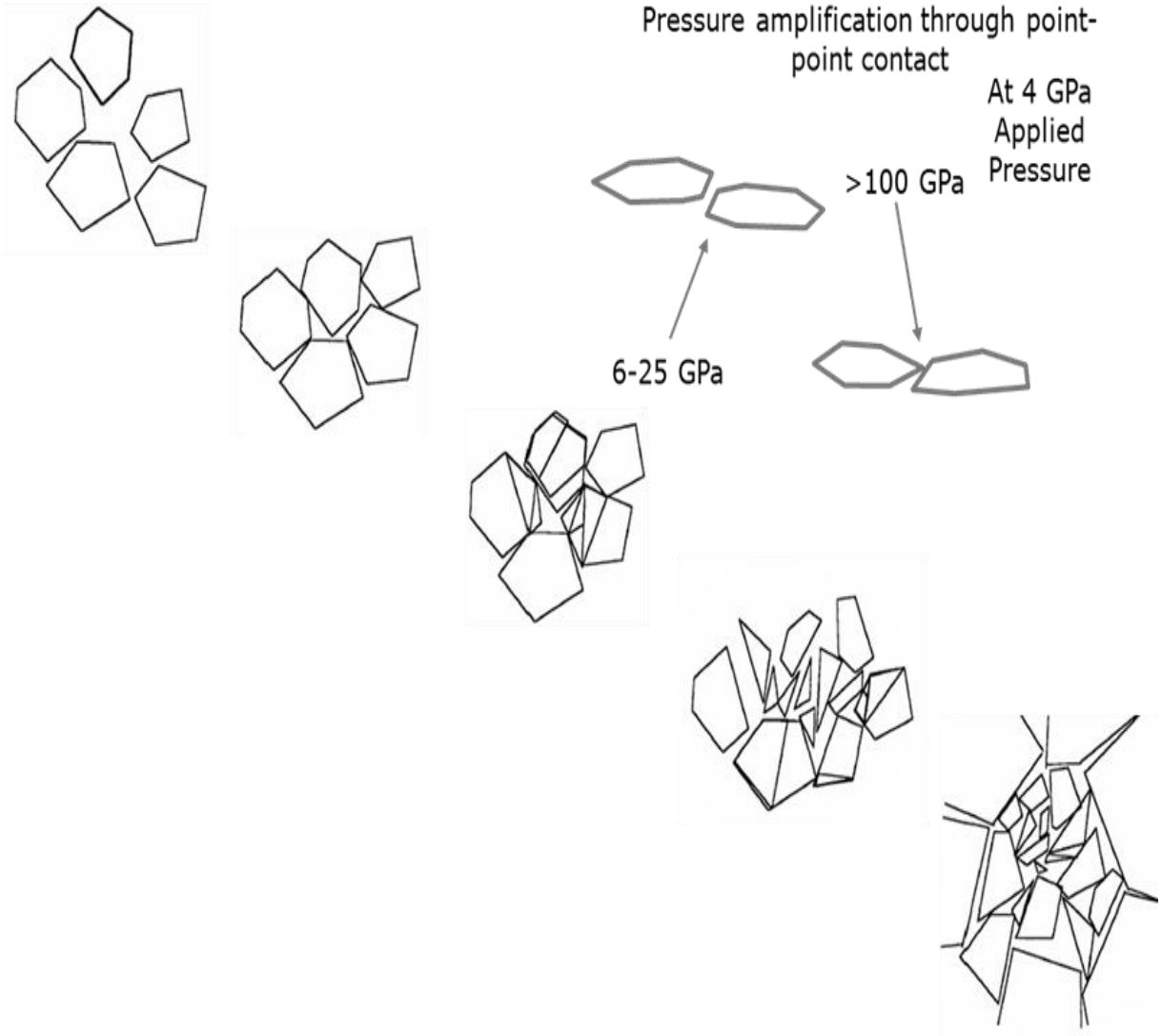


Figure 12: Representation of process taking place during cold compaction [11].

Figure 13 shows the effect of pressure on crushing of diamond grains. Coarser powder crushes more due to the high surface energy. The presence of larger pores in coarser grades is the reason why course diamond grades are easier to infiltrate with cobalt during sintering.

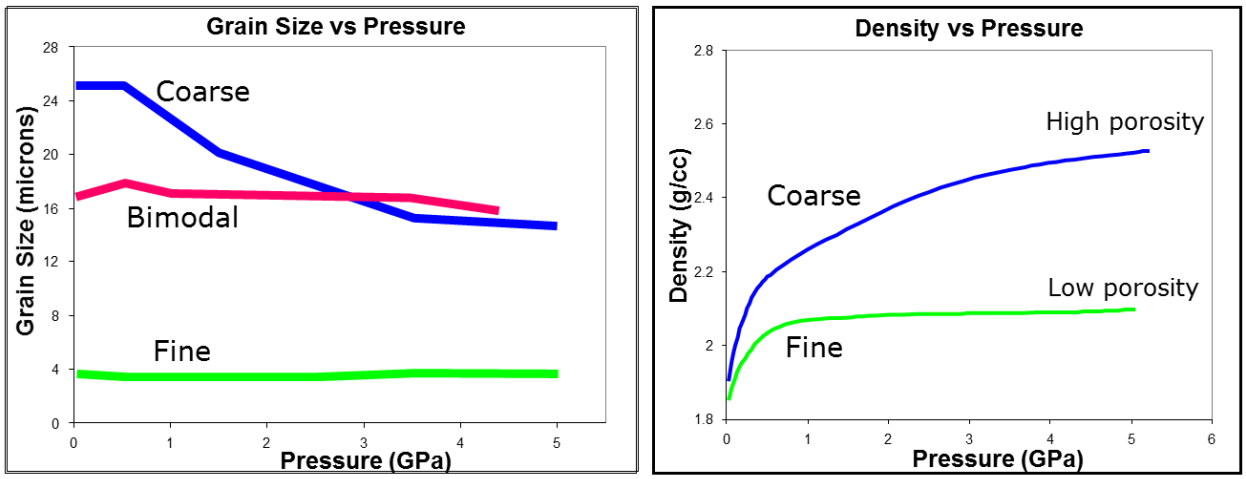


Figure 13: Graph representation of densification taking place during cold compaction [29].

Hot Compaction

The cold compaction stage is followed by hot compaction. At this stage, temperature is raised to just below the melting point of the metallic Co-base phase present in the WC-Co substrate. Figure 14 shows different stages of sintering.

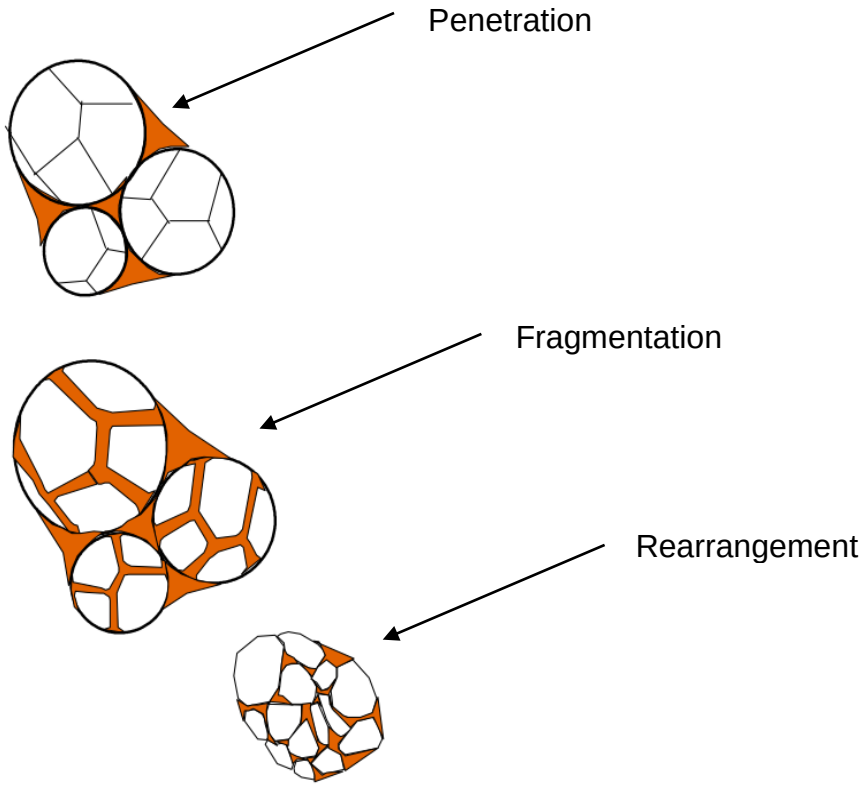


Figure 14: Illustration of rearrangement and fragmentation of polycrystalline particles leading to secondary rearrangement [29].

Hot compaction further builds diamond phase density past what can be accomplished by cold compaction as shown in Figure 15. During the hot compaction stage no infiltration and liquid phase sintering occurs since the temperatures are not sufficiently high for the Co phase to melt. Just plastic deformation of diamond grains, graphitization of diamond surfaces, densification of the compact and some solid state sintering processes take place as indicated in Figure 15.

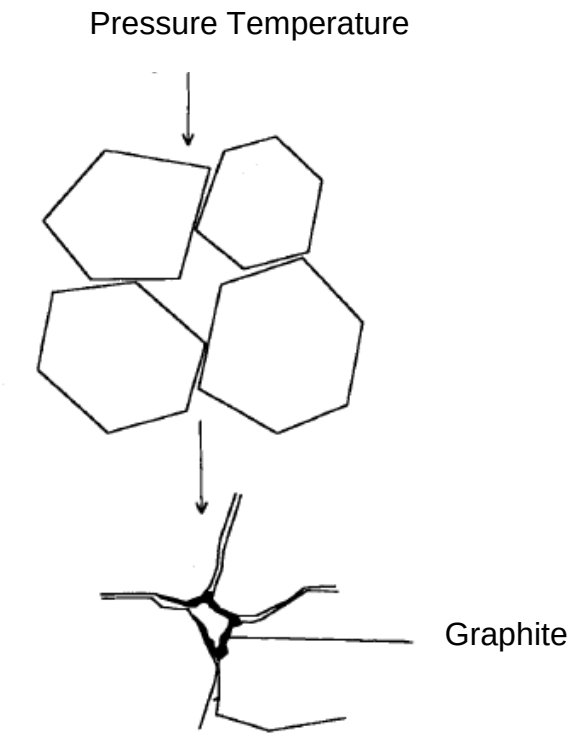


Figure 15: Schematic representation of diamond grains deformation under HPHT [29].

The diamond compact densification continues with more crushing and rearrangement up to 700 °C of the crushed particles when the temperature is increased at high pressures [11]. The process of densification continues with plastic deformation after 700 °C [11]. At high temperatures, the surfaces of the diamond grains begin to become smoother due to surface tension and, as the sharp edges disappear, they begin to deform in the zones of contact [11].

During hot compaction, the smaller particles have a larger sintering reactivity hence their densification rate is faster compared to coarser particles. It is still far from making up for the density advantage that coarser grains get at the end of cold compaction stage. For example in Figure 16, G04 densifies by 17% during hot compaction whereas G75

densifies by 7%. G04 represent 4 µm grain size and G75 is 75 µm respectively. Figure 17 shows a porosity change that occurs as the temperature is increased. This change yields the porosity free structure after sintering is completed. The mathematical equation showing the relationship between temperature, time and final porosity (*P*) at a given pressure is:

$$P = (a_0 + a_1 t).e^{-(b_0+b_1)/T} \qquad \text{Equation 1}$$

where t is time, T is absolute temperature and a_o, a_1, b_0, b_1 are constants for a specific grit size and pressure level.

Figure 16 shows the extent at which pore size changes as the temperature is further increased to 1350 °C.

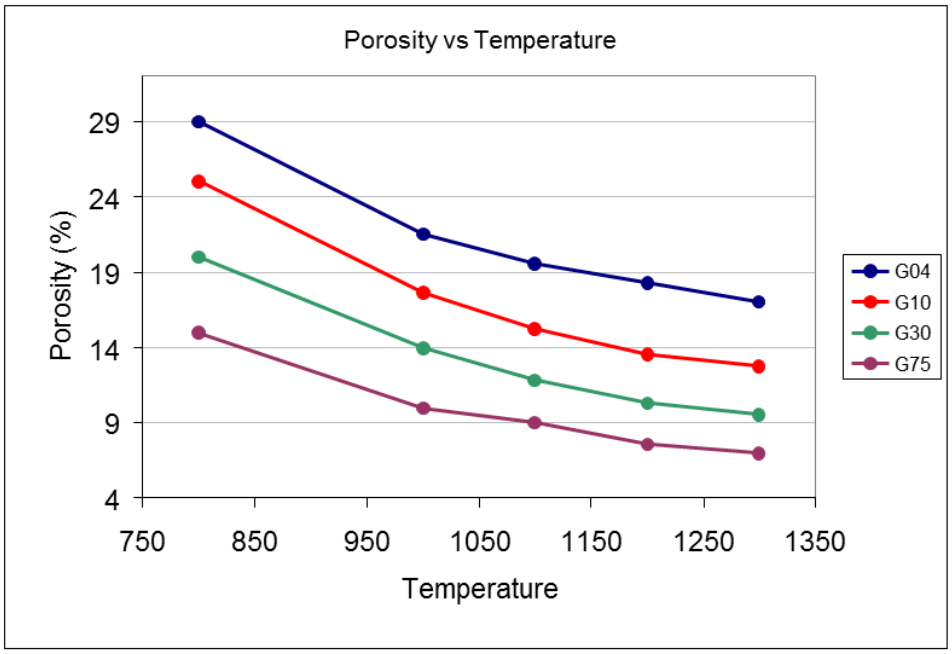


Figure 16: Porosity versus temperature during hot compaction at 5.5 GPa [29].

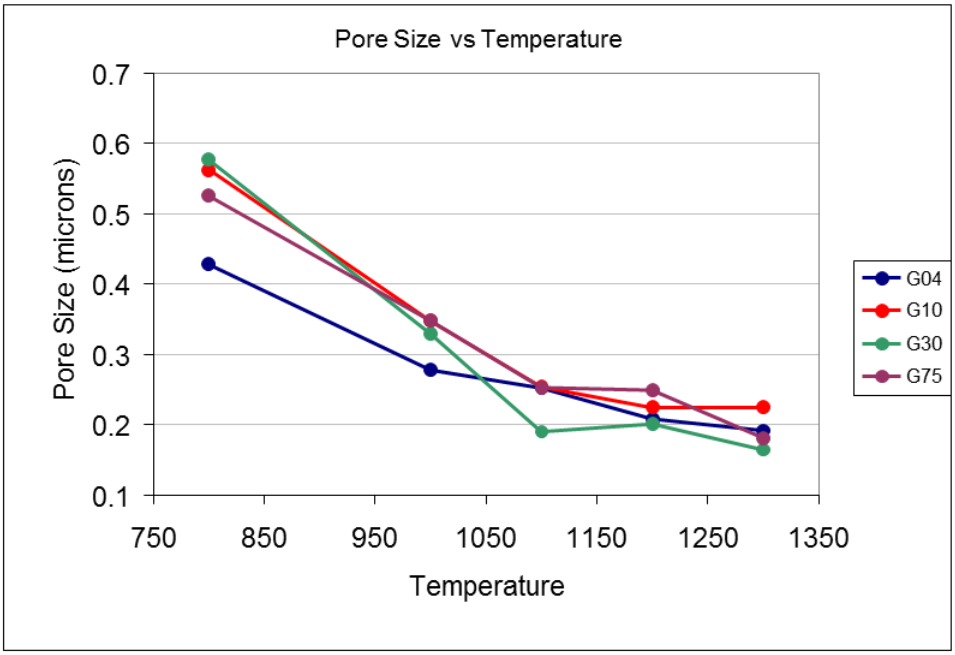


Figure 17: Pore size change during hot compaction as temperature is increased which maintain pressure at 5.5 GPa [29].

Graphitization during Hot Compaction

During the graphitization process, carbon atoms, one at a time, are removed from the diamond surface. The amount of graphitization is dependent on the increase in temperature at a given pressure [11]. The specific resistivity of the compacts can be associated with the level of graphitization since graphite is a conductive material compared with diamond which is an insulator. If temperatures are further increased, the bulk graphitization of diamond grains begins to take place and the produced PCD compact's hardness and wear properties start to degrade.

From these observations one can infer that, at a given plastic deformation, the change in hardness and wear resistance is determined by the level of graphitization. Nonetheless, the properties are more sensitive to plastic deformation until bulk deformation starts taking place and thereafter both plastic deformation and graphitization take place. Because of the large surface area in contact with pores, finer particles tend to graphitize more than coarser particles at a given pressure and temperature as shown in Figure 18 and a consequently higher number of nucleation sites are available.

As the sintering temperature further increases, densification of the diamond compact improves and the voids disappear. This process is clearly depicted by a set of micrograph images shown in Figure 19 [20].

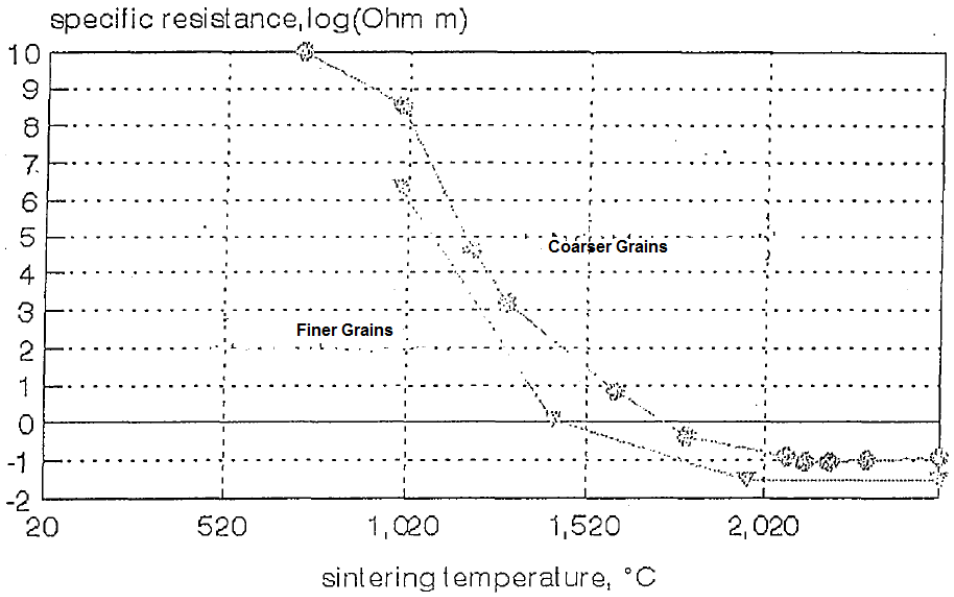


Figure 18: Change in specific resistance of diamond compacts with sintering temperature [29].

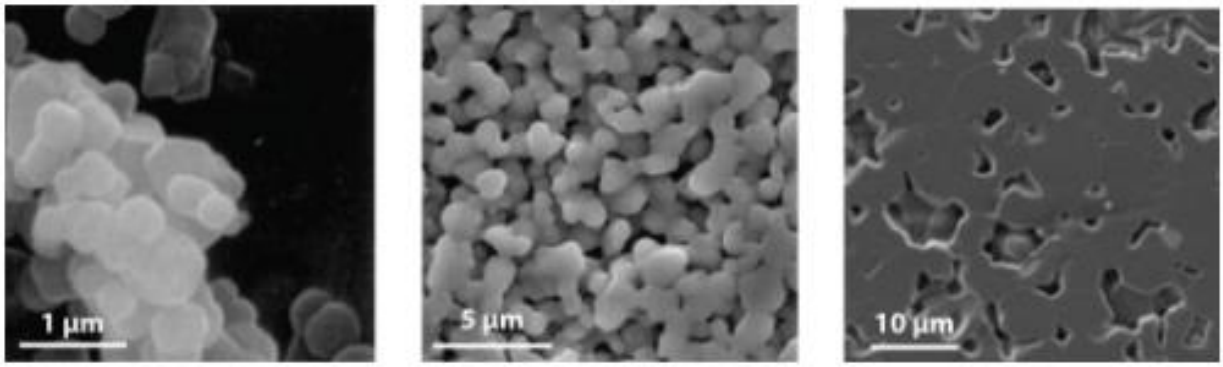


Figure 19: Micrograph of ceramic material sintering stages process when temperature increases. Left: Initial stage sintering, middle: Microstructure after sintering for two hours at 1250 °C (Less porosity than initial stage), and right: the microstructure after sintering for two hours at 1450 °C [32].

2.6. Liquid Phase Sintering and Metal Phase Infiltration in PCD Compacts

2.6.1. Liquid Phase Sintering overview

Liquid Phase Sintering (LPS) is a process whereby high performance, multiple-phase components are formed from powders which are utilized as part of industrial and commercial products. One of the most common utilization of LPS is found in the sintering of building bricks from earth based minerals (hydrated aluminium silicates).

Scientific developments in understanding LPS started in the 1950s and included sintering under conditions where solid particles existed together with a wetting liquid. Numerous variations of LPS were employed to an extensive variety of engineering materials. This process has found its applications in car motor connecting rods and high-speed metal cutting inserts [33]. The LPS methodology allows the development of dense, pore free PCD inserts with properties better than any earlier known cutting material. The advantages of the LPS process include speedier sintering, caused by rapid atomic diffusion through the liquid phase, as well as reduction of sintering temperature from that approaching the solid phase melting point to the melting point of the liquid phase sintering aid. For these reasons LPS is much faster and more convenient than solid state sintering.

Another critical advantage of this process is that rapid compact densification is accomplished by capillary attraction because of a wetting liquid, resulting in rapid particle rearrangement at the onset of the generation of the liquid phase. This resulting “particle rearrangement” densification step occurs with no external pressure applied. LPS has a few limitations in its application. Such inadequacies include compact slumping, which happens when a lot of liquid is formed during sintering. The same parameters that control the sintered microstructure regularly control the final product [34]. Furthermore, the strength of the resulting material often decreases at the melting point of the phases resulting from the solidification of the LPS aid at the end of the LPS process.

Understanding the relationship between the system’s properties, the developing density and the microstructure is vital [35]. During LPS, the microstructure comprises solid grains in a liquid phase (Cobalt), where the liquid gives both a capillary force and a transport medium that advances full densification [13].

Liquid phase sintering is divided into three stages [36].

- Dissolution and primary rearrangement,
- Solution-precipitation, resulting in further decrease of the distance between centres of gravity of individual particles, together with neck thickening and
- Final pore removal and noncommittal coarsening.

Critical Parameters and Processes in Liquid Phase Sintering

The critical parameters for the cold compaction stage are pressure, starting average grain size, starting grain size distribution, amount of cobalt admixed in the powder, a figure of merit for the strength of a specific diamond batch, and output parameters are volume percent porosity and average pore size.

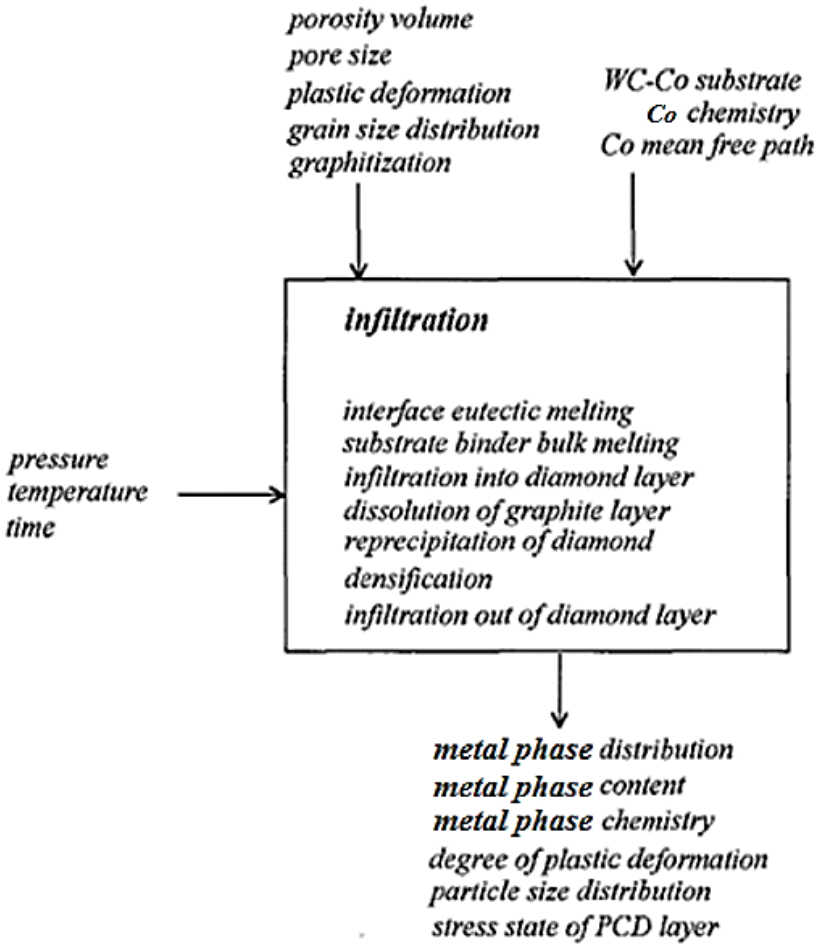


Figure 20: Critical Parameters and Processes in Liquid Phase Sintering [29].

2.6.2. Primary re-arrangement

The primary stage is the rearrangement stage resulting from particle repacking simultaneously with liquid formation giving substantial densification; this takes place in a short time. Speedy initial densification is observed in the primary re-arrangement stage resulting from the movement of particles in the direction of the formed wetting liquid phase by capillarity force [37]. Re-arrangement is further improved by the solubility of the diamond particles in the liquid metal phase giving closer packing, and also resulting in increase in densification [37].

The elimination of pores occurs concurrently and minimizes the total interface energy of the system. Microstructural changes occur during the early stage of sintering and most of the densification is achieved during primary re-arrangement, because it is during this part of the process when the liquid phase fills up most of the voids [37].

2.6.3. Solution re-precipitation (Secondary re-arrangement)

Secondary rearrangement is mainly due to the solution re-precipitation (Ostwald maturing) [38]. In this step, densification occurs at the same time with grain development and shape accommodation of diamond particles. After re-arrangement takes place, the newly formed liquid phase spreads between the diamond particles, forming liquid films between them. This raises the chemical potential for dissolution of the solid phase in contact with the liquid, which then dissolves, while diamond is kept out of the liquid [39].

The smaller diamond grains dissolve because of their higher dissolution potential, (expanded chemical potential) [40] and the bigger grains grow by material re-precipitation (Ostwald aging). The substantial large grains experience shape accommodation due to precipitated material from the dissolved smaller grains, prompting accessibility for the liquid phase to fill the pores. The amount and the size of pores decreases with increase in grain size. Grain growth due to Ostwald ripening can be described by Equation 2:

$$G^n - {G_o}^n = k(t - t_o) \qquad \text{Equation 2}$$

where G_o is the grain size before sintering at time (t_o) and G is the grain size at end of the sintering at time (t), k is a material constant dependent on temperature [41], $n=2$ for

interface reaction-controlled Ostwald ripening and *n=3* for diffusion-controlled Ostwald ripening [41]:

$$k = k_o \exp(-\frac{Q}{RT}) \qquad \text{Equation 3}$$

Where *Q* is the activation energy for grain growth, R is the universal gas constant and T is absolute temperature. Thus, grain growth due to Ostwald ripening is dependent on the activation energy for grain growth, time and temperature [42].

2.6.4. Final pore removal, and coarsening

During LPS, densification occurs at the same time as grain coarsening, however in the final stage, grain development is dominant [38]. Grain development in the last stage is a result of interface response controlled by Ostwald ripening [41]. After secondary rearrangement, the diamond phase and cobalt phase are completely, or totally dense, consequently this last sintering stage influences the microstructure in terms of grain size, distribution and shape, as well as metal phase distribution and spreading. The adjustments in the microstructure influence mechanical properties, for example, hardness, wear resistance and fracture toughness [11]. In industrial practice, PCD compacts are densified by sintering at high pressure and at temperatures that range from 1350–1650 °C leading to virtually pore-free compacts.

Polycrystalline diamond consists of intergrown grains resulting from micron-sized engineered diamond powders with the said intergrowth being the result of the LPS process. The later takes place at pressures of 5.5 GPa and temperatures in the range 1450-1550 ºC. PCD is regularly sintered onto a cemented tungsten carbide substrate containing a cobalt binder phase. This substrate gives backing to the diamond layer and a means for attaching it to a given tool. At high pressure and high temperature conditions, cobalt metal melts in the carbide substrate and enters the diamond powder filling in the pores between diamond particles, and encouraging diamond-to-diamond bonding by enhancing the LPS kinetics between grains.

Depending on the volume fraction of diamond and metallic phase in the material, the resulting composite shows a range of superior properties attractive for cutting and drilling

tools [36]. The microstructure that gives rise to these properties is related to the sintering conditions [43].

This process of LP sintering creates a coherent diamond structure with residual cobalt metal left in the pore spaces between diamond grains. The more fine grain diamond particles react to LPS and have a tendency to have higher sintered density over coarser diamond particles, demonstrating a higher volume fraction of metallic cobalt content [44].

The use of ferromagnetic metal phase material for the sintering of diamond compacts has three advantages: (i) a reduction in sintering temperatures and pressures, (ii) cleaning the diamond surface of graphite, and (iii) electron discharge cutability for tool making [11]. PCD materials are exceptionally favorable in view of their high hardness, high thermal conductivity, and wear resistance.

2.6.5. Liquid phase sintering typical microstructure

Liquid phase sintering results in a range of sintered microstructure for a variety of materials. It is observed that the shape and distribution of the phases have clear differences. The microstructural investigation permits the analysis to quantify each phase, for example, solid grain size, porosity, grain shape, and solid-solid contact size. The essential thermodynamic behavior of the materials is additionally studied from the microstructure measurements which thus take into consideration the monitoring of the kinetics. LPS microstructure is described in terms of grain size, grain shape and grain orientation in relation of a measure of a phase and connections between the phases.

2.6.6. Contact angle in liquid phase sintering of PCD

The balance between the interfacial energies is represented by a physical characteristic which is called the contact angle. The aggregate free energy must be reduced in order for a liquid to wet a solid. At the point in which the formation of liquid occurs during sintering, three phases are observed and are present in a microstructure– (i) solid, (ii) liquid, and (iii) vapour.

Good wetting is shown in Figure 21 a) whereas poor wetting is shown in 21 b). The wetting level is described in terms of the contact angle demonstrated in each of the figures. The contact angle θ is the angle included in the liquid; its size relies upon the balance of the

surface energies. As indicated in Figure 21 c), the contact point is connected with the vector equilibrium of the three interfacial energies [42]. The level of wetting is portrayed by the contact edge shown in Figure 21.

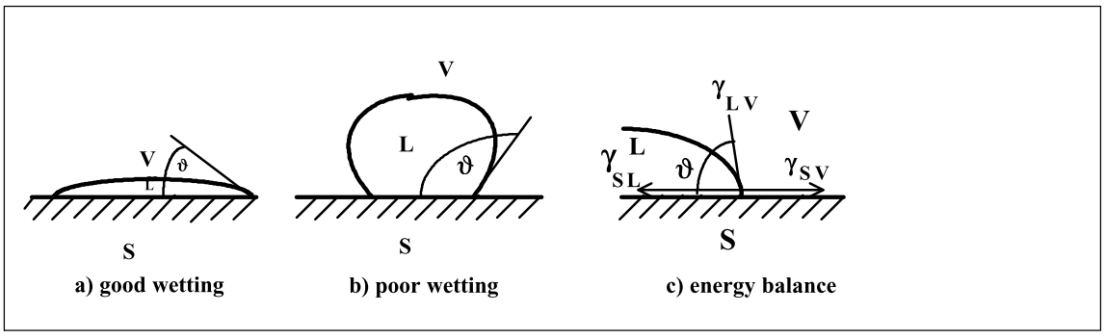


Figure 21: Contact angle in a solid/liquid/vapour system space [42].

Where, γ is the interfacial surface energy and SL denotes solid-liquid, LV denotes liquid-vapor and SV denotes solid-vapor in Figure 21.

Since there is a connection between the vector equilibrium of the interfacial energies and the contact edge, in this way, for the purpose of solid-liquid-vapor contact to be in equilibrium, the sum of the horizontal components of the three vectors must equal zero.

2.6.7. Dihedral Angle in Liquid phase sintering

The dihedral angle Φ forms when a solid - solid grain boundary is formed in equilibrium with a liquid. The dihedral angle and surface energy equilibrium between two intersecting grains with a partially penetrating liquid phase is shown in Figure 22. The dihedral angle is a characteristic of the ratio of energy between the solid - liquid surfaces and grain boundaries and it influences the degree of penetration and the liquid phase shape at the grain intersections.

In LPS, the dihedral angle is a function of time. When the melt forms and spreads, the penetration of grain boundary leads to a change in chemical composition in the liquid. The liquid chemical composition and interfacial energy show changes during solid dissolution up to the solubility limit. Gradually, the solid-liquid surface energy will stabilize at a value lower than the initial (unalloyed) melt value [31].

After the infiltration of Co at the diamond to diamond grain boundaries and reaction between cobalt and diamond is complete, the system approaches an equilibrium dihedral angle. Due to the rapid initial decrease in dihedral angle, there exists a possible over-penetration of the liquid into grain boundaries.

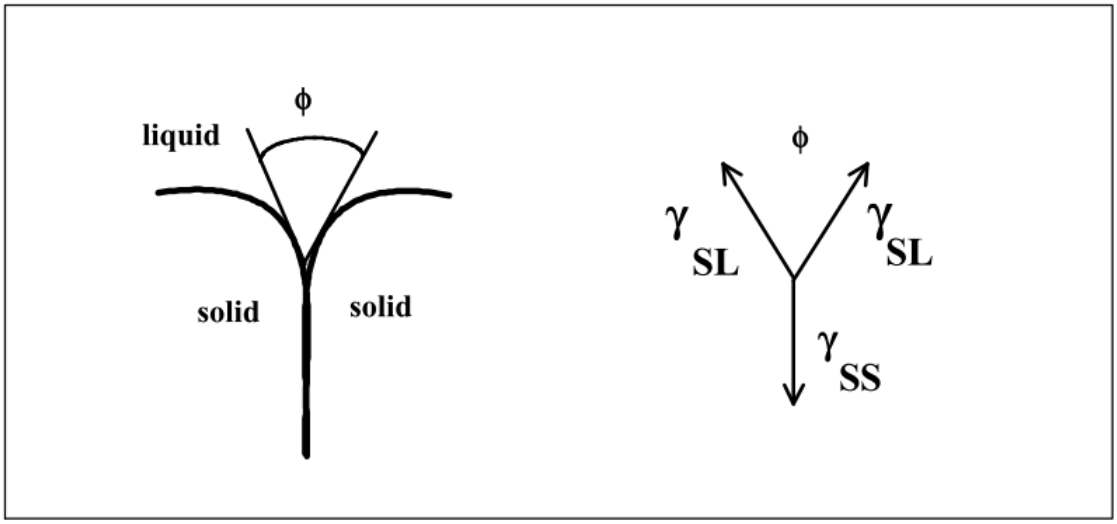


Figure 22: Figure of dihedral angle in a solid/liquid system [42].

2.6.8. Volume Fraction in LPS

The Volume fraction of liquid in a solid-liquid composite is specifically impacted by the measure of added phase. This quantity has a noteworthy impact on the rate of sintering and the sintered microstructure. Features like grain size, grain separation, contiguity, grain shape accommodation, and liquid connectivity are subject to the volume fraction of a liquid [42]. The volume fraction is dependent on three phases which initially occupy a portion of the total volume. These are the volume fraction of solids V_S, liquids V_L, and pore phases V_P, respectively. The three volume fractions add up to unity,

$$1 = V_S + V_L + V_P \qquad \text{Equation 4}$$

2.6.9. Grain Shape

The grain shape is subject to the volume fraction of solid, surface anisotropy and dihedral angle (Φ). The grains change shape to accomplish better packing because contacts form between adjacent grains at the higher volume fractions of solids [42]. The growth of the coarser grains is a result of finer grains crushing and, the small grains dissolving are spherical, whereas the growing large grains have flat face. As the full densification is

reached during LPS, the flat faces for the contact zones are formed by solid grains, yet retaining a rounded overall shape.

Figure 23 shows liquid phase that stretches along the edges of the rounded polyhedron [42]. This is due to the fact that the rate at which the size change is often too quick during dissolution for the grain to maintain an equilibrium shape. In the case of diamond, if the crystal surface is very high, then faceting results, and if the surface energy is low, then a spherical grains form.

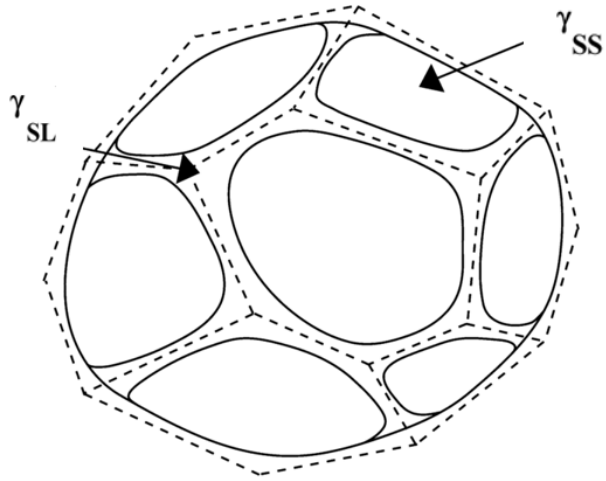


Figure 23: Grain shape change as fully density is reached during LPS [31].

2.6.10. Contiguity in LPS

Contiguity measures the extent of solid-solid contact in a liquid phase sintered material; this is in the later stages of LPS independent of the grain size. Contiguity is expressed as the surface area of solid – solid contacts as follows:

$$C_{ss} = \frac{S_{ss}}{(S_{ss} + S_{SL})} \qquad \text{Equation 5}$$

Where S_{SS} is the surface area per grain of the solid-solid contact and the solid-metal phase surface area per grain is S_{SL}. Contiguity increases by increasing the volume fraction of solids and the dihedral angle [45].

The contiguity can also be measured using the number of intercepts per unit length metallographically as follows:

$$C_{ss} = \frac{2N_{ss}}{(2N_{ss} + N_{SL})}$$ Equation 6

Where the subscript SS denotes the solid-solid intercepts and SL denotes the solid-Co phase intercepts. The factor 2 in the equation above is necessary since the solid-solid grain boundaries are only counted once by this technique, but are shared by two grains [42].

In measuring contiguity in PCD, there is an issue of not having the capacity to determine diamond to diamond grain limits by conventional techniques like an optical microscope and SEM. That is the reason for using indirect methods to measure contiguity in PCD.

2.6.11. Metal phase Infiltration (spreading and rearrangement)

The infiltration is a two-step variant of LPS [31]. The microstructural evolution of PCD was studied by Froschauer and Fulrath. These authors confirmed that rearrangement is the primary densification process. The metal phase spreading rate is restricted by a number of factors. These factors include surface area, curvature and chemistry of the diamond particles and content, dispersion, chemistry and physical properties of the liquid metallic phase (LMP). Metal phase spreading is associated with the Young-Laplace forces acting along the wetting front line between diamond and LMP. These infinitesimal forces rearrange and reduce the mean distance between neighbored diamond particles, bringing about densification [46].

There are four primary stages in the infiltration of the cobalt phase [47] during liquid phase sintering of PCD compacts:

(1) During the initial stage, the temperature is sufficiently high to bring about melting of the Co-W-C at the interface because of the high carbon concentration which causes a decrease in the eutectic temperature [11].The dissolved metal phase penetrates into the diamond because of the high pressure gradients between the permeable diamond body and the solid interface.

(2) In the second stage, the cobalt metal phase in the bulk substrate begins to melt. As the temperature increases and the metal phase in the bulk substrate melts, infiltration occurs and cobalt enters into the diamond compact because of pressure gradients

which are equivalent to the capsule interior pressure. During this infiltration period, liquid cobalt dissolves tungsten carbide forming a solid solution. As the solubility of carbides in cobalt increases, the alloy phase is totally liquid.

(3) In the third stage, mass transfer of the cobalt metal decreases as the pressure gradients decreases. Once the pores are totally filled, either by the infiltrating metal, or (to be avoided) by residual gas, the pressure gradient becomes zero.

(4) In the fourth stage, an adjustment toward the flow of the liquid phase occurs. The amount of liquid phase in the diamond layer decreases and increases in the substrate. The reason is that the densification of the diamond skeleton drives the Co out, thus pushing it back into the substrate.

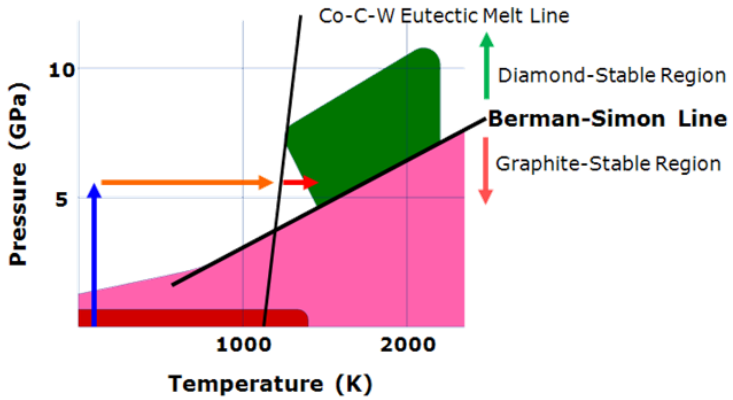


Figure 24: Phase diagram showing cobalt melt line and LPS of PCD sintered Structures [18].

The process of liquid phase sintering using carbide substrate (WC-Co) materials occurs by the liquid infiltrating metal turning into a cobalt alloy with dissolved tungsten and carbon [30]. This concentration is much lower than that of fine carbon. This difference in C activity results in dissolving large amounts of the first layer of diamond in contact with the interface. Once the infiltrate is soaked with carbon it can then work as a liquid phase sintering aid. The tungsten in the liquid cobalt reacts with a portion of the additional carbon and precipitates as tungsten carbide (WC) crystals at the interface of the substrate and PCD layer. This results in a large depletion of diamond at the substrate interface and a thick Co layer forms in this depleted diamond zone referred to as the cobalt pool.

Figure 26 is the schematic representation of LP sintering process whereby sintering starts off from powder mixing and filling of pores as the temperature increases, then rearrangement takes place, followed by solution re-precipitation and finally densification.

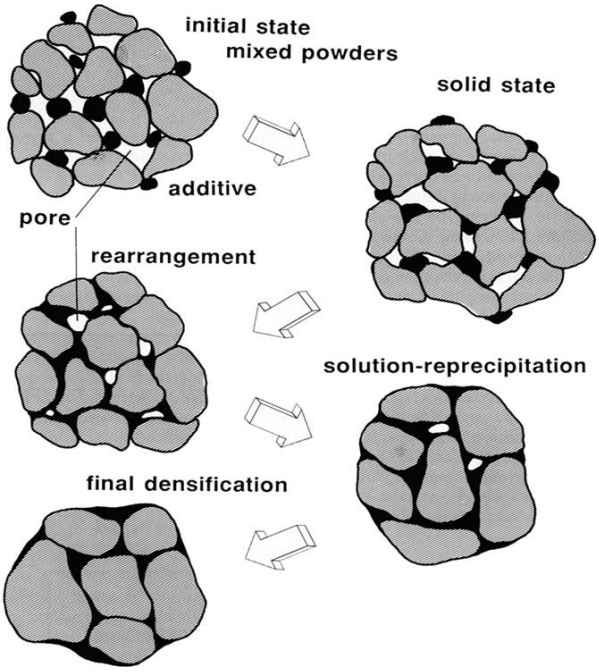


Figure 25: Microstructure changes during conventional sintering, starting from mixed powders to fully dense sintered compact [31].

2.6.12. Cobalt mean free path

The metal phase mean free path is dependent on both the cobalt content and the diamond particle size and can be utilized to describe the distance travelled by a dislocation when the metal phase is free of precipitates. Transverse rupture strength (TRS) is a property that determines mechanical strength of a brittle material and, in the case of PCD, is dependent on the grain size and cobalt mean free path.

Change in the magnitude of the mean free path leads to a transition from brittle to predominantly ductile failure. At the point when the metal phase mean free path is low the strength of an intergrown PCD material is controlled by the fracture toughness of the composite and increases with increasing metal phase mean free path. At the point when the metal phase mean free path reaches higher values the PCD material yields before failure and the strength is for the most part controlled by the resultant strength of the metal phase, which decreases with increasing cobalt mean free path. The strength of an intergrown PCD material is primarily due to the diamond-diamond bonding.

2.6.13. Effect of the cobalt content in PCD

PCD compacts used as part of specialized applications regularly contain between 5 to 20 wt% cobalt [19]. The hardness of the material decreases with increasing cobalt content while the compressive strength reaches a maximum at 2 wt% Co and after that decreases with increasing Co content. The cobalt content in the diamond part originates from the metal's migration from the substrate during sintering. Normally, cobalt content can be between 6 to 18 wt. % in tungsten carbide substrate and 5 to 20 wt. % in the diamond part.

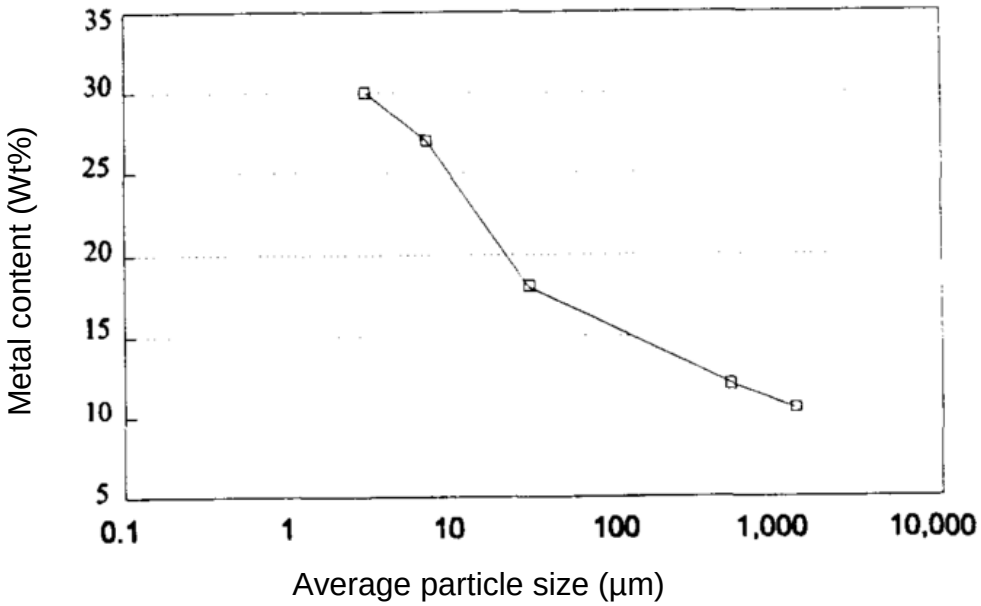


Figure 26: Cobalt content in PCD layers as a function of grain size [35].

Applying the density measurement procedure and using pure diamond crystal density of 3.53 $g.cm^{-3}$, it was possible to calculate the metal content of various grain size PCD layers as shown in Figure 26, where this is seen as a function of starting diamond grain size [35].

2.6.14. Grain boundary, inclusions and dislocations in PCD structures

The grain boundary is a region with a complex structure, about 1-2 unit cells wide, between two crystalline domains. It has a higher energy than the bulk crystal and, therefore, a reduction in the grain boundary area will reduce the free energy of the system. The diffusion of atoms allows the grain boundary to move so that atoms previously

residing in one grain become part of the other, causing it to grow at the expense of its neighbor.

During HPHT compaction of diamond grains, local pressures in the order of Mbars occur at the inter-particle contact zones and result in plastic deformation and/or fracture. Pressure over non-contacting surfaces is low, and graphitization occurs; such graphite-lined voids are infiltrated by liquid cobalt, which dissolves the graphite. At the point when the intergranular volume is at both high pressure and high temperature, carbon that has dissolved crystallizes out as diamond, prompting diamond intergrowth between the original grains.

Grain boundaries, inclusions, dislocations, and deformation are interrelated; this has been observed through Transmission Electron Microscopy. The inclusions contain graphite and the presence of the cobalt phase in PCD is easily confirmed by SEM/EDS analysis of the material. The cobalt in the diamond skeleton pores has an FCC structure matching that of the host diamond. The cobalt FCC structure, as opposed to the HCP structure encountered in pure Co, is a result of the presence of C and W which are in solid solution in this phase after cooling from the sintering temperature.

2.7. Mechanical properties of PCD

The mechanical (e.g. hardness, elastic constants, wear resistance and cleavage) properties of polycrystalline diamonds are highly dependent on orientation [25]. Crystals have a tendency to cleave effectively along the (111) weak planes [25]. Lammer investigated the mechanical properties of PCD and reported the results in his paper “Mechanical properties of polycrystalline diamonds” [25].

2.7.1. Transverse Rupture Strength

Transverse rapture strength is a measure of the strength of PCD compacts. It is a mix of shear strength, compressive strength and rigidity, and consequently it is utilized as a general measure of the toughness of diamond compacts. Transverse rupture strength depends on grain size and cobalt content of the matrix. It increases with decreasing grain size and increasing cobalt content [25]. Figure 27 illustrates Lammers’ results obtained on 8 samples of different grain sizes.

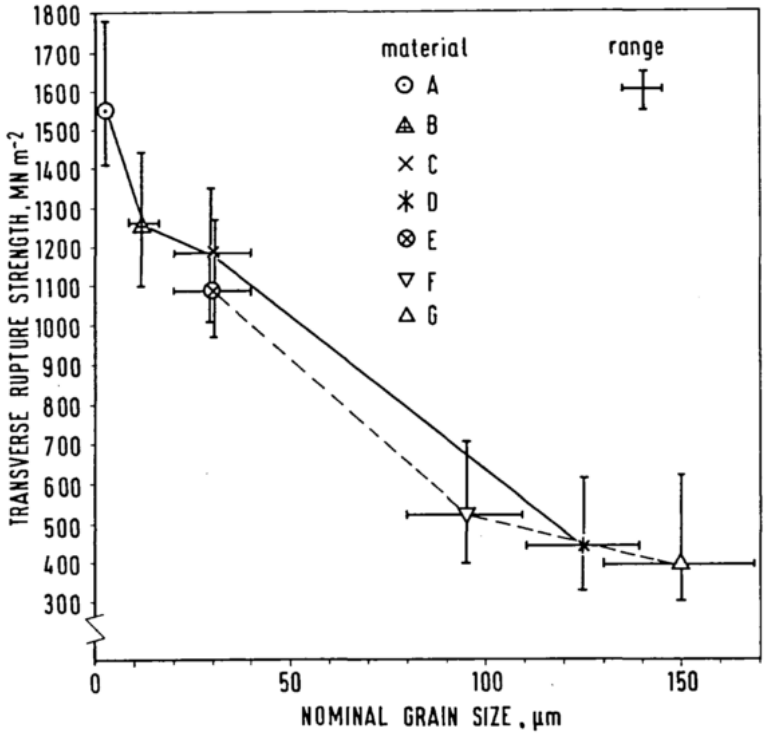


Figure 27: TRS of Polycrystalline Diamond layers as a function of grain size [25].

2.7.2. Hardness of PCD

Early measurements on the indentation hardness of natural diamond have been reviewed by Brookes [22]. Of note is the apparent lack of reproducibility in the quoted values from the early work. It is now known that the hardness of diamond compacts depends on factors such as orientation, diamond type, impurity content, load and shape of the indenter. Added to this is the fact that the indents themselves are small, thus giving relatively large experimental errors [22].

Hardness is the resistance to plastic deformation of a material. It is one of the most critical properties for PCD compacts applications. Hardness gives an evidence of the way of the composition and microstructure of the PCD, since it differs with amount and distribution of the metal phase, diamond grain size and level of porosity. PCD hardness is difficult to measure since the indenters used are also diamond. More often than not, these indenters are damaged during the measurement, making such measurements impractical for quality control purposes. The relationship defining hardness is given as:

$$H = \frac{P}{A} = \beta \frac{P}{d^2} \qquad \text{Equation 7}$$

Where H is the hardness, P – Applied load, A – Area of plastic contact, d – is the average of the lengths of the diagonals formed by the diamond indent and β – Constant dependent on the indenter geometry [48].

2.7.3. Density

The density, (specific gravity) of a sintered material is measured using the Archimedes technique and it is influenced by sintering parameters like temperature, pressure and time [49]. Sintered density is commonly used in the PCD manufacturing industry in order to identify the cobalt content of a particular grade. Densification is accomplished by means of eliminating porosity during sintering, and can be used as evidence of the viability of the sintering process. The density of a correctly sintered sample will be near the theoretical density (the density that the material would have if it had no voids) [48].

2.7.4. Fracture toughness (K_{1C})

Fracture toughness is the resistance of the material to crack propagation and is not dependent on the specimen size, geometry and finish [48]. The term K_{1C} is used to represent fracture toughness, and it refers to the plain strain fracture toughness. It is the critical value of stress intensity factor (K_{1C}) at a crack tip needed to produce catastrophic failure under uniaxial loading [48]. The fracture toughness is inversely related to hardness and, in the case of two phase composites with one of the two phases being metallic, increases with increased metal phase mean free path. The mean free path increases with increased metal phase amount and diamond grain size. Poor densification brings down the K_{1C} (750 to 1000MPa), since pores act as crack initiation and/or crack propagation sites.

The fracture toughness of a PCD compact is plotted against the starting diamond grain in Figure 28. The measurements points on the curve signify the mean of 10 specimens tested for fracture toughness under identical conditions. The scatter in data as measured by the standard deviation was less than 10% of the mean value. As the grain size increases, the fracture toughness of PCD layer increases and the rate of increase of grain size occurs at a very fast pace up to about 30 µm beyond which the rate of increase with respect to grain size reduces. Lammer's [25] measurement on PCD disks indicated similar trends and results considering the differences in manufacturing process used to produce PCD disks [35].

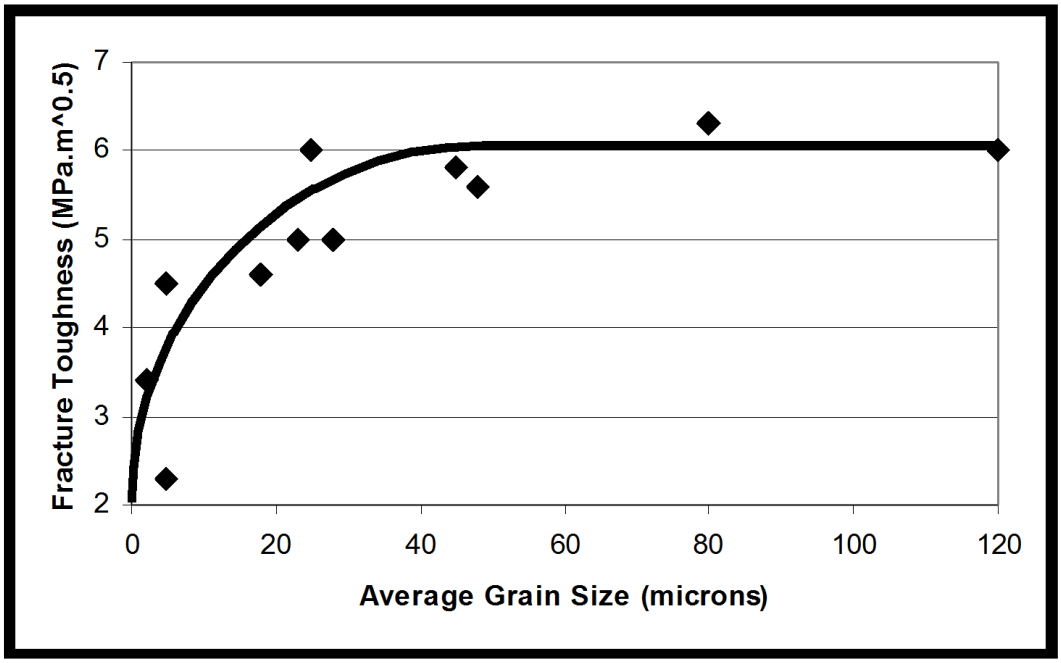


Figure 28: Diagram of PCD test specimen used for fracture toughness test [35].

2.8. Relationship of structure to properties in polycrystalline diamond

2.8.1. Influence of particle size on the strength of PCD materials

The decrease in the diamond grain size increases the strength of diamond composite materials [15]. However, ultra-fine particles have a high propensity to form agglomerates in the starting diamond powder, which sometimes is admixed with fine cobalt powder during the green compact preparation. Agglomerates of diamond grains can result in defects in the resulting PCD microstructure, adversely affecting the mechanical properties of these materials.

Therefore, it is essential to enhance the mixing procedures when processing sub-micron particles in the composite materials so as to accomplish uniform dispersion of phases all through the diamond composite matrix. Furthermore, the increase in the surface area of fine-grained materials increases their sensitivity to surface impurities, for example, oxygen, picked up from the atmosphere. This brings about challenges when cleaning the sub-micron grains.

2.8.2. Effect of particle size distribution on the strength of PCD materials

The grain growth is associated with the consumption of small grains by the larger ones so that the free energy is brought down by wiping out high free energy regions, i.e. grain boundaries. In this way, on account of multi-modal particle size distribution, grain growth can take place. Large grains in the microstructure of diamond composites are potential defects at which crack initiation can occur.

Therefore, a narrow particle size distribution is preferred for cobalt-PCD, and a bi-modal or multi-modal particle size may be utilized as part of diamond composites to enhance starting packing density. Depending upon the relative amount and distribution of large diamond particles, the sintered diamond composite TRS may decrease considerably [15].

2.8.3. Effect of microstructural homogeneity on the strength of PCD materials

The composite's homogeneity inside smaller scale volumes is the most significant parameter influencing its strength. In light of the Griffiths law of brittle fracture, agglomerated diamond grains and/or metal large inclusions will act as flaws, favouring crack initiation at lower applied stress, thus decreasing the strength of PCD composites. Hence, materials with a fine particle size and uniformly dispersed hard particles represent the desired microstructure, as far as high strength is concerned.

The agglomeration of particles for the most part occurs during milling and blending processes of fine and ultra-fine particles. Since blending efficiency reduces with decreasing particle size, the tendency towards formation of agglomeration may be avoided by the addition of suitable dispersing agent to the milling slurry such as WC balls during powder mixing. It has been found that attritor milling of ultra-fine diamond particles and metal phase materials results in a more homogeneous microstructure compared with that arrived at through planetary ball milling which is used to blend powders to very fine powders. In this manner, homogeneous distribution of particles in a diamond composite network can be accomplished.

2.9. Magnetism

Just as electrical phenomena were known to the ancient philosophers, so too were the phenomena that are placed under the title magnetism. The earliest known magnets were

iron minerals that occurred naturally. In this section, a brief explanation of the magnetic fields origin is given as well as the discussion of the different magnetic field vectors and magnetic parameters [50].

The basic principles and mechanisms that give rise to the phenomenon of magnetism are unobtrusive, and their understanding has evaded researchers up to generally modern times. Large portions of our cutting edge innovative technologies are dependent on magnetism and magnetic materials which comprise electrical power generators and transformers, radios, electric motors, computers, television, telephones, and sound and video systems parts.

2.9.1. Different types of magnetism

Magnetism falls under five categories, namely, diamagnetism, paramagnetism, ferromagnetism, antiferromagnetism and ferrimagnetism. In ferromagnetism, certain materials (such as iron) form permanent magnets, or get attracted to magnets. Ferromagnetism (including ferrimagnetism) is the strongest type: it is the only magnetism that typically creates forces strong enough to be felt, and is responsible for the common phenomena of magnetism in magnets encountered in everyday life.

The magnetic moments of atoms, usually related to the spins of electrons in materials that exhibit antiferromagnetism, align in a regular pattern with neighbouring spins (on different sub lattices) pointing in opposite directions. This is the same as in ferromagnetism and ferrimagnetism, in which they manifest an ordered magnetism. Sufficiently low temperatures show the existence of antiferromagnetic order, disappearing at and above a threshold temperature, which is the Néel temperature. Louis Néel is the first scientist to identify this type of magnetic ordering and therefore it was named after him.

For paramagnetic solid materials, the electron spin and orbital moments show incomplete cancellation result in each atom retaining a permanent dipole moment. If there is no external magnetic field applied, the atomic magnetic moments orientations are randomized, in a way no net macroscopic magnetization is retained by a piece of material. The formation of paramagnetism results from free rotation of atomic dipoles when they preferentially align with the existence of an external field, *H* as shown in Figure 29.

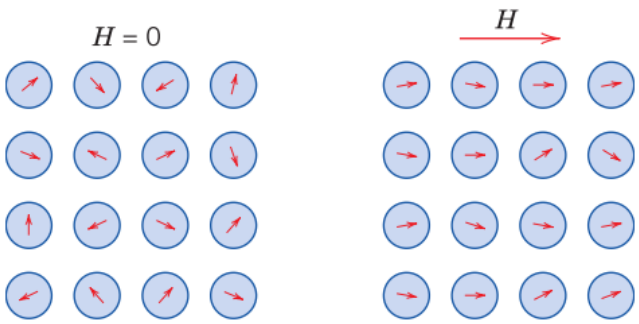


Figure 29: Schematic diagram of showing atomic dipole structure with/without an external magnetic field for a paramagnetic material [51].

These magnetic dipoles are acted on individually without the mutual interaction between adjacent dipoles. For as long as the dipoles align with the external field, they improve it, giving rise to a relative permeability μ_r that is greater than 1, and to a relatively small but positive magnetic susceptibility [51]. Diamagnetism shows a very weak form of magnetism that only exists when the external magnetic field is applied and is also non-permanent. It is induced when there is a change in the orbital motion of electrons resulting from the applied magnetic field. The amount of the induced magnetic moment is very small, and acts in an opposite direction to that of the applied field. Thus, the relative permeability μ_r becomes less than one (however, only very slightly), and the magnetic susceptibility becomes negative; that is, the magnitude of the B field within a diamagnetic solid is less than that in a vacuum.

The volume susceptibility χ_m for diamagnetic solid materials is of the order of 10^{-5}. Diamagnetic materials are attracted toward regions where the field is weak, when placed between the poles of a strong electromagnet. Figure 30 illustrates the atomic magnetic dipole structure of a diamagnetic material when the external magnetic field exist/non-exist; at this point, the atomic dipole moments is represented by arrows, though for the earlier discussion, arrows indicated only electron moments. In Figure 31, a material that exhibits diamagnetic behaviour shows that *B* is dependent on the external field *H*. All materials have diamagnetism in them; but because of its weakness, it can only be detected when there is no other form of magnetism existing.

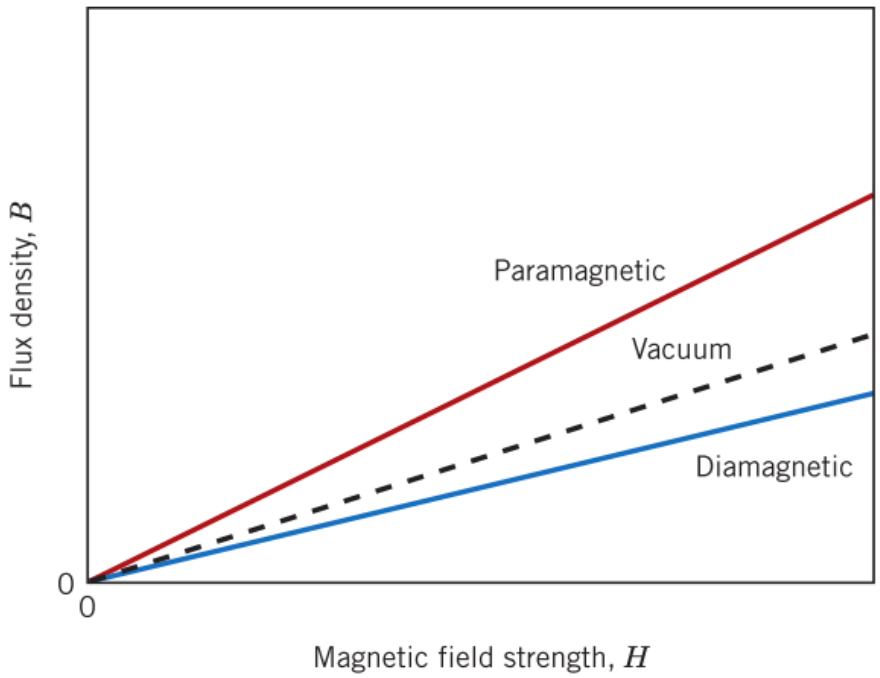


Figure 30: Schematic illustration of the flux density *B* against the magnetic field strength *H* for diamagnetic and paramagnetic materials [51].

This research work focuses on magnetic properties of the metallic cobalt phase (which is ferromagnetic) in PCD, therefore ferromagnetism will be explained in relation to the objectives of this research work.

Magnetization in a crystal points in specific crystallographic directions, those corresponding to energy minima. Deviations from these directions raise the energy of the system and this directional preference is denoted as “magnetic anisotropy”. On the other hand, classical dipolar energy is the energy of interaction between two dipoles and it is so small that it can be neglected in discussing the energy of a system of magnetic dipoles. Ferromagnetic materials are characterised by the existence of coupled, atomic magnetic dipoles distributed throughout their volume.

The strong coupling between atomic moments makes it possible to define a macroscopic magnetization vector ***M*** as a vector sum of the atomic dipole moments per unit volume and this vector is related to the magnetic induction ***B*** and magnetic field ***H*** of electromagnetic theory by the definition $\boldsymbol{B} = \boldsymbol{H} + 4\pi\boldsymbol{M}$. The interaction of magnetization vector ***M*** with the electric and magnetic fields ***E*** and ***B*** respectively is described by Maxwell’s equations:

$$\nabla \times \boldsymbol{E} = -\frac{1}{c}\frac{\partial \boldsymbol{B}}{\partial t}\,; \qquad \nabla \cdot \boldsymbol{B} = \mathbf{0}$$ Equation 8

2.9.2. Magnetic Dipoles

Magnetic forces are produced by moving particles that are electrically charged; such forces are additional to any electrostatic forces that may be present. Generally it is helpful to consider magnetic forces in terms of fields. The force's direction can be shown by drawing Imaginary lines of force at positions in the vicinity of field's source [51]. Magnetic dipoles may be considered as little bar magnets made out of north and south poles rather than positive and negative electric charges. In the present discussion, magnetic dipole moments are represented by arrows, as illustrated in Figure 32. Magnetic dipoles are impacted by magnetic fields in a similar manner in which electric dipoles are influenced by electric fields. The field force applies a torque on the magnetic dipoles within a magnetic field that tends to align them in the direction parallel to the field. An example is the lining up of a magnetic compass needle with the earth's magnetic field.

2.9.3. Ferromagnetism

Ferromagnetism refers to the spontaneous parallel alignment of unpaired electron spins in a solid, without the existence of an external magnetic field as shown in Figure 31 [52]. The unpaired electron spins of atoms in a solid interact through exchange integrals of their adjacent electron clouds, (normal interaction between unpaired spin localised electron orbitals of 3d elements). This interaction also occurs through other conduction electrons, in the case of highly localised electron clouds, as is the case for 4f group elements, i.e. rare earths (this type of magnetic interaction is dealt with by the RKKY theory (Ruderman-Kittel-Kasuya-Yosida). Parallel to the exchange integral interactions, there is always a plain magnetic dipole interaction. However, the energy related to this interaction is several orders of magnitude lower than that related to exchange interactions. Other forms of interactions that give rise to magnetic order are double-exchange and super exchange [53].

Ferromagnetism is exhibited by several solids containing 3d (iron, nickel, cobalt) as well as 4f elements (i.e. the rare earths). As discussed, this type of magnetic order is a result of quantum mechanical interactions between the orbitals of unpaired electrons, in combination with the Pauli Exclusion Principle. There is additionally an orbital magnetic

moment contribution that is less in correlation to the spin moment and is given by Equation 9.

$$\mu = \frac{q}{mc} S \qquad \text{Equation 9}$$

where, μ is the magnetic moment, q is the charge of a particle, m is the mass of particle, c is the speed of light, and S is the electron spin angular momentum.

The saturation magnetization is equal to the product of the net magnetic moment for every atom times the quantity of atoms present. For cobalt, the net magnetic moment per atom is 1.72 Bohr magnetons.

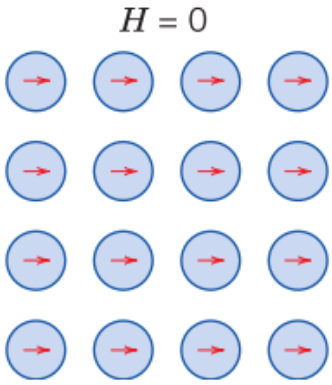


Figure 31: Schematic diagram of the mutual configuration of atomic dipoles for a ferromagnetic material [51].

2.9.4. The Temperature Influence on Magnetic Behaviour

Temperature can likewise impact the magnetic qualities of materials. Raising the temperature of a solid result in an increment in the magnitude of the thermal vibrations of atoms, but also tends to raise the energy of the spin assembly by some of them populating the “down” orientation simply by thermal activation. This process tends to randomize the spin directions, up to the point where there are as many “up” spins as there are “down” ones. At that point all permanent magnetization is lost. The temperature at which this happens is called the Curie point or Curie temperature. The magnitude of this temperature has a strong correlation with the strength of the exchange interaction [51].

For ferromagnetic, antiferromagnetic, and ferrimagnetic materials, the atomic thermal motions can overcome the coupling forces between the atomic dipole moments, bringing

on some dipole misalignment, irrespective of whether an external field is available. This results in a decrease in magnetic saturation for both ferro-and ferrimagnets. The magnetic saturation is most extreme near absolute zero, at a temperature in which the thermal vibrations are at minimum. When the temperature is raised, the magnetic saturation decreases progressively and eventually drops to zero at the Curie temperature [51].

2.9.5. Magnetic Saturation

Magnetic saturation is the maximum magnetization that can be induced in a material by a strong magnetic field. For WC-Co-PCD, the saturation magnetization in Co diminishes linearly with increasing W concentration, and is not influenced by the amount of C present in the solution. The solubility of W in the Co is subject to the amount of C in the material [54]. The lower the C content in the metal phase of PCD, the higher the W concentration, thus reducing the magnetic saturation value [54]. Low magnetic saturation values are associated with eta phase in the microstructure. Thus, magnetic saturation is an indirect measure of the C content in the PCD materials prepared by HPHT on WC-Co substrate.

Each material has a defined and constant magnetic saturation value. Magnetic saturation measurement allows the magnetisable content of a material to be determined. Magnetic saturation measurements are not dependent on the shape and size of the specimen. If the material contains one magnetisable component (cobalt), as is the case with hard metals, then its content in percent can be determined only if Co is pure. If there is W present, the magnetization decreases [55].

In hard metal manufacturing, the significance of the ratio of the ferromagnetic cobalt content before and after the sintering process is very high [55]. The composition of the cobalt phase and cobalt ferrous compounds can be deduced from the measurements before and after sintering.

2.10. Coercivity

Coercivity is the magnetic field required to demagnetize a material after it has been magnetised up to saturation. The coercive force measurements provide a means of characterizing the grain size. In the case of the cemented tungsten carbide, WC-Co interface limits the movement of the magnetic domain walls within the ferromagnetic Co binder-phase. Therefore, the magnetic field required to restore zero magnetization to a

magnetically saturated WC–Co hard metal is proportional to the interfacial area between the Co binder-phase and the WC hard phase and this in turn is associated with the WC grain size [56]. Coercivity increases with decreased cobalt mean free path, and hence is used as an indirect measure of the degree of sintering, cobalt distribution and diamond grain size [57]. The cobalt mean free path is decreased using multi-modal diamond mixes, i.e. improving the packing by deliberately adding smaller particles.

Thus the modality of the diamond starting feed also plays a role then. Generally, larger diamond grains have thicker cobalt mean free (CMF) paths between them, and the same applies to finer diamond grains where the CMF is smaller [58]. Therefore, for PCD compacts, coercivity is high when the Co content is high and/or diamond grain size is fine and low when the Co content is low and/or the diamond grain size is coarse [54]. Free carbon, which also leads to increased diamond grain growth [57], also reduces the coercivity.

Magnetically hard materials having high coercivity are referred to as ferromagnetic materials, and are utilized in the making of permanent magnets. Applications of permanent magnets include electric motors, magnetic separation, and magnetic recording media [59].

The coercivity of PCD is measured by a coercimeter. This device comprises a coil and measurement and control electronics coupled to it. The control electronics are designed to pass a current through the coil so that a magnetic field is generated. During testing, the magnetic field generated by the coil magnetizes the PCD sample approximately to saturation. The same electronics measure the degree of magnetization of the sample through a magnetization sensor. After saturation has been achieved, the magnetic field is progressively reversed until the magnetization is zero. The field at which the magnetization is zero is called the coercive force, or the coercivity.

The magnetization measured at zero magnetic field is called remnant magnetization and is an important quantity in the field of geoscience and, more importantly, industrial magnets. The coercive force is also referred to as the magnetic hardness of the material. The reversal of the applied field is continued until the magnetization of the sample is completely reversed to saturation in a direction opposite to the initial one. The applied

field is then driven again in the direction it originally had. The process is repeated until saturation in the original direction has been achieved. The resulting graph plotting magnetization versus applied magnetic field is called the hysteresis loop and is schematically given in Figure 32.

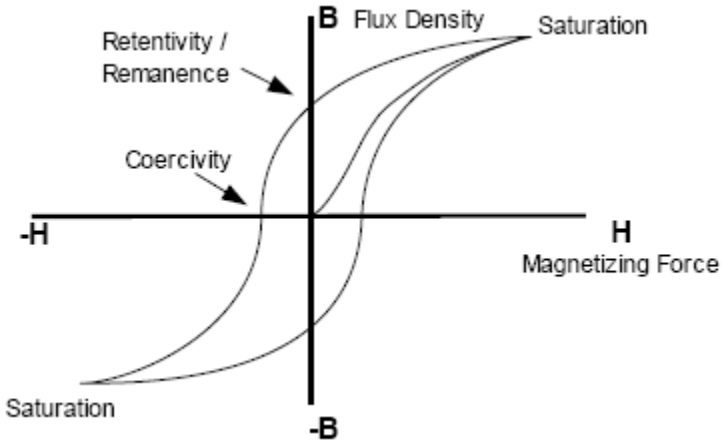


Figure 32: The area contained within the hysteresis loop has energy units and denotes the energy consumed during one complete reversal of the magnetization and back. A large hysteresis loop is desirable in hard permanent magnets, while the opposite applies to electrical transformer cores [60].

The flux density and applied magnetic field relationship is represented by the expressions in equation 10 as:

$$H = \frac{B}{\mu_0} - M \qquad \text{Equation 10}$$

Where, B is magnetic flux density, μ_0 is the magnetic susceptibility

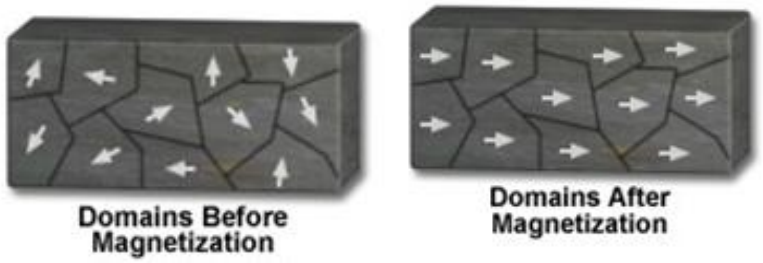
In terms of the H-field, Ampere's law gives:

$$\oint \vec{H}.d\vec{l} = \oint \left(\frac{\vec{B}}{\mu_o} - \vec{M}\right).d\vec{l} = I_{\text{tot}} - I_{\text{b}} = I_{\text{f}} \qquad \text{Equation 11}$$

where I_f represents the 'free current' enclosed by the loop so that the line integral of H is not dependent on the bound current, I_b, at all. From these expressions, ***B*** represents magnetic flux density. ***H*** represents magnetic field strength [61].

2.11. Magnetic Domains

Magnetic domain is an area in a material in which the magnetic fields of atoms are clustered together and aligned. Figure 33(a) and (b) indicates magnetic domains in the metal material represented by the arrows. One can think of magnetic domains as small magnets within a material. In an un-magnetized object, all the magnetic domains are pointing in different directions as in Figure 33a. The magnetic domains occupy sub-regions of a grain of a magnetic polycrystalline material. The magnetization in each domain points in such a crystallographic direction that minimizes the magnetic anisotropy energy. But, when the metal became magnetized, which is what happens when it is rubbed with a strong magnet, all like magnetic poles line up and pointed in the same direction shown by Figure 33b. The metal becomes a magnet. It would quickly become un-magnetized when its magnetic domains return to a random order. The latter description is approximate, as all domains in each single-crystal-grain orient themselves in the magnetic anisotropy minimizing direction closest to the applied magnetic field direction.



(a) (b)

Figure 33: Alignment of domains in metals (a) before magnetization and (b) after magnetization [62].

For magnetic domains to form, materials need to have magnetic ordering in which their dipoles align spontaneously resulting from the exchange interaction. Such materials are the ferromagnetic, ferrimagnetic and antiferromagnetic. As for the Paramagnetic and diamagnetic materials, their dipoles do not spontaneously align, and they do not have magnetic domains in which the dipoles will align when an external field is applied.

2.11.1. Development of domain theory

The French physicist Pierre-Ernest Weiss developed the magnetic domain theory in 1906 and suggested the existence of magnetic domains in ferromagnets. He suggested that

large number of atomic magnetic moments (typically 10^{12}-10^{18} atoms) are parallel aligned. The direction of alignment of domains varies in a random manner, even though certain crystallographic axis are preferable by the magnetic moments, called easy axes. The reason for the spontaneous alignment of atomic moments within a ferromagnetic material was explained by Weiss, who also came up with the Weiss mean field. He anticipated that a given magnetic moment in a material experienced a very high effective magnetic field due to the magnetization of its neighbours. In the original Weiss theory, the mean field was proportional to the bulk magnetization ***M***, so that

$$H_e = \alpha M \qquad \text{Equation 12}$$

Where H_e is the mean field and α is mean field constant. The ferromagnets do not experience such due to the magnetization variability from domain to domain. Therefore, the field of interaction is

$$H_\mathrm{e} = \alpha M_\mathrm{s} \qquad \text{Equation 13}$$

Where M_s is the magnetic saturation.

The microscopic origin of the Weiss field became more understandable by quantum theory. The parallel (in ferromagnets) or an anti-parallel (in anti-ferromagnets) state of neighbouring magnetic moments was favoured by the exchange interaction between localized spins [63].

2.11.2. Domain Structure

Iron is one of the magnetic material that divides spontaneously into isolated domains, instead of existing in a state where the magnetization is in the same direction throughout the material, in which case internal energy is minimized. A huge area of ferromagnetic material having a constant magnetization throughout will induce a large magnetic field that extends into the space outside its region. This needs a lot of magneto static energy stored in the field. For such energy to be reduced, the sample splits into two domains, with the opposite directions of magnetization in each domain.

The field outside the material is reduced when the lines of magnetic field pass through each domain in loops in opposite directions. For further reduction of the field energy, each of the domains also splits, and produces smaller parallel domains with magnetization in alternating directions, as well as smaller field amounts outside the material. However, splitting of large domains into smaller ones does not usually form the domain structure of actual magnetic materials. The equilibrium domain structure simply appears when a sample is cooled below the Curie temperature. Nonetheless domains can be split, and the explanation of splitting of domains is regularly used to reveal the energy trade-offs in the formation of domains.

2.11.3. Domain Size

In section 2.11.2, it was explained that a too big on domain is unstable, and will further split into smaller domains. Nevertheless a domain which is very small will be stable and will not divide, and hence the size of the domains created in a material will be determined. This size is dependent on the residual energies that occur within the material. Whenever a magnetization region splits into two domains each time, a "domain wall" is created between the domains, and these adjacent magnetic dipoles (molecules) with magnetization pointing in different directions are formed. The creation of the magnetization by exchange interaction is a result of the force which tends to align nearby dipoles making them to align in the same direction. An energy is required in order to force the dipoles that are adjacent to point in different directions. As a result a domain wall requires extra energy, called the "Domain wall energy", which is relative to the area of the wall.

Thus when a domain splits the remaining amount that the energy is reduced by is equal to the change in energy saved between the magnetic field energy, and the extra energy required to create the domain wall. The field energy is found to be proportional to the domain size cube, while the domain wall energy is proportional to the domain size square. As the domains contract, the remaining energy saved by splitting decreases The domains keep separating into smaller domains until the energy cost of creating an additional domain wall is just equal to the field energy saved. Then the domains of this size are stable. The domains are microscopic in size in most materials, they are around 10^{-4} - 10^{-6} m.

2.11.4. The Grain Structure

Grain structure describes the magnetic domain arrangement in a perfect crystal lattice, which is the same structure that would be found in a single crystal of iron. Nonetheless most magnetic materials are polycrystalline, and are made up of tiny crystalline grains. Such grains are therefore not similar to domains. Each grain represent a little crystal, having the crystal lattices of isolated grains oriented in random directions. As in most materials, a bigger domain has the ability to contain several domains. . Each crystal has typically several "easy" magnetization axes, determined by the crystal symmetry, these are divided into domains with the magnetization axis parallel to these axes, in alternate directions.

2.12. Cobalt

2.12.1. Ancient History of Cobalt

The use of cobalt goes back to ancient times. Its use in shading of glass and coatings was documented. A necklace comprising various blue glass beads coloured with cobalt was found in the north west of Persia, dating approximately 2250 B.C [64]. During those times, cobalt was utilized for decorating Egyptian statuettes; the specialty of decorating with cobalt outlasted the old civilisations. The Portland vase, differently reported as having been made in 100 B.C. and also, in 100 A.D, is viewed as the finest example of late Roman glass-blowing method; spectrophotometric studies have demonstrated that cobalt was the shading agent in the blue-and-white carved glass [64].

2.12.2. Metallic Cobalt and Cobalt alloys

Preceding 1914, for all intents and purposes no cobalt metal was produced; cobalt oxide was the form in which this element was then marketed. A US patent was granted in 1907 to E. Haynes, a vehicles maker, on cobalt chromium composites containing from 40 to 90 % cobalt; Haynes had been experimenting with cobalt-chromium alloys as early as 1897. It was asserted that these alloys, named stellites, were corrosion resistant, were usable as metal-working instrument materials and could substitute platinum in some applications [64]. In 1913, Haynes was awarded licenses on cobalt-chromium-tungsten compounds, additionally named stellites to be utilized for rapid cutting. R Bottger, in 1942, was most likely the first to demonstrate that cobalt could be electroplated on metals [64]. A British patent was awarded to E.D Nagel in 1870 for plating with cobalt, nickel or both metals in

a mixed form. K. Honda disclosed cobalt-containing magnet steel in 1917 and after four years, a superior permanent magnet material, containing 35% cobalt steel, was produced. In 1935, the Alnico arrangement of magnet compounds (iron, nickel, cobalt, and aluminium) were created at the same time by General Electric Company situated in the United States and Tukushichi Mishima in Japan [64].

Cobalt-based super alloys use up the majority of the cobalt produced. The capability of these alloys to withstand high temperatures without deterioration in their mechanical properties makes them ideal for utilization in gas turbines and jet airplane engines; nevertheless nickel-base single crystal alloys exceed them in this regard. Cobalt-based alloys are corrosion and wear-resistant. The first decade of 19th century was the time were the development of the wear-resistant cobalt alloys started with the stellite composites, which are cobalt-chromium compounds with changing W and C content [65].

2.12.3. Physical properties of Cobalt

Cobalt is a ferromagnetic metal that has a specific gravity of 8.9. The specific gravity has no SI units as it is derived from the ratio of densities. The Curie temperature of cobalt is 1,115 °C and the magnetic moment is 1.6–1.7 Bohr magnetons for every atom. The relative permeability of cobalt is 66% to that of an iron, a melting temperature of 1495^{o}C, and theoretical density of 8.9g/cc. Its Young's modulus is 207 GPa, thermal expansion coefficient of 16µm/m.K and hardness of ~1.043 GPa [66]. Cobalt has two crystallographic structures: FCC (α-Co) and HCP (ε-Co). The temperature at which the two structures transit between the HCP and FCC structures is 450 °C. The allotropic change temperature is dependent of on the purity and the temperature change rate, yet, the free energy difference between the two phases is small to the point that irregular intergrowth of the two is common [65].

Cobalt is not a naturally occurring pure metal; however it is an element found in more than nearly 100 naturally occurring minerals, that includes various arsenides, sulfides, hydrates, oxides and sulfoarsenides [67].

For the highest purity Co (~99.998%) and slow temperature changes, the transformation temperature ranges between 417 ^{o}C - 421.5^{o}C [68], [69]. Generally, a mixture of roughly

the same amount of both allotropes exists in cobalt powders, but during milling, the amount of hcp (ε-Co) increases to up to 100% [70].

2.12.4. Chemical Properties of cobalt

Cobalt is a reducing metal that is protected by passivating oxide film from oxidation. It is easily attacked by sulphur and halogens. When Co is heated in oxygen it produces cobalt oxide (Co_3O_4) which releases oxygen at 900 °C to produce the cobalt monoxide (CoO). At normal Standard Temperature and Pressure (STP), cobalt slowly reacts with mineral acids, and also reacts extremely slowly with moisture, however it does not react with dry air. It is inert in nitrogen gas (N_2) and hydrogen gas (H_2) or even when it is subjected to heat, but then it does react with phosphorus, boron, carbon, sulphur and arsenic [65].

Pure cobalt does not dissolve in water and soil, and can stay unchanged for years at room temperature. Fine Co powders prepared by hydrogen-reduction technology are easily oxidized to cobalt oxide and can even self-ignite in air. So the fine Co powders must be carefully preserved in a vacuum or an inert gas container.

As a weakly reducing metal, cobalt is easily attacked by halogens and sulphur, and also dissolved easily and quickly in HCl, H_2SO_4 and HNO_3 acid solutions. Cobalt forms many intermetallic compounds by solid-dissolving many metal and non-metal atoms. This metal can easily infiltrate many ceramic powder preforms (WC, TaC, TiC, ZrC, TiN, Al_2O_3, cBN, diamond), and for almost all carbides the wetting angles are lower than 50 °, so it is often used as an additive in the above ceramic-metal composites [71].

2.12.5. Composition of Cobalt material

The addition of cobalt to diamond powder preforms makes liquid phase sintering possible at temperatures just above the melting point of that metal. Sintering in the absence of a liquid phase sintering aid would only take place at much higher temperatures in order to sufficiently activate the diffusion processes required for solid state sintering. Cobalt is introduced into the diamond preform through infiltration from the WC-Co substrate during sintering into PCD. Therefore the addition of cobalt to diamond preforms used for the making of PCD composites has the following advantages:

- It is a low-melting point and, as a liquid transmits pressure throughout the volume of the preform thus inhibiting diamond to graphite transformation.

- Carbon is highly soluble in Co, thus greatly aiding the solution-precipitation process required for the liquid phase sintering process.

2.12.6. Production of Cobalt

Pure cobalt is produced by reductive smelting. G Brandt was the first person to prepare pure cobalt in 1735. Cobalt was produced through the reduction of cobalt oxide in hydrogen at temperatures ranging from 600 ^{o}C to 700 ^{o}C, as shown by Equation 14 [69], [72].

$$Co_3O_4 + 4H_2 \rightarrow 3Co + 4H_2O \qquad \text{Equation 14}$$

Co powders greater than 2 μm in particle size were achieved from the above process, and if finer grains are required, an additional milling step had to be added to the production [69]. As a result, new methods have been developed and are used for the production of spherical and non-agglomerated cobalt powders of both micron and submicron sizes. The process uses reduction of cobalt hydroxide, $Co(OH)_2$, by a mixture of ethylene-glycol and diethylene-glycol, as shown in Figure 34. Micron sized cobalt powders are produced through homogeneous nucleation and growth from the $Co(OH)_2$ solution.

The submicron powders are obtained either by seeding the reactive medium with foreign metal nuclei, (silver or palladium) to induce heterogeneous nucleation, or by raising the reaction temperature [69].

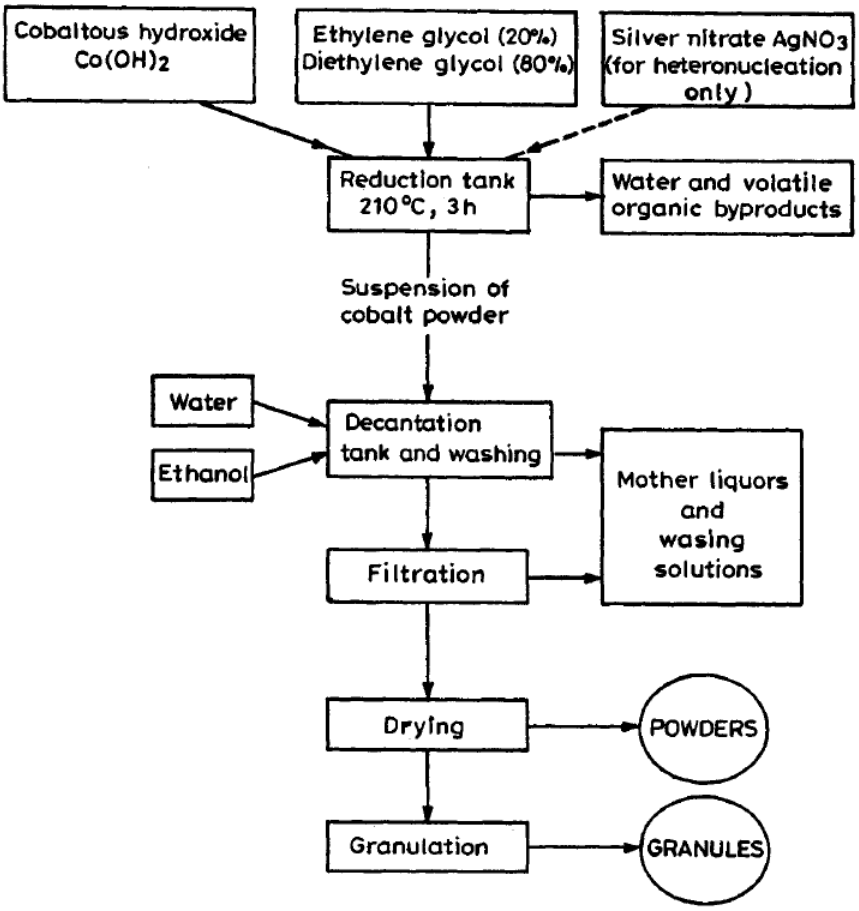


Figure 34: Flow diagram of the production of cobalt powders and granules [69].

2.12.7. Magnetic properties of Cobalt

The ferromagnetic properties of the cobalt phases (cobalt, nickel and iron) in the PDC make it possible to perform quick non-destructive quality control tests such as coercivity and magnetic saturation tests [73].

Ferromagnetic cobalt materials show a long-range magnetic order at the atomic level causing the unpaired electron spins to line up parallel with each other in a domain. The magnetic field is intense within the domain, but in a bulk sample the material will usually be un-magnetized due to random orientation of domains with respect to one another. Ferromagnetism manifests itself when a small externally imposed magnetic field, say from a solenoid, causes the magnetic domains to align themselves parallel with each other; at that point the material is said to be magnetized. The resulting magnetic field, added to the driving magnetic field will result in a total field increased by a large factor which is

usually expressed as the relative permeability for the material. Figure 35 shows the extent at which abrasion resistance is influenced by diamond grain size and cobalt content.

The coercivity and magnetic saturation tests give information about the effectiveness of the sintering process and some information about the microstructure [69].

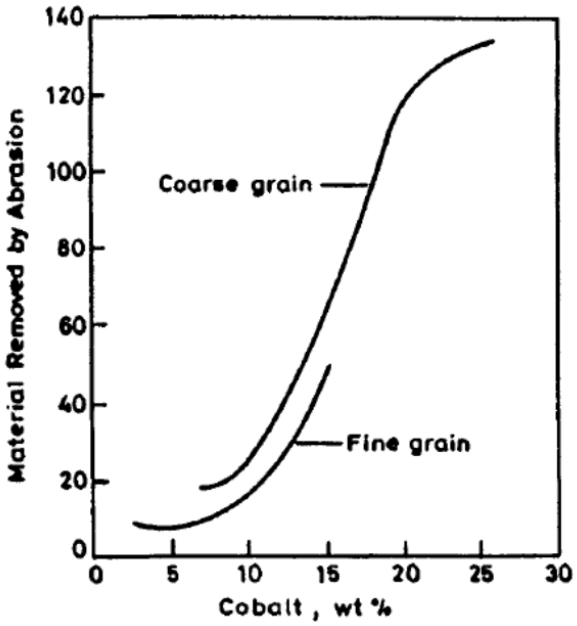


Figure 35: Influence of grain size and Co content on the abrasion resistance of WC-Co [69].

2.12.8. Applications of cobalt

Cobalt is used as one of the ingredients in the production of certain high performance alloys, in which case its application is as a free metal [74]. Owing to the excellent chemical, physical, and mechanical properties, cobalt is widely used in fabricating various alloys (which are used as high-temperature and wear resistant components, dies, saws, cutting tools) by powder metallurgy technology. The resulting materials are super alloys, high speed steels, cemented carbides, polycrystalline diamond (PCD), and polycrystalline cubic boron nitride (PCBN). Cobalt in the above alloys is usually used as an additive, an alloying element or a binder [74].

Cobalt is the most commonly used metal liquid phase sintering aid for PDC manufacture because of its excellent carbon solubility and resultant diamond wetting properties. The capillary action of cobalt during sintering allows the achievement of high densities possibly due to the convenience of sintering on a WC-Co substrate [75].

Significant amount of FCC cobalt is present in sintered PDC hard metals at room temperature. The transformation between the two phases is martensitic in nature [76], [77]. The cobalt transformation is also affected by the amount of tungsten carbide dissolved in the metal phase and the cobalt mean free path. Hard metals with a finer microstructure have been found to have a higher FCC/HCP ratio than conventional grades; this is due to the higher solution of tungsten in the metal phase [78].

2.13. Material Characterization of PCD

Characterization of a material refers to the process by which a material's structure is analysed and its properties are measured. A few definitions define the term's that characteristics utilization to techniques which study the microscopic structure and properties of materials. Material testing techniques are discussed further for PCD materials.

2.13.1. Scanning electron microscope (SEM)

SEM is an electron microscope that delivers high resolution images of a specimen by scanning it with a focused beam of electrons to inspect the microstructure of the surface of a material. The SEM produces higher resolution images and can go to higher magnification and greater field depth. The electrons created by the SEM interact with electrons in the specimen, and scatter from the surface. The scattered electrons contain data about the sample's surface topography and composition. The SEM delivers different types of signals that include back-scattered electrons (BSE), secondary electrons (SE), light (cathodoluminescence) (CL), characteristic X-rays, specimen current and transmitted electrons [79].

All SEM systems use secondary electron detectors as primary detectors, however it is rare that a single machine would have detectors for all possible signals. The interactions of the electron beam with atoms at or close to the surface of the sample generates signals that are passing through the sample during analysis. In the most common or standard detection mode, secondary electron imaging (SEI), the SEM can produce very high-resolution images of a sample surface, revealing details close to 1 nm in size. SEM micrographs have a large field depth that produces a characteristic three-dimensional appearance. To obtain good quality results, surfaces need to be ground and polished to

very smooth finishes for back scattered electron imaging, quantitative X-ray analysis, and X-ray mapping of specimens. Specimens that undergo energy-dispersive-spectroscopy (EDS) analysis are often coated in the carbon or gold. As a general rule, metals need not be coated prior to imaging in the SEM because they are conductive and surface charging effects are minimized [79].

2.13.2. Scanning Process and Image Formation

For a scanning process and image formation to occur, an electron beam is projected from an electron gun-fitted with either a tungsten filament, or LaB_6 or CeB_6 cathodes. The utilization of tungsten target in electron guns is preferred because that it has of the lowest vapour pressure and has the highest melting point of all metals, thus allowing it to be heated for electron emission, and also because of its low cost.

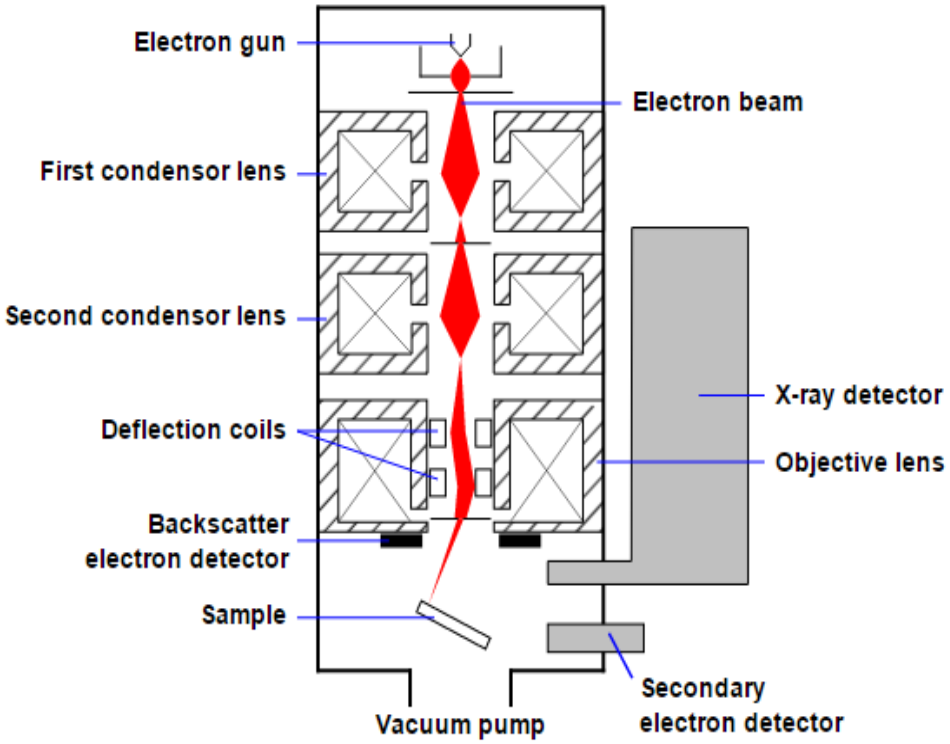


Figure 36: Schematic representation of an SEM [79].

Figure 36 shows a schematic diagram of the electron beam which typically has an energy ranging from 0.2 keV to 40 keV, and is focused by one or two condenser lenses to a spot about 0.4 nm to 5 nm in diameter. There are pairs of scanning coils that allow a beam to pass through in the electron column, typically in the final lens, which deflect the beam in the x and y axes so that it scans in a faster fashion over an area of the sample surface

2.13.3. Detection of Secondary Electrons

The secondary electrons are identified by an Everhart-Thornley detector, which is a type of scintillator-photomultiplier framework. The secondary electrons are initially gathered by pulling them towards an electrically one-sided matrix at around +400 V, and after that further accelerated towards a phosphor or scintillator positively one-sided to around +2,000 V. The accelerated secondary electrons are now adequately energetic to cause the scintillator to emit flashes of light. The light is taken to a photomultiplier outside the SEM column by means of a light pipe and a window in the wall of the specimen chamber. The amplified signal generated by the photomultiplier is shown as a two-dimensional intensity distribution that can be seen and captured on a simple feature show, or subjected conversion and showed and saved as a digital picture.

2.13.4. Detection of Backscattered Electrons

Backscattered electrons (BSE) comprise electrons starting in the electron beam that are reflected or back-scattered out of the specimen interaction volume by elastic scattering from the specimen. The size of the interaction volume is dependant not only on the ability of the sample to decelerate the electrons but also the incident energy of the electrons that requires absorbing. It is apparent that in the case of PCD a 15keV beam interacts with a substantive volume of diamond approaching the micron length scale before the electrons finally come to rest.

It is thus generated from a volume orders of magnitude bigger than the nm sized incident beam as well as from a considerable depth into the sample. This has clear implications on the generated signal and the subsequent image. The interaction volume also depends strongly on the atomic number of the specimen, and its size is drastically reduced with increasing atomic number. Two factors limit the size and shape of the interaction volume: (1) energy loss through inelastic interactions and (2) electron loss or backscattering through elastic interaction.

Since elements with high atomic number Z scatter electrons more than light elements (low atomic number), they are brighter in the image generated. BSE are utilized to detect contrast between areas with distinctive chemical structures. The Everhart-Thornley detector, which is ordinarily situated to the other side of the specimen, is inefficient for the detection of backscattered electrons on the grounds that few of such electrons are emitted

in the solid angle subtended by the detector, and in light of the fact that the emphatically biased detection grid has little capacity to pull in the higher energy BSE. Dedicated backscattered electron detectors are situated above the sample in a "doughnut" type arrangement, concentric with the electron beam, maximizing the solid angle of collection. BSE detectors are typically either of scintillator or of semiconductor types [80].

2.13.5. X-Ray Diffraction Technique

X-ray diffraction (XRD) is a standout amongst the most intense systems utilized for qualitative and quantitative investigation of crystalline substances. It is an instrument utilized for identifying the atomic structure of a crystal. The crystalline structure causes a beam of incident x-rays to diffract into numerous particular directions. By measuring the angles and intensities of these diffracted beams, a crystallographer can create a three-dimensional picture of the rows and planes of atoms that make up a regular pattern of the crystal arrangement.

The effects of X-ray diffraction in crystalline materials are a function of the nature of the atoms and their atomic arrangement. The method is capable therefore of measuring interatomic spacing changes resulting from alloying of specific phases and of detecting the presence of individual phases in a multi-phase material. In addition, disturbances in the order from the ideal atomic packing (strain) can also be evaluated. X-ray diffraction can also be used to determine the amount of dissolved elements in the cobalt phase of PCD.

CHAPTER 3 RESEARCH OBJECTIVES

3.1. Main Objective

The main objective of research was devoted to the study of the magnetization of the metallic cobalt phase in PCD, as a function of PCD processing conditions and resulting microstructure. This was largely an experimental work aimed at a broad description of PCD compacts sintering and the effect of metal sintering aid infiltration into PCD.

3.2. Detailed Objectives:

- To investigate the distribution of metallic phase in the PCD microstructure using image analysis techniques. This includes a number of relevant features such as Diamond grain size distribution, diamond skeleton pore-size and pore-size distribution, cobalt phase mean free path and cobalt phase contiguity.
- Measure the magnetic saturation as well as the magnetic coercivity of the PCD studied.
- Measure the metal content on each variant of syndrill cutters studied in this work by determining the density of PCD layer with no carbide substrate present.
- Characterise the phase and chemical composition of the metal phase in the PCD, by means of EDS, XRD and Inductive Coupled Plasma (ICP).
- To investigate the impact different grades of diamond feedstock powder have on magnetic properties of cobalt phase after sintering.
- To investigate the relationship between starting diamond particle distribution, substrate microstructure, sintering conditions and the resulting PCD microstructure with particular emphases on the metallic PCD phase's magnetic properties.

3.3. Important Questions

- Does the diamond grain size have impact on metal phase distribution in PCD?
- Can magnetic properties measurements of PCD compacts be used accordingly by industry to assess material consistency and performance?

- How does the presence of precipitated phases of WC in PCD after sintering affect the cobalt magnetic saturation and moment values as well as the material performance?

3.4. Hypotheses

- The magnetic saturation can be used for quality control and to estimate Co-W-C metal-phase composition.
- Coercive field strength can also be used for quality control and to estimate WC grain size in the substrate.
- If correctly interpreted, these parameters could have a direct link to the cobalt composition and hence overall material properties and performance.
- Could a combination of density, saturation and coercivity, allow one to derive metal phase volume fraction and Co mean free path?

CHAPTER 4 EXPERIMENTAL METHODOLOGY

The detailed experimental procedure followed to prepare and characterize the PCD compact in this research is presented in this chapter, along with mixing and characterisation of diamond powders and Cobalt.

4.1. Starting powders composition and their characterization

4.1.1. Constituents diamond powder composition

Figure 37 shows the Malvern Mastersizer™ used to analyse particles size. This technique uses Mie and Fraunhofer scattering theory of particle size analysis. The instrument measures particles size ranging from 0.02 µm to 2000µm producing an accuracy better than 1% and reproducibility better than 1% variability depending on the sample preparation.



Figure 37: Malvern Mastersizer 2000 for particle size analysis.

The Mastersizer 2000 measures the particles size using the laser diffraction technique. For the measurements to occur, the intensity of light scattered as a laser beam passes through a dispersed particulate suspension sample was measured. The data obtained was then analysed to calculate the particle size that created the scattering pattern. The output results of particle diameter are given in Table 5 and 6 in chapter 5. Full results are placed in the Appendix section at the end of this report.

4.1.2. Mixed Diamond Powder Ratios

The particle size results are summarized in Table 6 in chapter 5. These results were obtained from Malvern Mastersizer equipment. For fine grain feed, the D10 represents that the 10% of the total volume is smaller than 0.46 µm. For the D50, it means that 50%

of total volume comprises particle sizes with diameters smaller than 2.78 µm and 50% larger than 2.78 µm. The D90 represents that 90% of total volume is smaller than 6.95 µm. Similarly, medium and coarse grain feed may be explained.

Three sets of powders composed of 4.5 µm, 12.6 µm and 25.3 µm average diamond grain sizes were prepared and dispersed to the correct concentration and then delivered to the optical unit for measurements. A dispersed sample passed though the measurement area of the optical bench, where particles were illuminated by a laser beam.

The intensity of light scattered by the particles within the sample was accurately measured by a series of detectors over a wide range of angles. The system was then controlled by the Mastersizer 2000 software during the measurement process and the scattered data was analysed to calculate a particle size distribution.

4.2. Precomposite assembly and Synthesis of PCD compacts

PCD compact synthesis involved sintering diamond powders and this process was the most critical in the manufacture of a PCD cutter and involved a number of steps outlined in the following sections.

4.2.1. Pre-composite assembly and outgassing

Powders were weighed and placed into metal cups, then substrates were placed on top of the diamond powder and both were compacted. A second cup was placed around the WC substrate and the precomposites were outgassed in a high temperature vacuum furnace and sealed to prevent any atmospheric impurities finding their way through into the diamond powder.

4.2.2. Capsule Assembly

Units were enclosed in salt nests which acts as pressure and heat transfer medium and then loaded into a High Pressure – High Temperature (HPHT) press.

4.2.3. Sintering

Units were subjected to HPHT conditions of 1500 °C and a pressure of 5.5 GPa. Figure 38 shows the process steps involved during sintering:

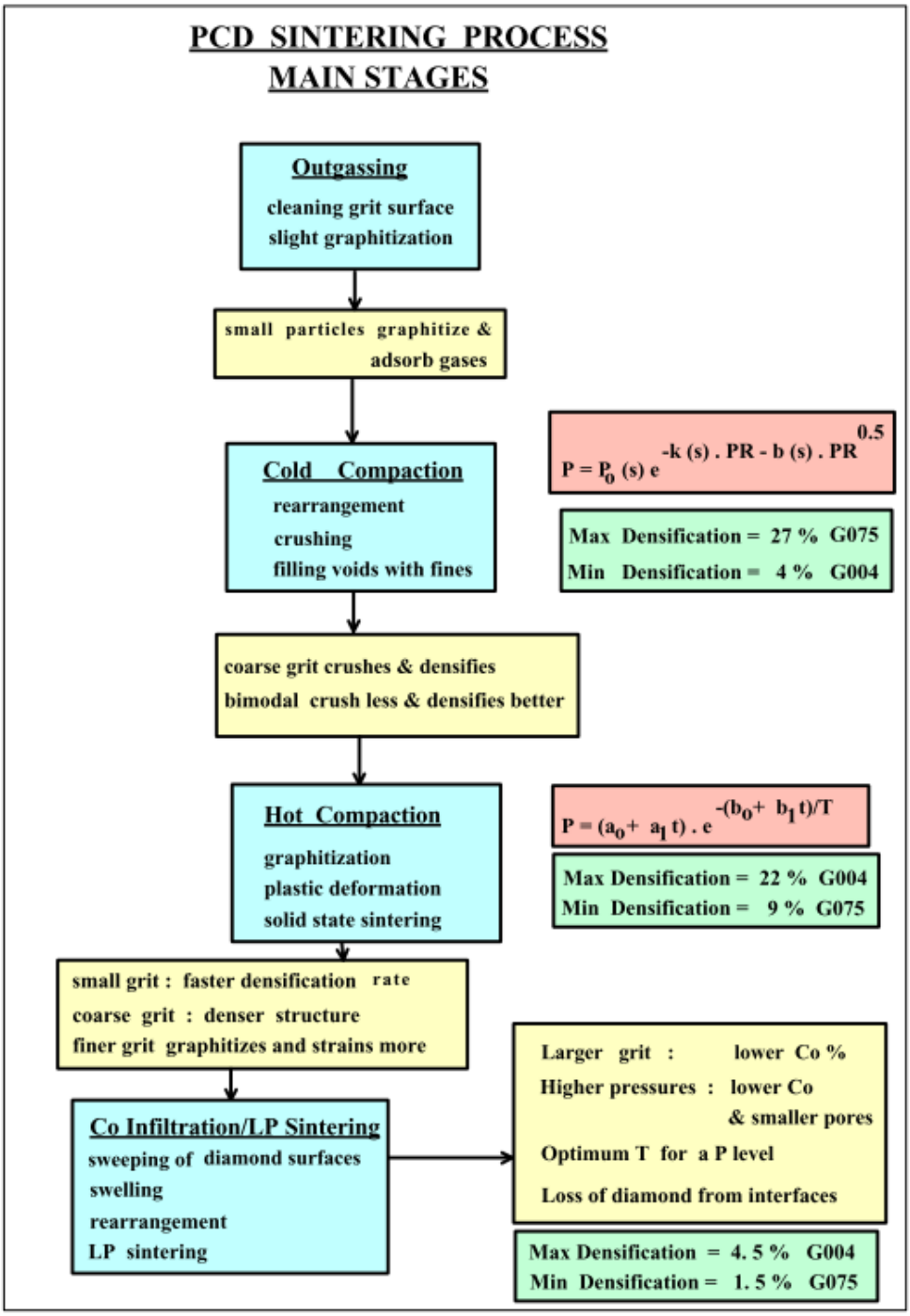


Figure 38: Process steps during sintering [47].

4.3. Sintered PCD compact processing

The resulting PCD table thickness was 2.5 mm. After sintering, cutters went through a variety of processing operations to produce a finished product. The processing steps included PCD lapping, OD grinding, carbide base grinding, PCD chamfering, WC chamfering and quality control.

4.4. Sintered PCD Characterisation

4.4.1. Sample Preparation (EDM Cutting and Polishing)

Sintered WC-PCD samples from the three variants were wire EDM cut to the right sizes, ground, lapped and polished for microstructural analysis. Furthermore, a series of samples from each of the three variants were cut 1.5 mm above the interface on the substrate to diamond area to separate the diamond table from the substrate to give meaningful magnetic properties measurements. The same disks were used to determine the density of metal phase in PCD.

4.4.2. Scanning Electron Microscopy (SEM)

ESEM (Philips XL30 at accelerating voltage of 15 keV and spot size of 3 nm as well as working distance of 12 mm) housed in the DRL was used to study the microstructure of PCD, grain sizes, and grain size distribution. It was also used to calculate volume fraction of both metallic and diamond phase. Electron Dispersive Spectroscopy (EDS) software was used to help identify the elemental composition of various phases present in the PCD microstructure using SEM images.

4.4.3. Image Analysis

Image analysis (IA) was used to characterize and quantify the microstructure of the PCD and WC-Co substrate using SEM images. The IA software aided in determining the phase percentage, diamond grain size distribution, contiguity and cobalt phase mean free path.

4.4.4. Powder X-Ray Diffraction (PXRD) analysis

Figure 39 shows the D2 phaser PXRD machine used to qualitatively determine the phases produced by the sintering of diamond powder with cobalt as the sintering aid. Before the analysis was done, WC substrate were remove from the samples and only PCD pieces were used. This machine was used to identify phases present in each of the three variants samples. It was also used to quantify the ratio of different crystalline phases formed during sintering as well as phase transformation of PCD/WC-Co cermets that was produced by infiltration of PCD with metal Cobalt after 700 °C.

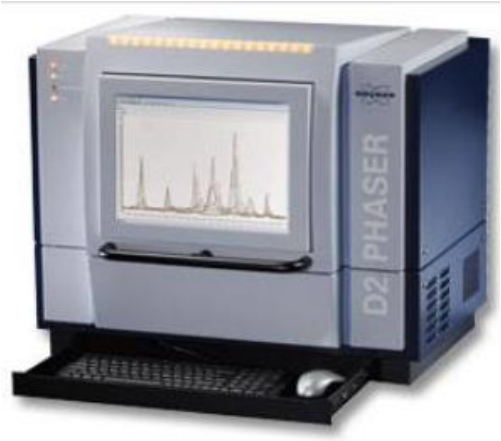


Figure 39: PXRD D2 phaser Bruker desktop [81].

Table 5: XRD parameters used to analyse the samples

Parameter	**Value**
Start 2θ position [^{0}2Th.]	30
End 2θ position [^{0}2Th.]	110
Step size [^{0}2Th.]	0.026
Cu Kα	1.5418
Generator settings	30 kV: 10 mA

The data obtained from D2 was analyzed using the PANalytical X'Pert High Score Plus software to identify peaks. Crystallite size of the magnetic particles was deduced from PXRD using Scherrer equation 15 [82] :

$$L = \frac{K\lambda}{B\cos\theta} \qquad \text{Equation 15}$$

where K is the Scherrer constant, *λ* was the wavelength of the radiation corresponding to the Cu Kα peak, *B* was the full width at half maximum (FWHM) in radians and *θ* was the Bragg angle.

The same software was also used to obtain the data needed to calculate the lattice parameters using equation 16:

$$a = d\sqrt{\boldsymbol{h^2 + k^2 + l^2}} \qquad \text{Equation 16}$$

Where: *hkl* are Miller indices of the crystal planes.

4.4.5. Magnetic Properties Facility Set-up and Measurement Method

Magnetic Saturation measurement method

Figure 40 shows the apparatus used to measure the Magnetic Saturation (Mag Sat) of the PCD samples. The apparatus includes a saturation magnet of sufficient strength to magnetize a PCD sample, a saturation module and a precision scale. The machine used for the Mag Sat measurements was the KOERZIMAT 1.097 MS measuring system with the precision scales for measuring the weight of the test piece.

The test piece was then placed in the air gap of the saturation magnet using a slide. The magnetic moment was measured by Helmholtz coils and a flux meter when the test piece was withdrawn from the magnet. The ratio of the magnetic moment to the weight was used to calculate the weight-specific saturation magnetisation (σ_s). Saturation magnet is equipped with a shielded permanent magnet with a large air gap and high field strength as well as Helmholtz measuring coils arranged within the air gap. A guide mechanism and a test piece shield for positioning the test part in the magnet were in place. The PCD samples were positioned on a sample holder within the air gap which was then magnetised to approximately saturation.

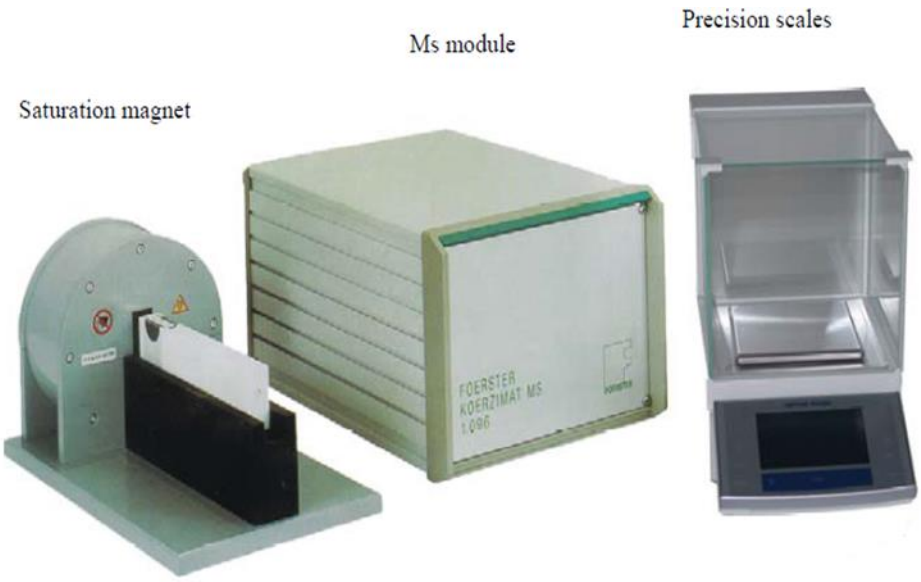


Figure 40: Magnetic Saturation Measuring Equipment Components.

Magnetic Saturation Module

The Magnetic saturation module consists of the fluxmeter, a saturation magnet that contains Helmholtz coils which have connection sockets to the fluxmeter on its rear side, there is also a PC, the remote control, and semi-automatic parts feed for interconnection to the measuring system. The module does not depend on coercivity measurements; it works independently.

Coercive Field Strength Measuring Method

The coercivity measurement set-up apparatus is shown in Figure 41. To determine the coercivity, an open magnetization circuit was required in the KOERZIMAT coil. The coil magnetized the test piece to saturation. Then FÖRSTER probes measured the polarization of the test piece and a reverse field subsequently built up until the polarization became zero. The reverse field strength H was the coercive field strength H_{cJ} in the case of zero polarization of the test part.



Figure 41: Components of coercivity Measurement equipment.

The coercive force measuring device determined the coercivity of the PCD sample. The device included a coil and measurement electronics coupled to the coil. The measurement electronics were configured to pass a current through the coil so that a magnetic field was generated. During testing, the magnetic field generated by the coil magnetized the PCD sample approximately to saturation. Then, the measurement electronics applied a current so that the magnetic field generated by the coil was increasingly reversed.

The magnetization sensor measured a magnetization of the PCD sample resulting from application of the reversed magnetic field to the PCD sample. The measurement

electronics then determined the coercivity of the PCD sample, which was the reverse magnetic field at which magnetization of the PCD sample was zero.

4.4.6. Determination of Density

Density measurements procedure

The densities of the PCD disks without the WC substrate were calculated using the Archimedes' principle. Principle, the actual weight of an object submerged in a fluid decreases by an amount equal to the weight of the volume of the liquid that it displaces.

The density can be calculated from known mass and the volume of an object. Dry masses of PCD disks were measured on a weighing scale and recorded, then samples were immersed in water and their weights were recorded.

The expression used for the determination of the density is given in equation 17.

$$\rho_s = \frac{W}{V} = \rho_w \frac{M_a}{M_a - M_w} \qquad \text{Equation 17}$$

Where: ρ_s = density of sample (g/cm^3)

ρ_w = density of water (g/cm^3)

M_a = mass of PCD in air

M_w = mass of PCD in water (g)

4.4.7. Derivation of Metal Content of PCD

Metal mass content was derived from the calculated densities in section 5.4.12 using the equation 18 [35]:

$$Co\% = \frac{(\rho_{pcd} - \rho_{diamond})}{\rho_{diamond}} \qquad \text{Equation 18}$$

Where: ρ_{pcd} = density of PCD without WC substrate

$\rho_{diamond}$ = Density of diamond

CHAPTER 5 EXPERIMENTAL RESULTS

This chapter details the experimental results of constituent diamond powder, mixed powder and sintered product characterization.

5.1. Constituents Diamond Powder Characterization

5.1.1. Particle size distribution results

The particle size distribution of the constituent diamond powder is tabulated in Table 6.

Table 6: Constituent Diamond Powder particle size distribution.

Base Name	Grain Size	D10(μm)	D50(μm)	D90(μm)	Supplier
G01		0.44	0.82	1.54	E6
G02		0.980	1.550	2.380	E6
G04		2.100	3.100	4.540	E6
G06		3.250	4.700	6.740	E6
G12		7.390	10.41	14.64	E6
G22		13.07	18.46	26.06	E6
G30		16.60	22.83	31.55	E6

Figure 42 shows the particle size distribution of constituent diamond grade analysed using Malvern.

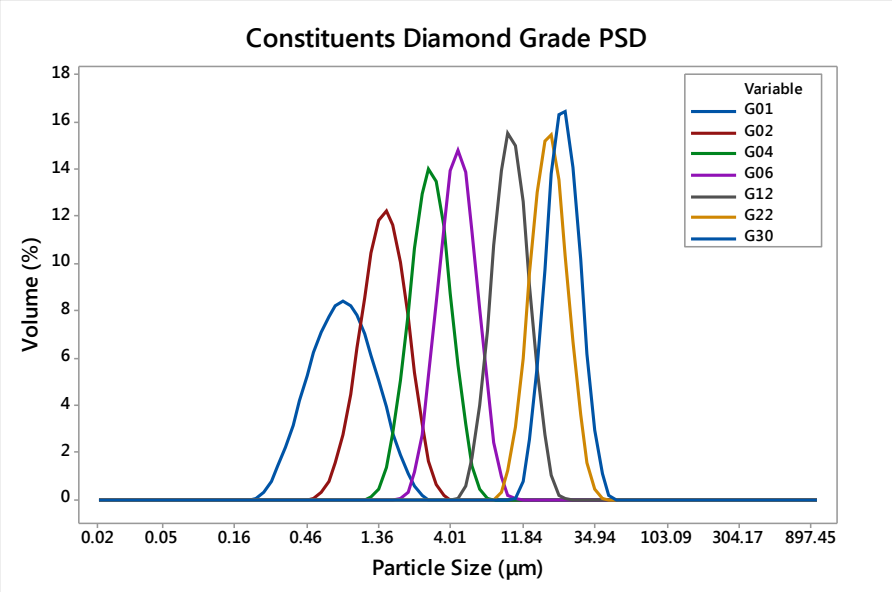


Figure 42: Constituent Diamond Grade PSD.

5.1.2. Microstructure results of constituent diamond grades

Microstructure images of each constituent diamond grade are shown in Figure 43. These images were taken at 1000x magnification to show a clear distinction between the different grain sizes.

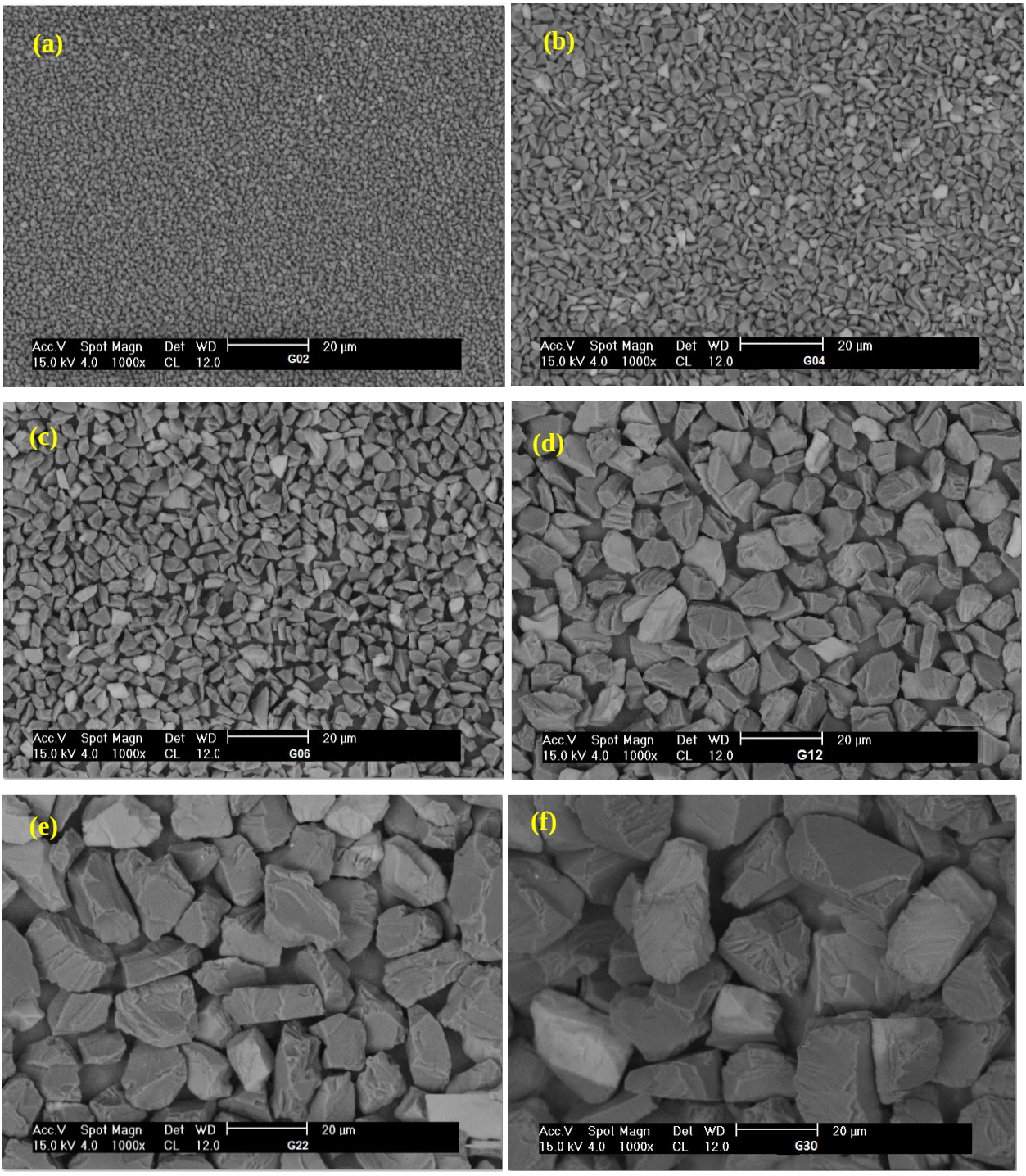


Figure 43: Micrographs of (a) G02, (b) G04, (c) G06, (d) G12, (e) G22, and (f) G30 constituent grades.

The spherical cobalt was also added into the starting diamond powders during blending and serves a multi-purpose which are explained in the discussion chapter. Figure 44 shows the particle size analysis results of cobalt. The Sp Cobalt microstructure analysis results are in Figure 45.

5.1.3. Particle size distribution and microstructure results of cobalt

The Sp cobalt is shown in Figure 44 and Figure 45 analysed by Malvern and SEM respectively.

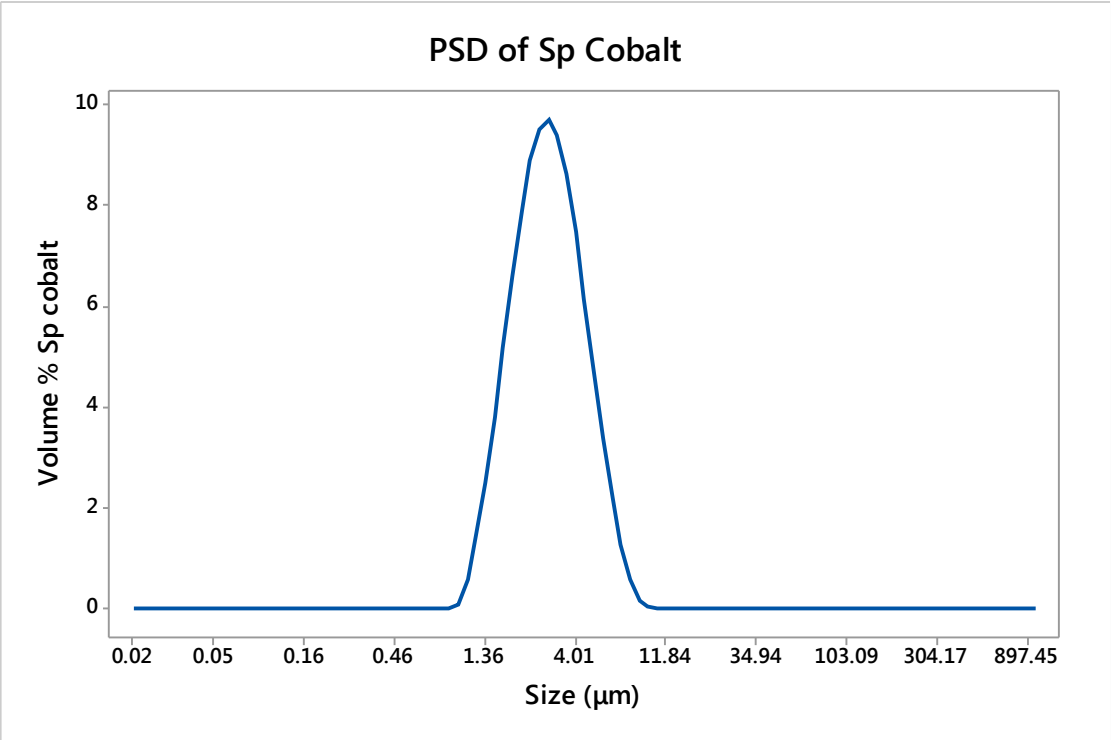


Figure 44: Particle size distribution of spherical cobalt.

Micrographs of spherical cobalt given by SEM at 5000x and 1000x respectively

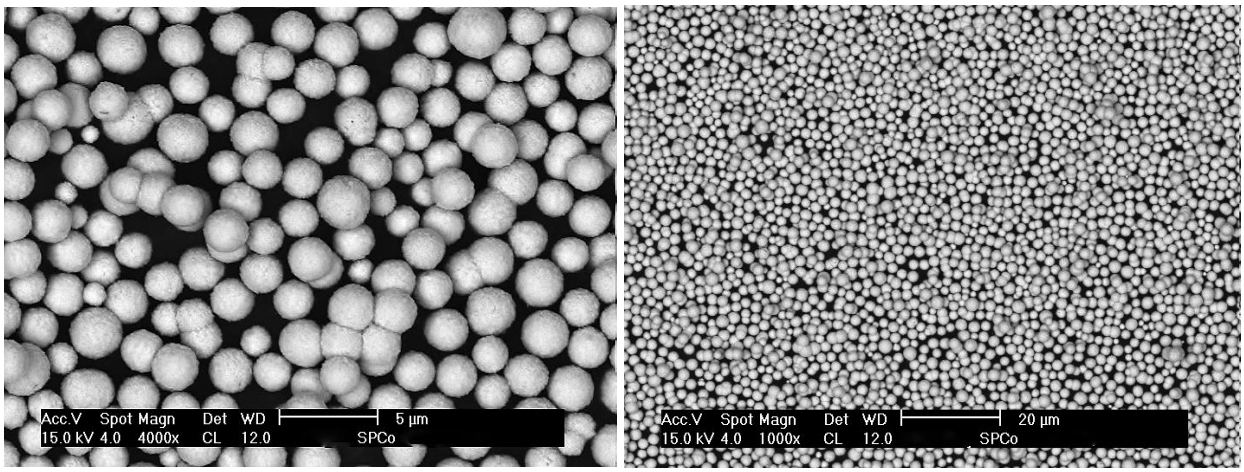


Figure 45: Micrographs of spherical cobalt.

5.2. Characterisation of mixed diamond powders

5.2.1. Particle size distribution of diamond mixes are shown in Table 7. These results were analysed by Malvern measuring instrument.

Table 7: Diamond Powder Particle sizes Composition.

Base Name	Particle Size(µm)	D10(µm)	D50(µm)	D90(µm)
Fine Grade	4.5	0.46	2.78	6.95
Medium Grade	13.6	1.94	9.52	19.91
Coarse Grade	25.3	9.27	19.93	34.62

The particle size distribution chart showing volume percentage of three diamond mix particle sizes is given in Figure 46. This shows the distribution of particle size of each mix.

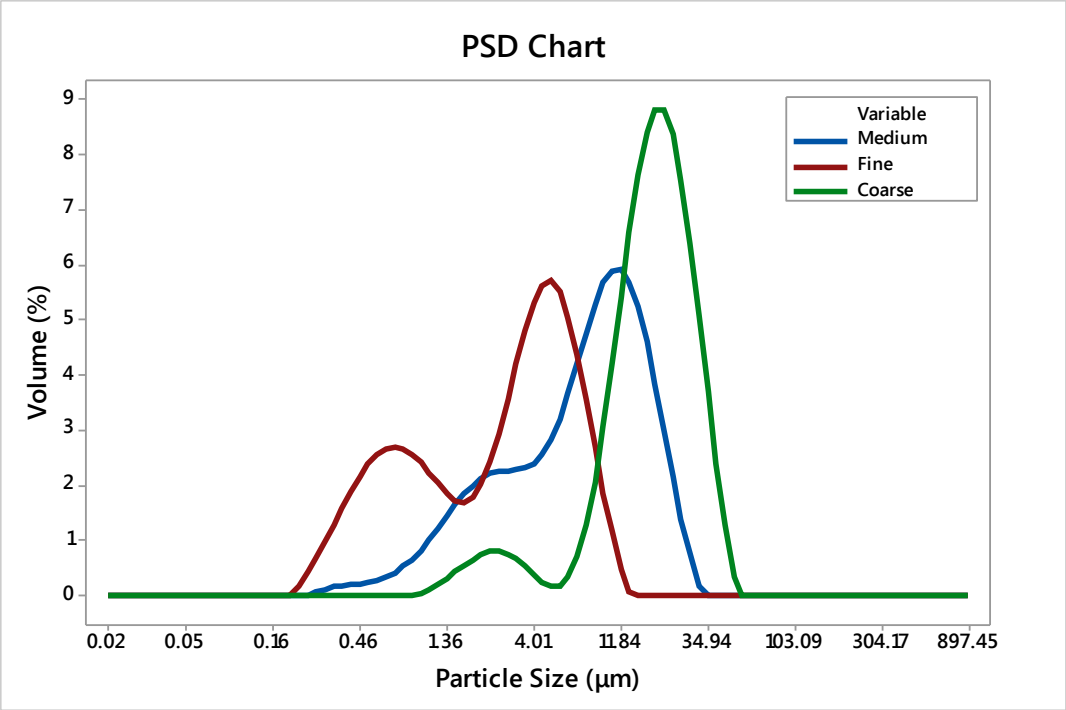


Figure 46: PSD of 3 different mixed diamond powders.

5.2.2. Microstructures of Fine, Medium, and Coarse grain powders. The images were taken at 1000x and 2000x magnification respectively for each diamond grade.

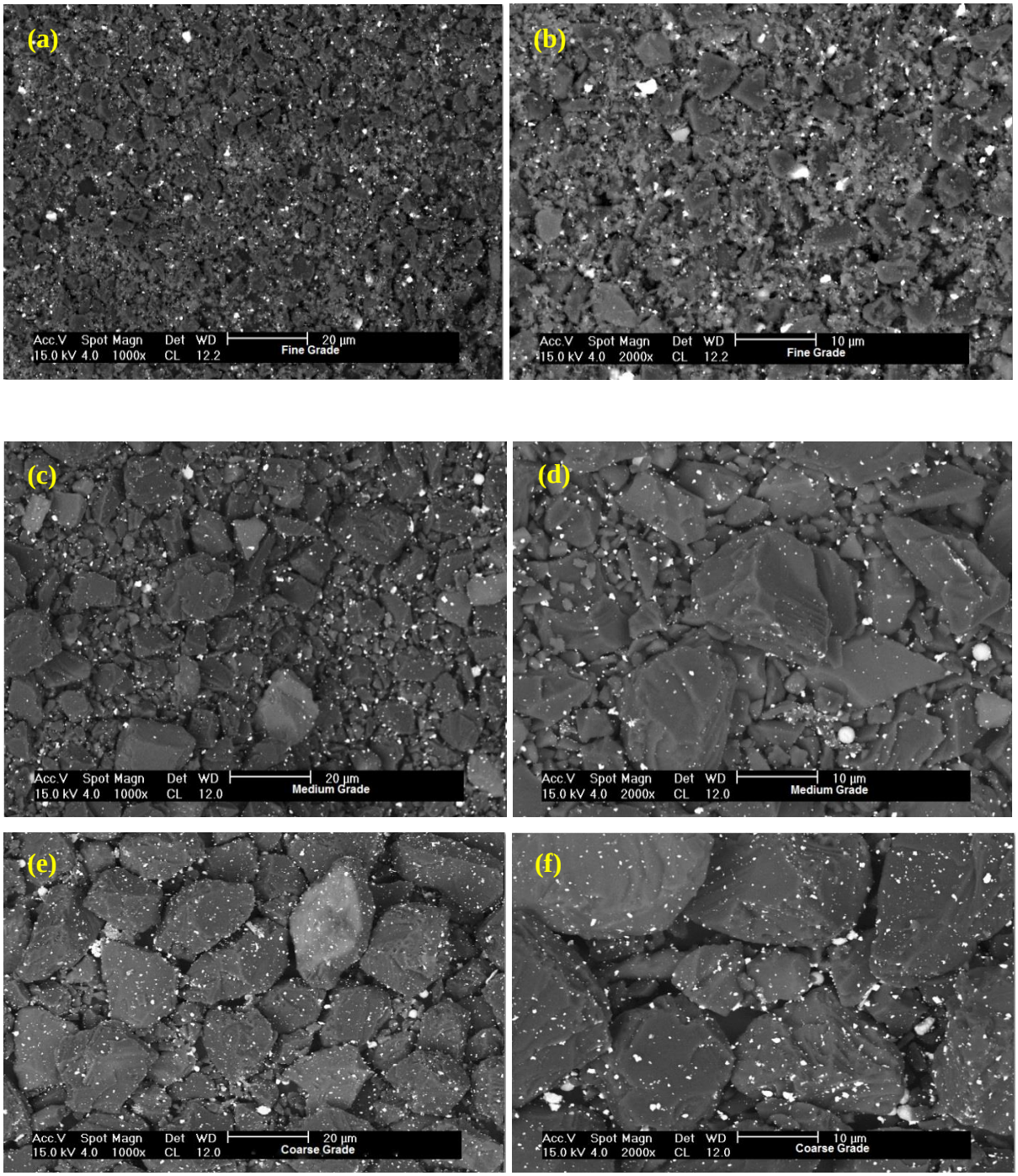


Figure 47: Micrographs of fine ((a) and (b)), medium ((c) and (d)) and coarse ((e) and (f)) diamond powders. These micrographs were captured at 1000x and 2000x magnification respectively for each size.

From the microstructure images in Figure 47, it can be seen that there exists white particles dispersed everywhere in the microstructure and these are explained as follows:

during powder mixing at the diamond mixing plant, WC balls were added into the diamond powder. These balls were found to serve a multi-purpose; (i) to adequately mix the diamond and break up any agglomeration or clumping which may form and (ii) to restrict plume formation due to giving multiple precipitation points to the WC.

5.3. Resultant product after sintering

Sintering at HPHT resulted in production of fully sintered PCD compact shown in Figure 48.

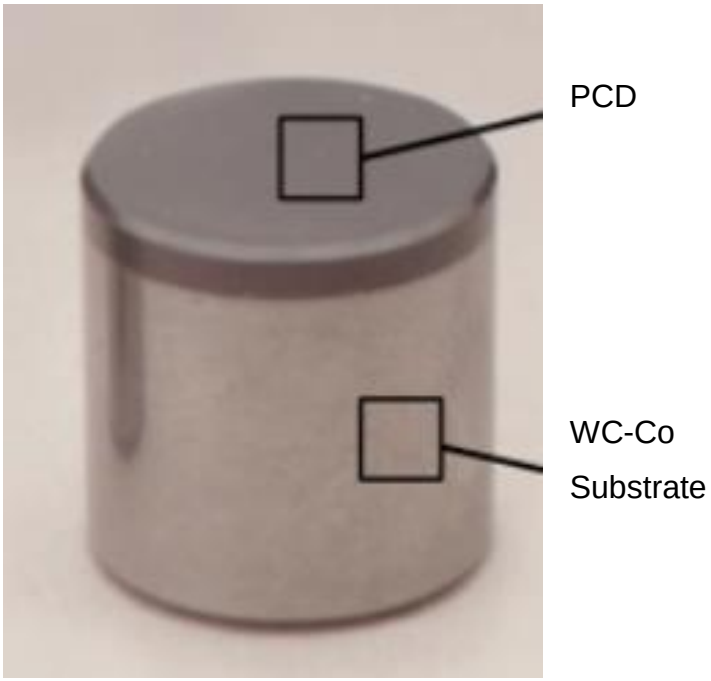


Figure 48: Sintered PCD compact.

5.4. Characterisation of sintered PCD compacts

5.4.1. Micrographs of sintered PCD compacts

The microstructure images of each of the sintered PCD compacts are presented in this section and represent the surface morphology of the entire PCD after sintering. Microstructure images were taken on the bulk of the PCD and interface of the cutter that represented the bulk microstructure and also the interface between PCD and WC substrate. These images were captured at 1000x magnification and have a scale bar of 10µm. However, the images cannot be included in this dissertation due to IP constraints.

5.4.2. Image Analysis Results

The IA software revealed the contents of each variant such as the average grain size, average cobalt pool size, cobalt mean free path and diamond contiguity as shown in Table 8.

Table 8: Image Analysis results of PCD

Material	Fine Grain	Medium Grain	Coarse Grain
Ave. Diamond grain size (µm)	3.25	8.71	11.84
Ave. Cobalt pool size (µm)	1.30	1.91	2.79
Ave. Diamond Area (%)	89.61	90.82	91.54
Ave. Cobalt Area (Wt%)	22.67	20.35	18.94
Ave. Cobalt MFP (µm)	0.34	0.62	0.80
Ave. Diamond contiguity (%)	63.82	62.27	66.55
WC phase area (%)	0.34	0.37	0.37

The cobalt content results from IA were converted to wt% to be able to compare them with the ICP and Archimedes density methods. There will not be a direct correlation between ICP and IA, as there is tungsten dissolved in the cobalt seen by the SEM, therefore, it would be more accurate to describe the SEM IA cobalt % as binder %.

5.4.3. X-Ray Diffraction Results of sintered PCD disks

X-Ray diffraction was used to determine the phases present in the material. In the case of polycrystalline diamond composites, a typical x-ray diffractometer trace as shown in Figure 49 indicates the presence of diamond and cobalt as discrete phases in the sintered diamond layer. Any other phase present generated their own unique diffraction peaks. Phase composition results were obtained from the diffractometer. The type of X-ray radiation used is Cu Kα. Specimens of three different diamond grades were analysed on D2 Phaser XRD apparatus.

All the selected diamond grades produced spectra that were very similar. Measurements were done on sintered PCD disks without the tungsten carbide substrate. Figure 50 shows XRD spectrum obtained for fine, medium and coarse grain PCD respectively. These patterns were obtained with 2θ values ranging from 30 ° to 110 °. This range of 2θ

angles was chosen because the corresponding XRD peaks for PCD and both phases of Co are found in that range.

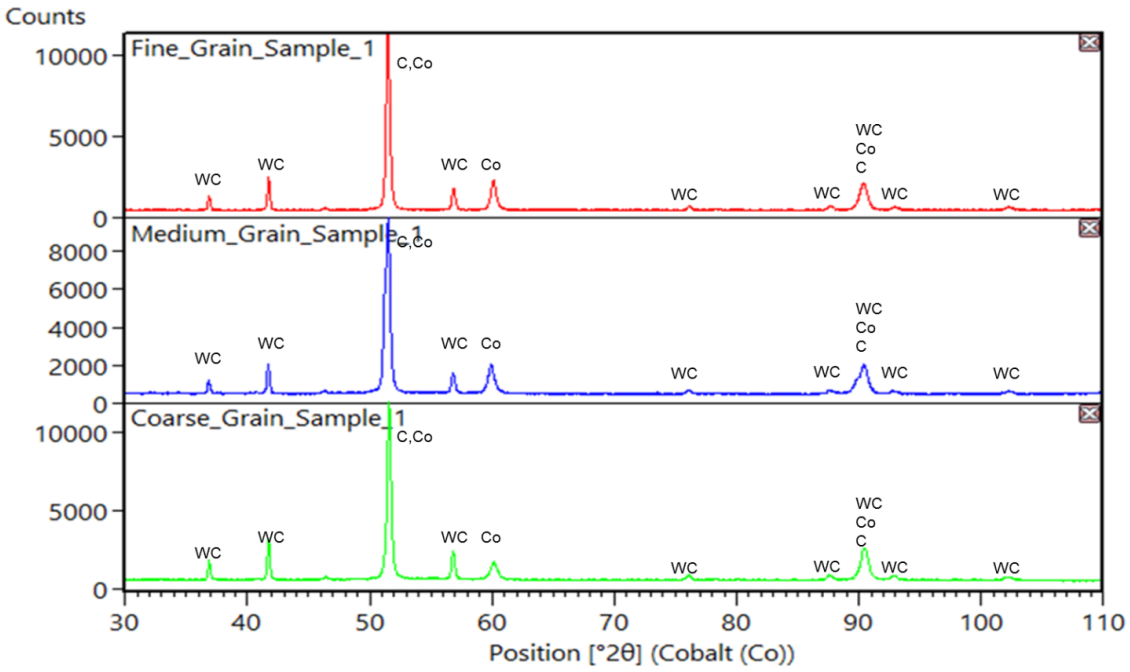


Figure 49: XRD spectra of fine, medium, and coarse grain diamond tables.

5.4.4. Cobalt and tungsten content analysis measured by ICP

This section details the chemical composition of the different diamond grain size PCD tables studied in this work (without their WC substrates) using the ICP technique. The amounts of Co and W contained in the three types of PCD studied here are given in Table 9 and 10, as well as Figures 50 and 51 respectively.

5.4.5. Metal phase content

Table 9: Cobalt phase content as a function of grain size

Content	Part ID	Fine Grain %	Medium Grain %	Coarse Grain %
	1	16.239	16.061	14.230
	2	16.169	15.417	13.965
Metal phase	3	15.840	15.245	14.044
Content	4	15.971	15.570	13.643
Average		16.055	15.573	14.080
Std Dev		0.183	0.351	0.136

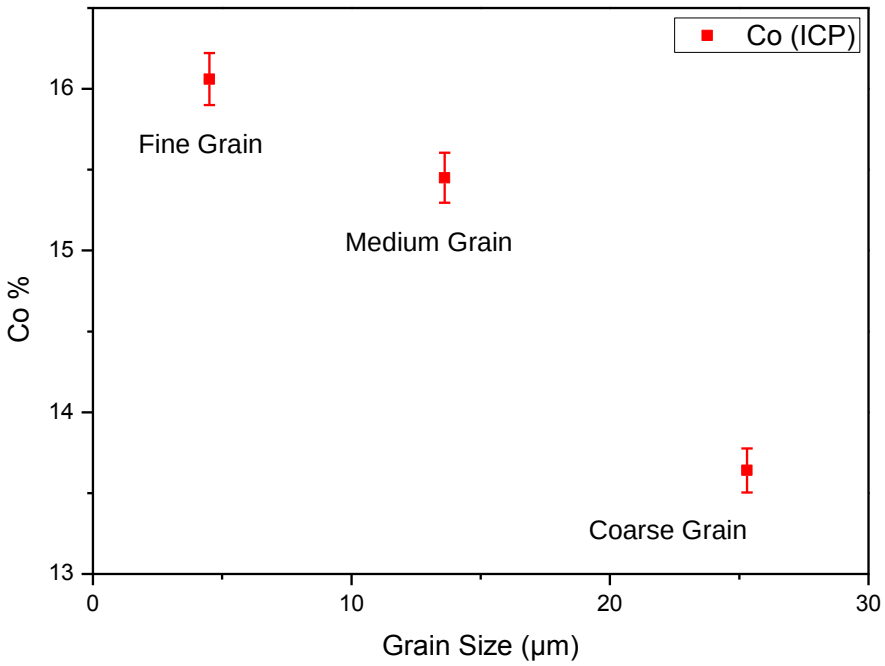


Figure 50: Cobalt content given by ICP in Wt% versus diamond grain size.

5.4.6. Dissolved Tungsten content

Table 10: Tungsten phase content as a function of grain size

Content	Part ID	Fine Grade	Medium Grade	Coarse Grade
Tungsten (%)	1	4.291	4.221	4.332
	2	4.165	4.280	4.179
	3	4.338	4.348	4.305
	4	4.301	4.159	4.292
Average		**4.274**	**4.252**	**4.277**
Std Dev		**0.075**	**0.081**	**0.067**

5.4.7. Graphical representation of grain size and tungsten.

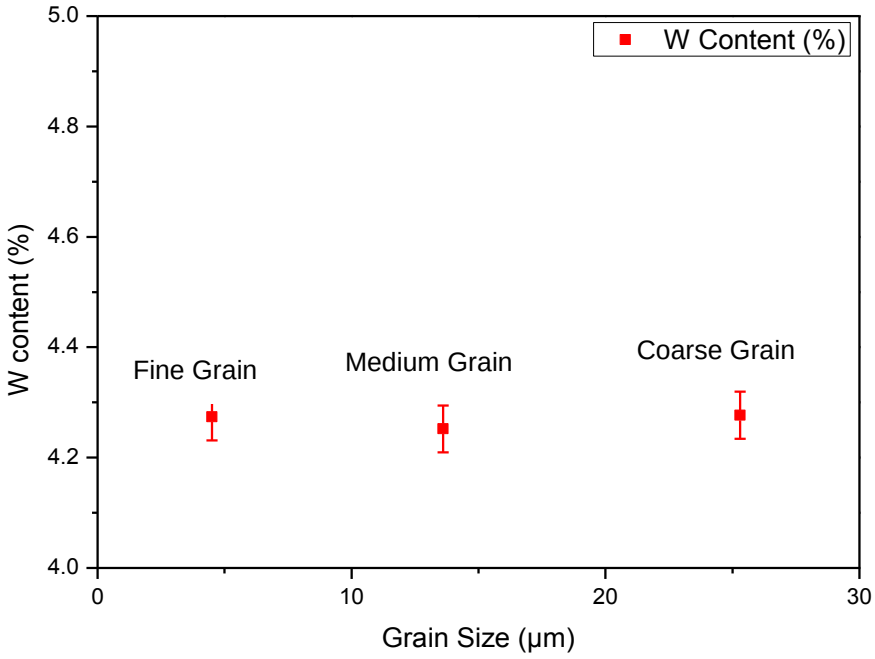


Figure 51: Dissolved Tungsten content in PCD of each variant given by ICP in wt%.

5.4.8. Magnetic Properties results

The magnetic properties results are summarized in Table 11. Scatter plots showing the results follow in section 5.3.10 and 5.3.11

Table 11: Summary of magnetic properties of each variant

Product Name	**Sample ID**	**Mass (g)**	**Mag Sat** (%)	**Coercivity (KA/m)**
Fine Grain	1	0.727	16.22	13.08
	2	0.782	14.75	14.64
	3	0.765	15.64	15.03
	4	0.720	15.65	13.38
Medium Grain	1	0.863	13.76	9.72
	2	0.860	13.92	9.76
	3	0.866	13.82	9.66
	4	0.865	14.03	9.58
Coarse Grain	1	0.721	11.66	9.28
	2	0.683	11.93	9.05
	3	0.722	12.13	9.07
	4	0.768	11.73	9.07

5.4.9. Saturation Magnetization

The saturation magnetization results are presented in Figure 52.

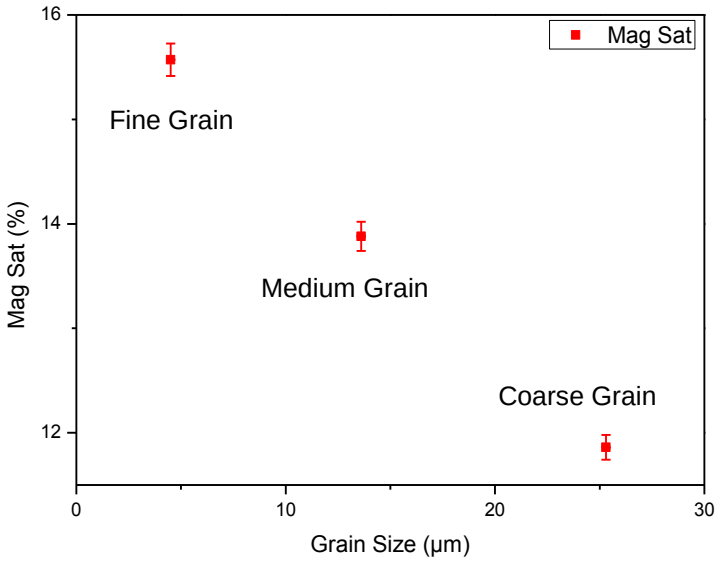


Figure 52: Saturation magnet versus grain size of each variant.

5.4.10. Coercive Field Strength

Figure 53 shows the relationship between grain size and coercive force. Coercive force decreases when grain size increases. This correlate well with the cobalt content determined for each of the three diamond grain size.

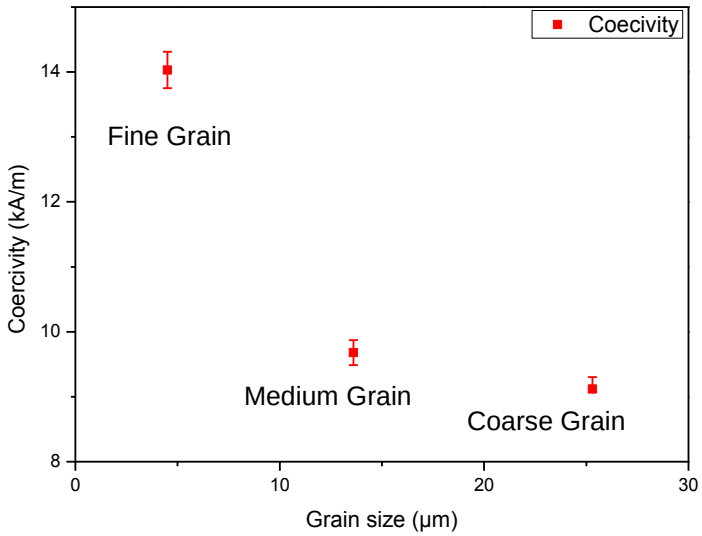


Figure 53: Coercivity results versus grain size of each variant.

5.4.11. Density Measurements Results

Metal phase content was derived from the densities measured using Archimedes' immersion density principle. This section shows the metal phase present based on the measured density of the samples the density determination and therefore derivation of metal phase content.

Table 12: Density measurements results

Feed	Sample ID	Mass(dry)(g)	Mass (Wet)(g)	Density (g/cm^{-3})	Co Content (%)
Fine Grain	1	0.491	0.371	4.0917	16.24
	2	0.466	0.352	4.0877	16.13
	3	0.619	0.468	4.0993	16.46
	4	0.504	0.381	4.0976	16.41
Average		**0.520**	**0.393**	**4.094**	**16.31**
Std Dev		**0.068**	**0.051**	**0.005**	**0.152**
Medium Grain	1	0.478	0.361	4.0855	16.06
	2	0.646	0.487	4.0629	15.52
	3	0.430	0.324	4.0566	15.24
	4	0.598	0.451	4.0680	15.57
Average		**0.538**	**0.406**	**4.068**	**15.60**
Std Dev		**0.101**	**0.076**	**0.012**	**0.341**
Coarse Grain	1	0.957	0.719	4.0210	14.23
	2	0.706	0.530	4.0114	13.96
	3	0.622	0.467	4.0129	14.00
	4	0.732	0.549	4.0000	13.64
Average		**0.754**	**0.566**	**4.011**	**13.96**
Std Dev		**0.143**	**0.108**	**0.009**	**0.243**

Figure 54 shows the amount of cobalt derived for each diamond grain size. These results were correlated with the results found by ICP and discussed in section 6.1.3

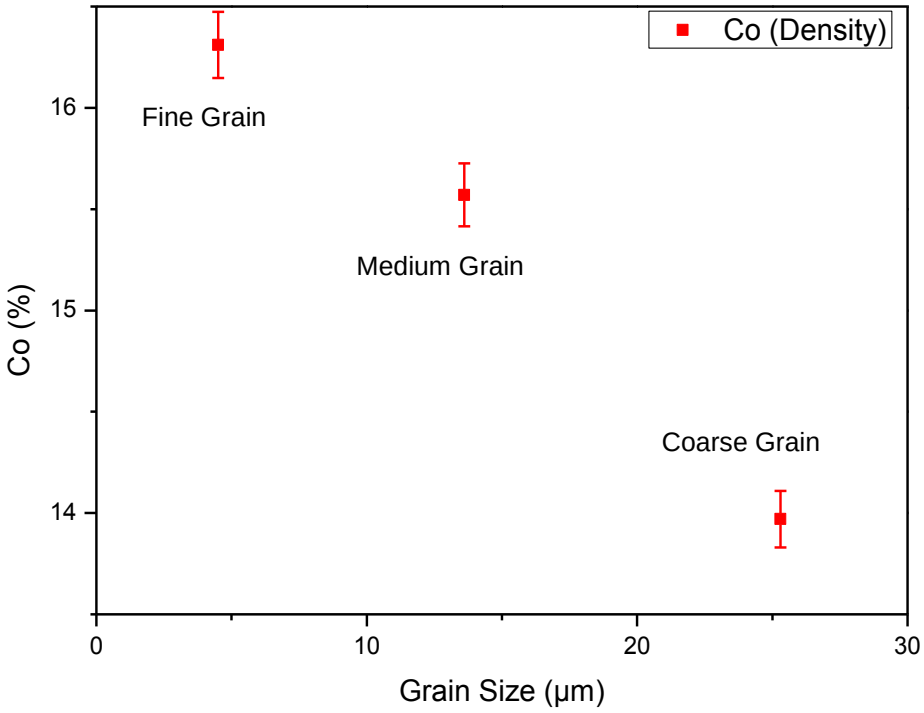


Figure 54: Grain size versus Co content from derived densities. This includes the effect of heavy WC in the PCD table as were clearly shown by XRD analysis.

CHAPTER 6 DISCUSSION OF RESULTS

6.1. Introduction

This section discusses the results obtained with an emphasis on the relations between them and the starting diamond powders particle sizes. Variability in diamond grain size has a strong impact on the structure and properties of the resulting material in many ways. The cobalt content achieved through Archimedes' immersion density principle demonstrated a strong correlation to the starting PSD compared to the same quantity as measured through ICP. The chapter also includes the correlation of results obtained from different techniques that showed to be very positive. In this chapter, the information obtained and discussed from previous chapters will be integrated into one model linking sintering, processing and microstructure to the magnetic properties of the material.

This chapter is divided into three sections, namely:

- Diamond grade selection and Co function
- Sintered PCD compacts characterization
- Model of results obtained

6.2. Characterization of diamond powders

6.2.1. Diamond charge mixes and grade selection

Each of the three types of diamond feed were prepared by mixing and milling different grades of diamond powders altogether. PSD plots are given in 5.1. Mixing of these grades resulted in a good degree of powder packing as the voids were minimized between diamond crystals. This in turn promoted an excellent sintering process at HPHT and produced a PCD that had superior toughness [83].

The selected mixes thus played a role in increasing the diamond packing density, which then increased the wear resistance of PCD at controlled sintering conditions. These mixes assisted in the fully sintered PCD and then resulted in a higher degree of contiguity between diamond grains. This in turn increased the PCD chipping resistance. Filling the voids between the coarse diamond grains with finer grains influenced densification and

yielded a continuous cutting edge as opposed to the rough irregular cutting edge of coarser diamond grains only.

The microstructure images (in section 5.1.) of mixes show the different sizes of diamond grade that were mixed together rather than a particular size. For each of the three diamond grade sizes, different amounts (4% (fine grain), 2% (Medium grain), and 1% (Coarse grain) respectively) of cobalt were added during powder mixing which served the purpose of creating channels for the infiltrated cobalt from the substrate and also helped with rearranging diamond particles during compaction to allow easy diamond-diamond bonding.

The amounts of added cobalt were varied depending on the grade size of diamond used. The fine grain diamond powder has closely packed particle sizes which prevent the infiltrated cobalt from substrate to enter the PCD easily, therefore, a higher percentage of cobalt was added to disperse the diamond particles evenly and to create path ways for the infiltrated cobalt. This in turn reduced the amount of time taken to fully sinter the PCD in which case it would have taken more time to sinter without cobalt added in the starting diamond grades during blending.

During diamond powder blending, WC balls were mixed with powders during milling which served the purpose of breaking the agglomeration of fines formed during mixing. This helped increase the abrasion resistance which the PDC could suffer resulting from the agglomerated area [83]. The admixing of WC balls also played a major role in preventing the formation of plumes during sintering which in turn reduces the life of the cutter. A plume in this case is a WC-Co phase that enters the diamond table during sintering which is detrimental to the life of a cutter. It forms as a result of hotter pressing conditions than normal in which case WC starts to melt from the substrate or could also result from the mixing procedure.

6.2.2. Characterization of sintered PCD

The characterization of sintered PCD has been subdivided into a number of sections. The PCD compact has three interfaces, namely: (i) PCD layer which is used as the cutting element, (ii) the WC-Co layer which is the carbide substrate and is used to attach the cutter to a drill bit by brazing, and lastly (iii) the interface between PCD layer and the

cemented WC-Co substrate which provides strength so that the cutting element can withstand shear loads and residual stresses produced during HPHT sintering process. The focus of this research is on PCD layer and the interface between the PCD layer and the cemented carbide substrate.

The interface design reduces the residual stresses arising from both the substrate and the PCD layer as a result of the high pressure and high temperature sintering process. Moreover, as in Figure 55, the interface is rich in cobalt. At the same time, the high thermobaric parameters cause considerable residual stresses in a finished product because of differences in bulk modulus and thermal expansion coefficients between PCD and carbide.

The residual stresses are generated during the cooling stage when the PCD layer is already fully sintered. The carbide shrinks more than the top PCD layer due to the thermal expansion coefficients mismatch between the PCD layer and substrate, forcing it to bend outward.

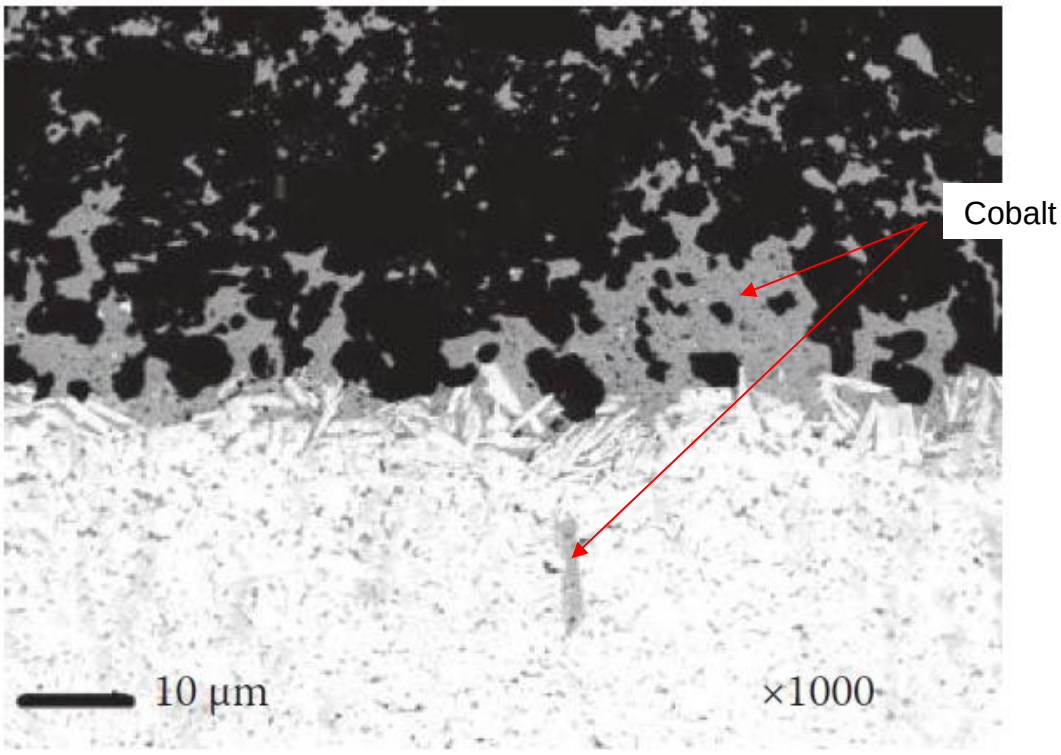


Figure 55: Micrograph of fully sintered PCD compact [10].

As Figure 55 shows, Co is well distributed over the PCD layer. It is present at the bottom, near to the WC substrate, as well at the top of the PCD. The Co is located around the

diamond grains in microstructures. The microstructure is also rich in Co pools which have been preferentially infiltrated because of superior transport channels with the help of added SP cobalt during the mixing stage.

For the analysis of the structure of the produced samples using the SEM and XRD, the results showed a formation of a thin transition zone between the carbide substrate and the diamond layer that contains 8%–12% cobalt during sintering which is also known as the denuded zone. The thickness of the denuded zone approximately corresponds to the initial diamond powder's particle size, that is, the cobalt melt penetrates into the diamond layer to a depth of no more than 40 μm.

During PCD sintering, as the infiltrated cobalt reached its melting point, it dissolved W and C in solution from the substrate. Not all of the C was dissolved into solution though, only a portion of it was converted into diamond as the temperature was increased. When the process of sintering reached equilibrium, the excess W and C were precipitated out of the solution and formed the WC phase which is observed in the XRD spectrum of fully sintered PCD compact shown in Figure 56. Such WC phases do not show strong peaks as they are present in very small amounts in PCD. One aspect of Co infiltration as opposed to sintering admixed powders is that as Co infiltrates, it cleans the diamond particle surfaces of their surface adsorbed gases and other contaminants thus acting as a cleaning agent as well as a liquid phase.

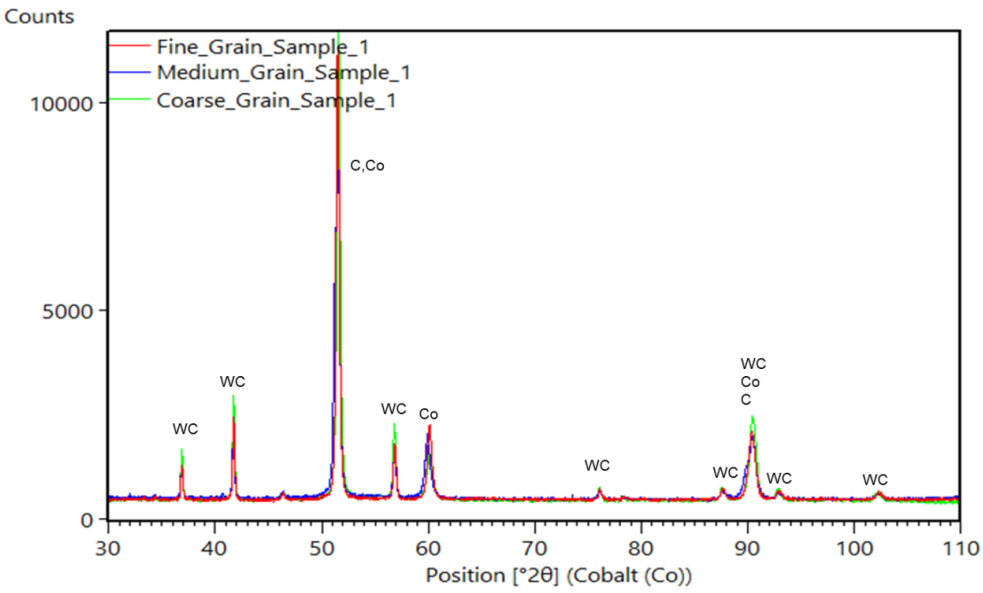


Figure 56: XRD Spectrum of all three diamond powders.

It is apparent that PCD is a very inhomogeneous material in terms of interaction with the primary electron beam in an SEM, the diamond has a significantly weaker effect on the electrons than the much higher atomic number cobalt and tungsten carbide phases present. As such the consideration of the effect of the beam on binder/diamond geometries close to the sample surface show marked effects of this inhomogeneity on the generation of backscattered electrons. This variation in backscattered signal can be minimised by minimising the incident energy, the absorption of which by the sample causes the distinctive interaction volume from which the signal is generated.

Minimising the size of the interaction volume by limiting the incident energy will effectively minimise the mixing of phases in the interaction volume and thus the deterioration of the image for subsequent image analysis based techniques. In the case of diamond the interaction volume is also larger in scale at 15kv than the submicron scale fine cobalt structures dispersed between the diamond grains in PCD.

Effect of tungsten in PCD

Tungsten is present in PCD in two ways: (i) It is added in the diamond powder at the very early stage of powder preparation to serve the purpose of preventing formation of plumes. (ii) When cobalt is infiltrated from WC substrate into PCD during sintering, it carries WC grains with during synthesis, which are then precipitated out during cooling after sintering to form WC. The presence of excess W in PCD causes early fracture of the diamond cutter. This yields inferior performance of the cutter. Tungsten also plays a role as leaching inhibitor in which it prevents acid to penetrate deeper into the PCD.

Relationship between grain size of diamond and various parameters.

6.2.3. Grain Size vs Magnetic saturation

The findings of this study showed that the magnetic properties of the cobalt phase in PCD are significantly affected by varying the particle size of the starting diamond. It is clear that as the particle size increases, there is a reduction in magnetic saturation as shown in Figure 57 due to the reduced amount of Co phase in the PCD affected by the staring diamond grain sizes. The decreasing trend appears to be limited to 40µm which was

found to be in agreement with Meiss and Rai [35]. This in turn will show no further reduction in magnetic saturation.

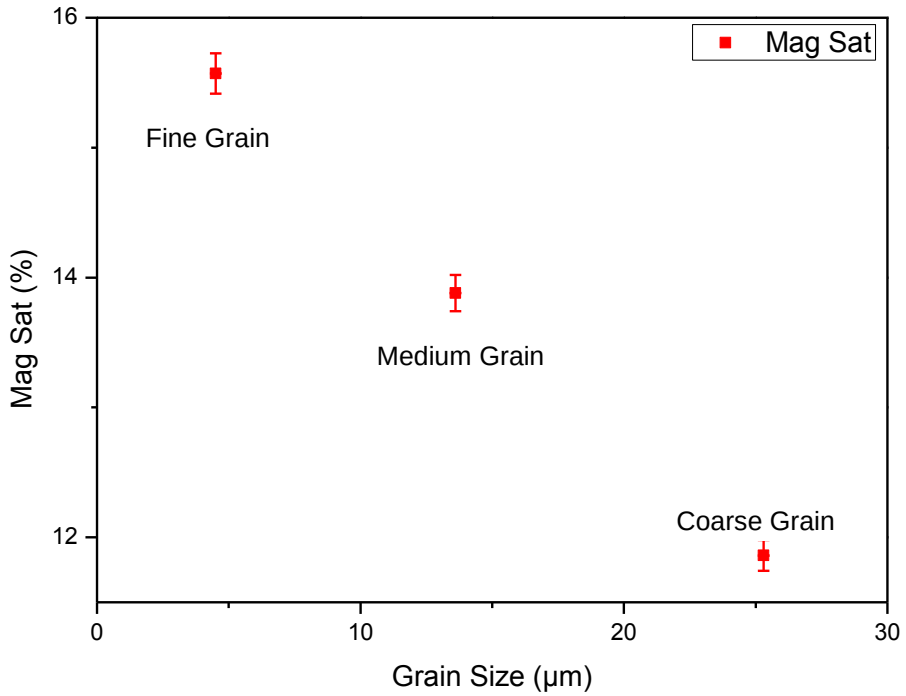


Figure 57: Relationship between magnetic saturation and diamond grain size after sintering.

The findings further showed that since PCD composites were found to comprise 5–20 wt% cobalt as a metallic phase in PCD which is ferromagnetic, the cobalt metal phase contained both tungsten and carbon in solution which moved into the PCD during infiltration of the cobalt during sintering. The amount of W that has dissolved in the Co phase was evaluated by measuring the magnetic saturation of the PCD which showed the linear decrease in the saturation value of the cobalt resulting from addition of the W, but the amount of carbon in solution did not affect it. At the saturation point, all magnetic moments are in parallel with the external fields and therefore are not affected by the sample size. This simply means if a sample is cut in half and the saturation magnetisation is measured, the results will still be the same as those found with the full sample.

6.2.4. Relationship between grain size and coercivity

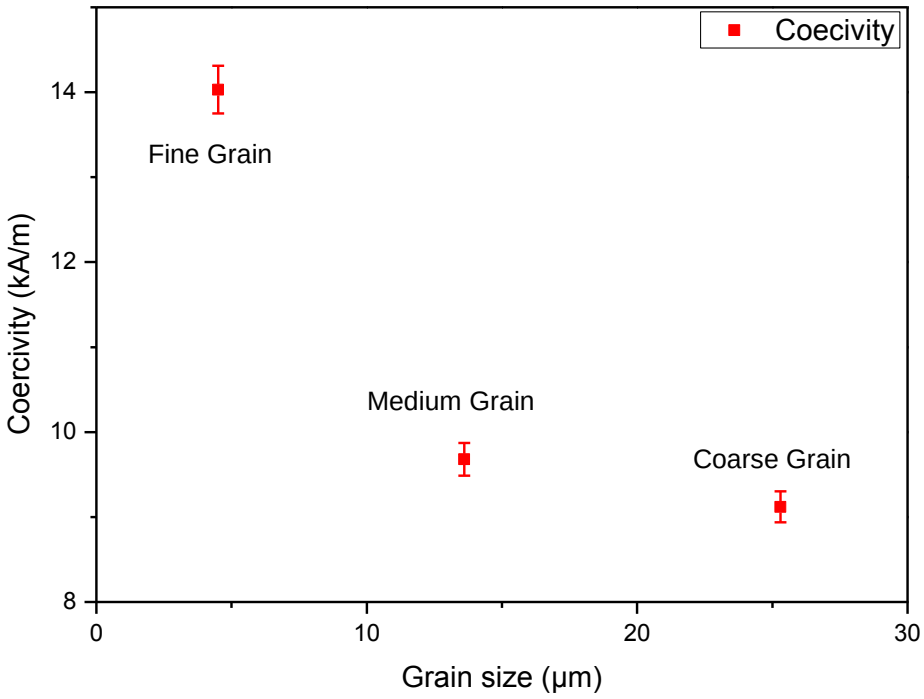


Figure 58: Relationship between coercivity and diamond grain size after sintering.

In a similar manner, the findings show that an increase in particle size reduces the coercivity as shown in Figure 58. The reduction in coercivity is a result of the presence of WC in PCD which precipitated out after sintering. The coercivity was also affected by the presence of additives in the starting diamond powder. The rate of decrease is insignificant beyond 40μm particle size PCD layers as reported by Meiss and Rai [35].

6.2.5. Correlation between grain size and Cobalt content

Cobalt content calculated (ICP), IA and that derived from Archimedes' principle were plotted on the same graph to compare the relationship between them. The results show that the finer grain PCD consists of larger cobalt content in the microstructure resulting from the larger surface areas in the PCD table which accommodated a large amount of the cobalt phase during LPS. Figure 59 shows a decreasing trend in which the cobalt content decreases at the expense of increasing diamond grain size.

Since IA cobalt content is given in vol%, then the IA cobalt results were converted from vol% to the wt% to have consistent results comparison. The IA cobalt content results were

very interesting in comparison to the other 2 methods in the sense that image analysis results overestimated the wet chemical results by about 30% due to the fact that the depth from which information was obtained is larger than the grain size of the material being analyzed, resulting in higher cobalt contents, larger cobalt mean free paths and lower diamond contiguity than expected.

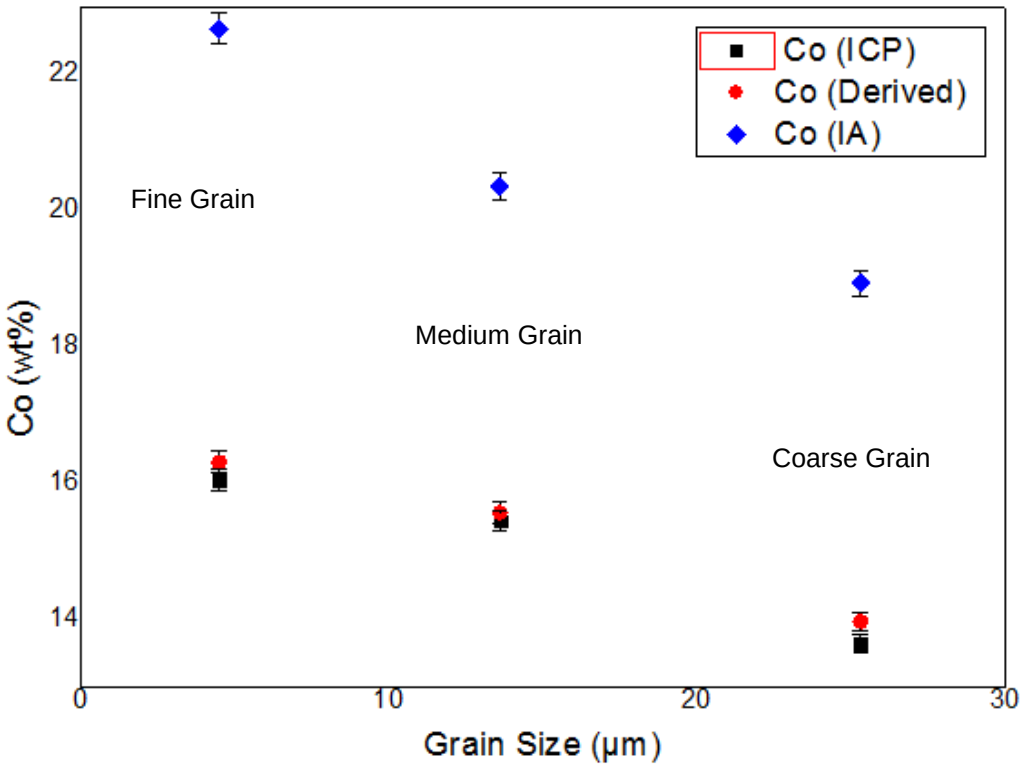


Figure 59: Relationship between ICP, IA and derived cobalt content and diamond grain size after sintering. The derived value was calculated using Archimedes immersion density values.

6.2.6. Comparison of metal phase MFP and coercivity

Figure 60 shows the coercivity of the PCD tested in this work as a function of the cobalt mean free path between neighbouring diamond grains. The coercivity shows a decreasing function of the metal phase's mean free path. The reason for this is that a large mean free path signifies larger contiguous areas of the metal phase of PCD. This in turn indicates a bigger freedom of movement for the magnetic domain walls described in section 2.10. This relationship is in agreement with literature, as it is reported in the case of WC-Co hard metal [56].

It is deduced from the graph that a large coercivity indicates a smaller mean free path. A smaller mean free path indicates relatively more diamond-to-diamond bonding in well-sintered PCD and a large surface area. In general, as the sintering pressure that is used to form the PCD table increases, the coercivity increases and the magnetic saturation decreases.

The presence of inclusions in the cobalt phase, such as WC, or a small size of the cobalt pools residing between diamond grains acts as a barrier movement in PCD. This obstruction in wall movement delays the alignment of the magnetic moments in the metal phase with the applied magnetic field. This in turn translates in the high coercive force exhibited by such a material.

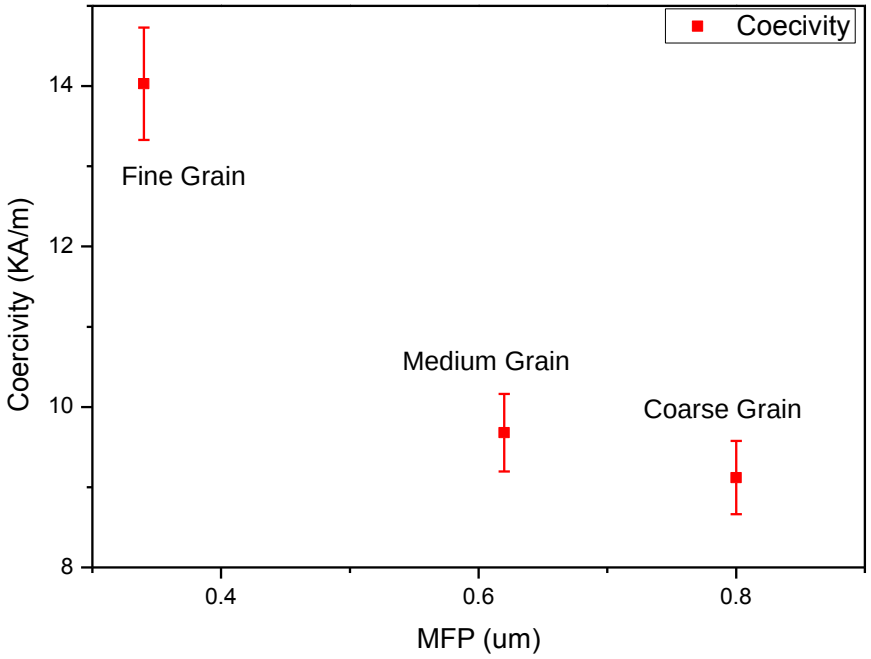


Figure 60: Correlation of coercivity and Co mean free path (MFP) (µm).

6.2.7. Comparison of MFP and Grain Size of PCD

Figure 61 shows that the smaller the grain size of the starting diamond the smaller the MFP. This indicates that the PCD compact has larger magnetic saturation than the amount of cobalt which is ferromagnetic and therefore higher. This is evident for a fine grain cutter because it suffers microchipping due to the larger amount of cobalt in the PCD structure. However, the structure-to-property relationships in PCD is somewhat

complex due to the thermal expansion mismatch between residual cobalt and the intergrown diamond skeleton.

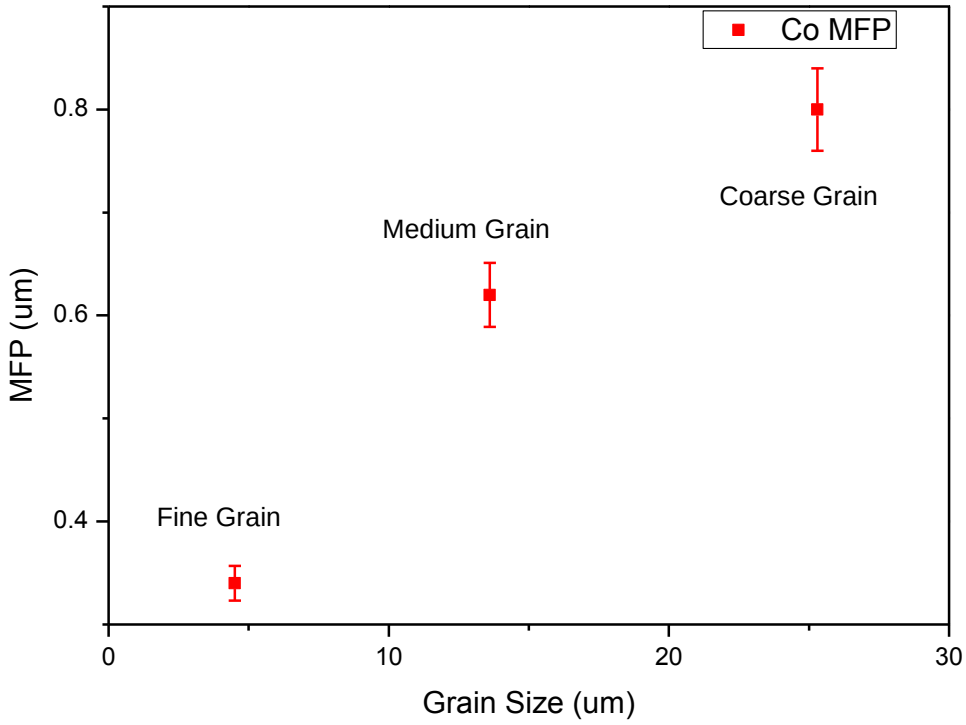


Figure 61: Relationship between MFP and diamond grain size.

6.2.8. MFP versus Co (IA)

It has been universally found that the fracture toughness increases with volume fraction, the mean free path (MFP) length of the metal phase, and the size of diamond grains as reported by Meiss and Rai [35] for the case of diamond grains. In addition, higher fracture toughness has been assumed to result from the increased contiguity of Co phase, which minimizes the fracture along weak diamond-diamond boundaries. Figure 62 shows the correltion between the MFP and cobalt calculated by ICP.

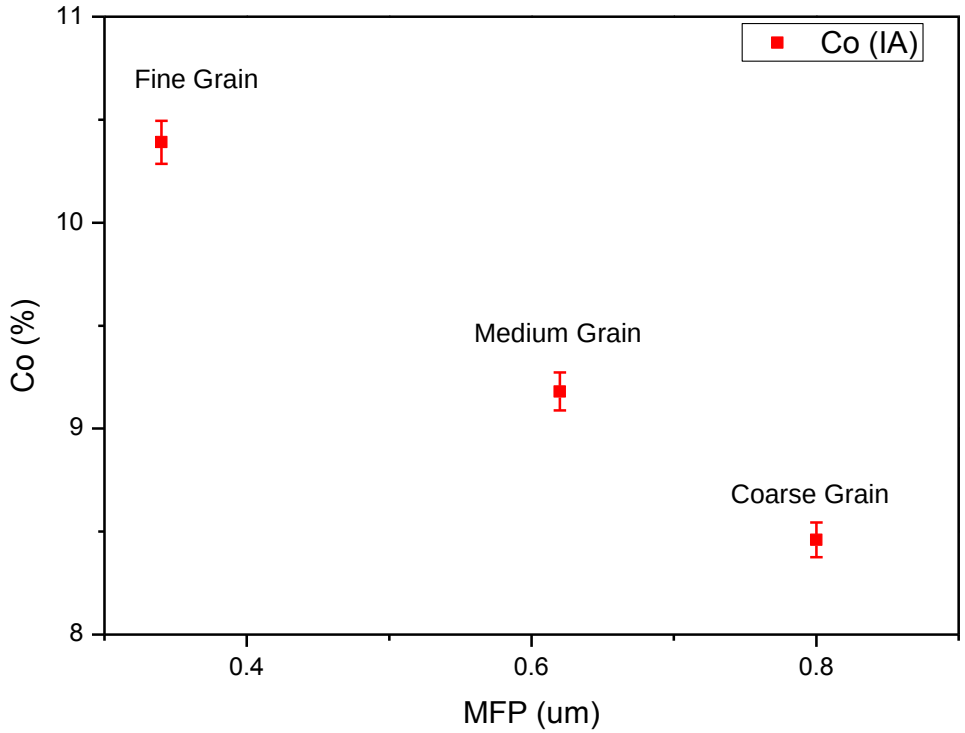


Figure 62: Relationship between MFP and Co (IA) content after sintering.

6.2.9. Magnetic Saturation versus Co content

The essence of magnetic saturation (moment) measurements can be explained as follows: WC-Co composites in general contain 5–20 wt% cobalt as a binder phase.

In PCD compacts, the metal phase contains both tungsten and carbon in solution. The magnetic saturation and moment values of cobalt are not affected by the presence of C, but by the excessive amount of W in PCD which decreases the fracture toughness.

The amount of the cobalt present in the PCD element may be correlated with the measured magnetic saturation of the PCD element as shown in Figure 63. A relatively larger magnetic saturation indicates relatively larger cobalt content in the PCD element. This is in agreement with what has been reported in the US patent by C. Hills and J. Qian [60].

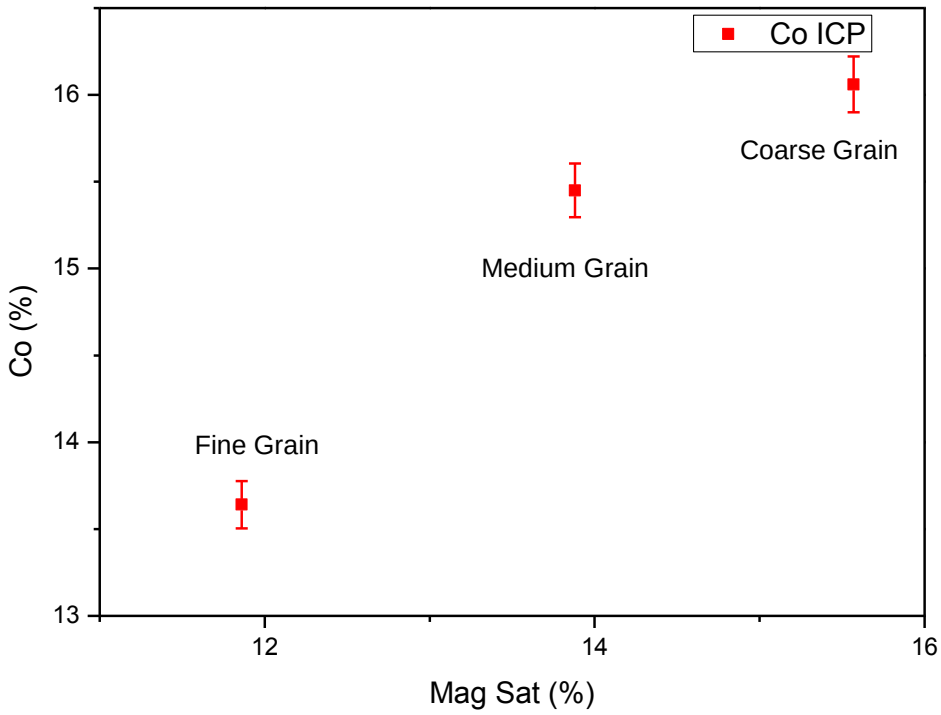


Figure 63: Relationship between magnetic saturation and ICP cobalt content after sintering.

The volume fraction of cobalt during LPS affected the magnetic properties. The saturation magnetization values revealed the presence of the Co phase which is ferromagnetic, which intensified as the cobalt content increased. It was also noticed that the presence of residual W and C in solution was a contributing factor to the lower values of magnetic saturation obtained though the C in solution did not show any effect on the decrease.

6.2.10. The XRD analysis

The phases were identified by comparing the resultant peaks with the International Centre for Diffraction Data (ICDD) database cards. The diamond peaks were located at 2θ = 51.6, and 90.4 respectively. The XRD analysis showed 2 major phases of diamond and Co, and minor phases of WC as shown in Figure 49. It was difficult to see the differences, as the diamond peak is in the same 2θ position of 51.6, there may be shifts in the Co peak position due to differences in the amount of dissolved WC but these will be so small and may not be within the resolution of the XRD. Comparison of the XRD peaks from the 3 diamond grain sizes did not show any significant differences at any 2Theta angles. This

means that for an accurate phase composition to be determined, Rietveld refinement must be employed. Without it no obvious conclusions can be drawn just by comparing the peaks. For the future research work, it is recommended that Rietveld refinement is carried out to have a precise amount of phases in PCD.

It is expected that when smaller diamond grain sizes are sintered together, the abrasion resistance of PCD increases. This in turn allows PCD to be prepared by EDM cutting and polished quite easily to obtain a high quality cutting element with minimum serrations.

6.2.11. Interrelationship of test results to microstructure of the material

After the HPHT sintering process, the PCD tables were removed from the WC-Co substrates by EDM cutting 1mm above the interface and used to derive the cobalt content through Archimedes principle. PCD table results listed in Table 13 show a higher cobalt content for a fine grain feed as indicated by the relatively higher magnetic saturation values. This is believed to be a result of the PCD tables formed by sintering diamond particles having a greater percentage of fine diamond particles. The PCD tables exhibit a lower coercivity indicative of a relatively greater mean free path between diamond grains, and this in turn indicates relatively less diamond-to-diamond bonding between the diamond grains.

Table 13: Summary of magnetic properties of PCD tables.

Feed	Average particle size	Sintering pressure GPA	Mag Sat (%)	Calculated Cobalt (%)	Coercivity (KA/m)
Fine Grain	4.50	5.5	15.56	16.31	14.03
Medium Grain	13.00	5.5	13.88	15.6	9.68
Coarse Grain	25.30	5.5	11.86	13.96	9.12

6.3. Structure and Magnetism

The relationship between the microstructural and magnetic properties investigations is shown in Figure 64, where *H*c has been plotted against the average diamond grain size. The most important feature is the decrease of Hc as the grain sizes increases to about 40 µm [85].

The magnetic properties of an assembly of small grains depend strongly on the local magnetic anisotropy energy and ferromagnetic exchange energy. For large grains the magnetization can follow with the easy magnetic direction since the single grains and domains can be formed within the grains. The magnetization process, thus, is determined by the magneto-crystalline anisotropy *K*1 of the crystallites.

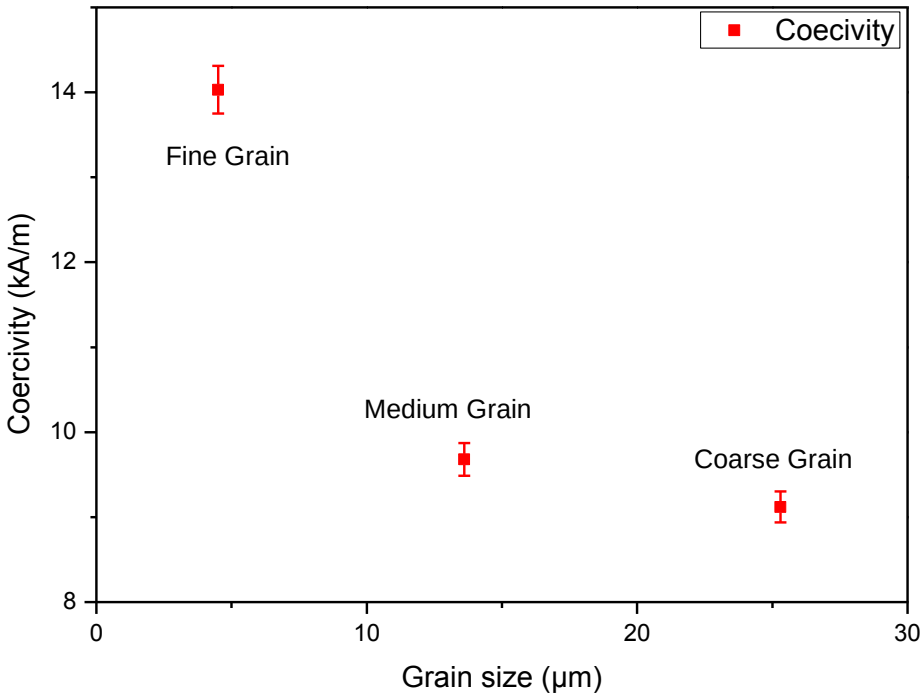


Figure 64: Relationship between coercivity and diamond grain size after sintering.

6.3.1. Correlation between the coercivity and the grain size measured by SEM image analysis.

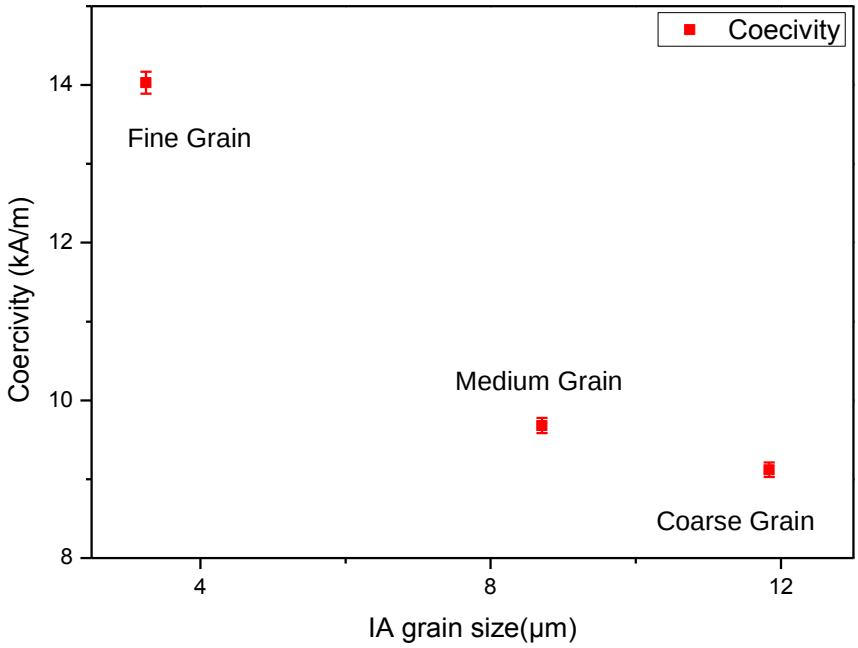


Figure 65: Relationship between coercivity and image analysis diamond grain size after sintering.

6.3.2. Relationship of microstructure to average grain size of diamond

The results of the diamond average size microstructural investigation that were determined by a linear intercept method, confirm that as the ferromagnetic metal phase content increases, a decrease in the grain size was observed. When the metal phase content is low, the distribution of the Co is not uniform and the diamond grain separation is by a small layer of the cobalt or they remain in contact with each other, resulting in an abnormal grain growth and a coarsening in the grain size. This is in agreement with what has been reported by Walid in the case of WC-Co hard metals [86].

When the cobalt phase content is high, it prevents the coalescence of the diamond particles, producing a grain structure which is more uniform and finer. In other words, there is a layer of the metal phase that separates all the diamond grains and subsequently produces grain growth that is normal and as a result, as shown in Figure 66, the finer diamond grain size has higher content of cobalt and the opposite holds for the coarse diamond grains. The metal phase content has a significant influence on the diamond

particle size. Therefore, a decrease in the grain size of diamond shows an increase in metal phase content.

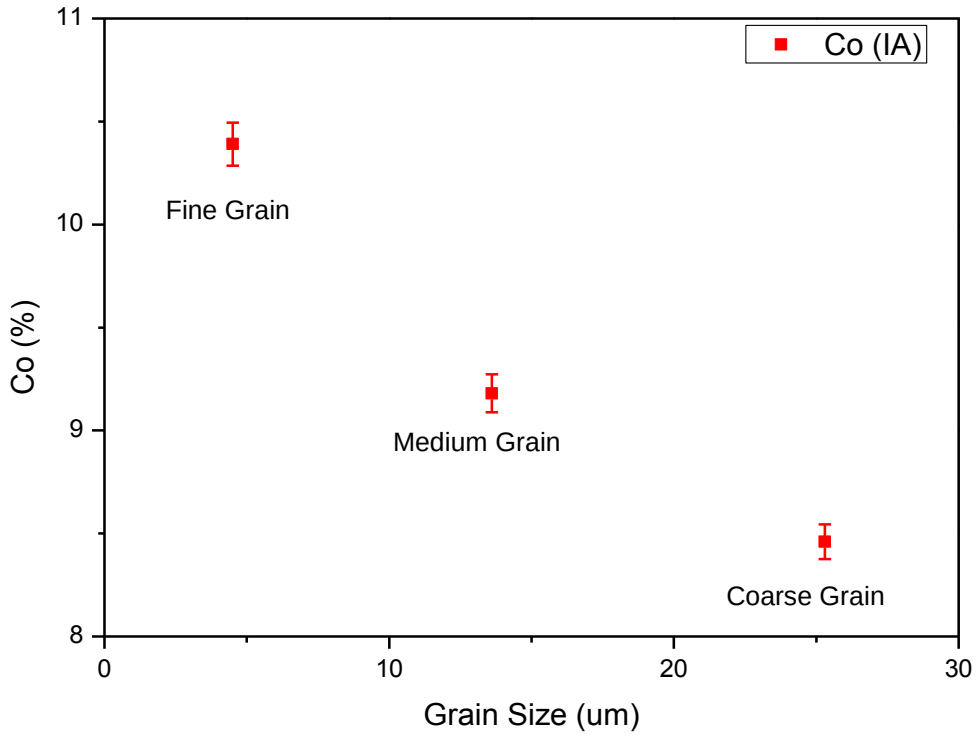


Figure 66: The relationship between cobalt calculated by IA and diamond grain size after sintering.

One other aspect of microstructure to grain size relationship is that, a decrease in porosity of the diamond skeleton results from the increase in the content of metal phase is observed. These results are attributed to the system in the LPS; the system attempts to reduce the total surface, in which case is the main contributor to influence the densification in all stages of the LPS. The maximum densification is achievable through particle rearrangement and also influenced by different parameters, such as the amount of liquid present, the size of the diamond particles, the contact angle, and the solubility of the solid in the liquid. This has been addressed in section 2.5.2. of the literature review and the same applies in the case of cemented carbide hard-metals as shown in Figure 67.

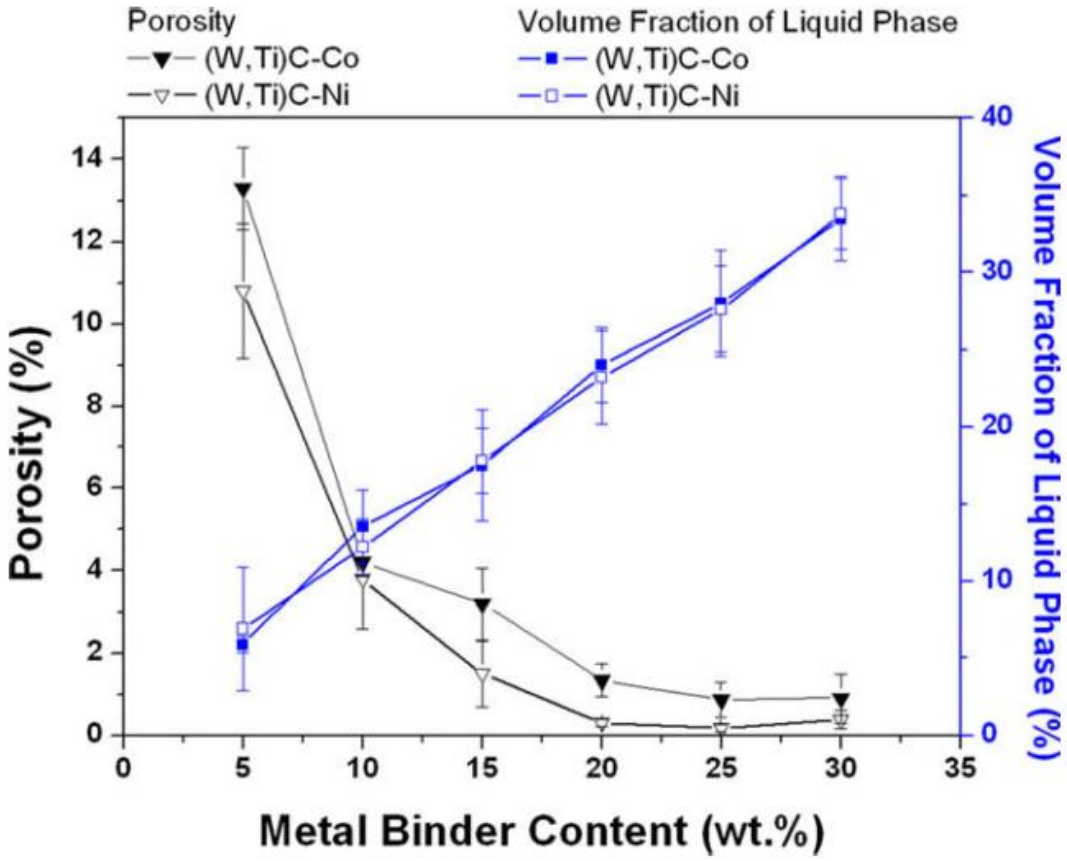


Figure 67: Influence of the composition of the metal binder on the porosity and the volume fraction of the binder of the (W,Ti)C–Co and (W,Ti)C–Ni cemented carbides [86].

6.3.3. Magnetic coercivity vs cobalt content

Figure 68 shows the effect of the cobalt content on the coercivity measurements. Increasing the metal phase content decreases the coercivity. As the sinterability of PCD increases, there is a decrease in porosity, which in turn decreases the particle–particle interactions and reducing the materials coercivity.

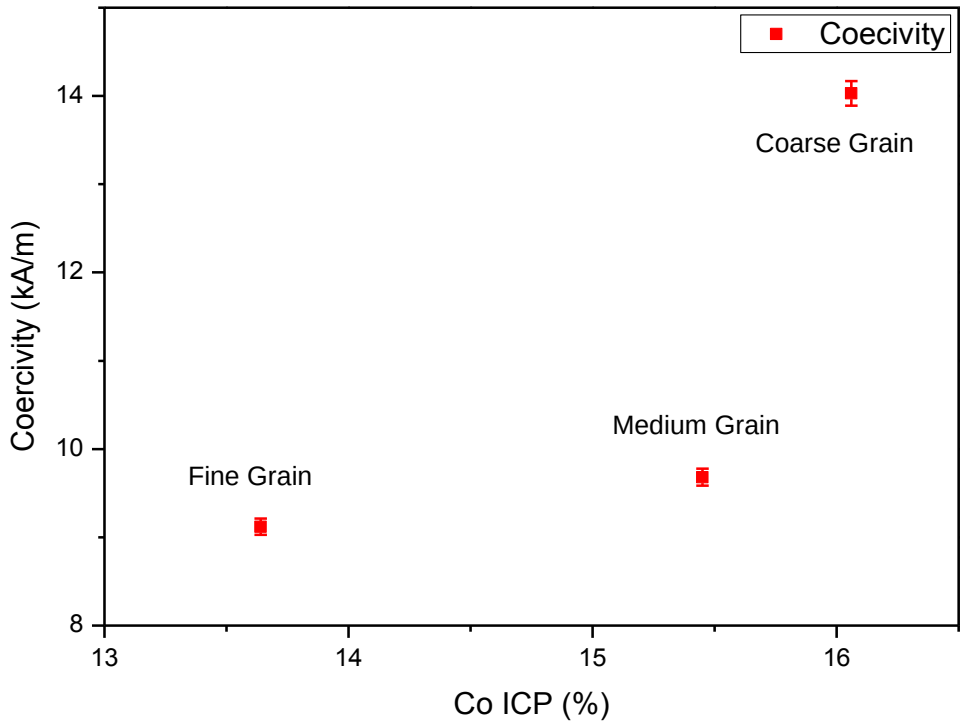


Figure 68: Relationship between coercivity and cobalt content from ICP after sintering.

6.3.4. Image Analysis results

The image analysis results shown in Table 8 show that the starting diamond grain size play a major role when cobalt is infiltrated into PCD from the substrate in the sense that coarse diamond grain PCD has less cobalt area due to the larger mean free path between diamond grains. The fine diamond grains show the most cobalt content infiltrated. These results show correlation with the magnetic properties results in the sense that the coarse grain diamond table has less cobalt content and therefore show less percentage of magnetic saturation which is the only ferromagnetic phase in PDC. For a good comparison, image analysis cobalt content in vol% was converted to wt% and this calculation shows that image analysis over estimates the cobalt content by a significant amount. This was due to the interaction volume from the 15kv beam of electrons used in SEM when imaging samples. Literature review explains this further in section 2.13.4.

Due to the less porosity in fine grain diamond, densification is rapidly achieved. There is however small differences in density measurements derived by Archimedes' immersion

density principle, and this show that magnetic properties are insignificantly affected by the density of the three diamond sizes.

The questions asked in Chapter 3 were thus answered by this investigation and confirmed by the correlation of results obtained after material characterisation. It was shown by image analysis that changing the grain size of the starting diamond powder changes the microstructure of the material and its properties, and these are related to the magnetic properties and mechanical properties.

CHAPTER 7 CONCLUSION

The microstructure, mechanical and magnetic properties of PCD compacts have been investigated. The PCD compacts were sintered with the help of the liquid phase cobalt base using HPHT presses at 5.5 GPa and 1450 °C. The high temperature is used because it is sufficient to melt cobalt during sintering, which makes it easier for diamond-diamond particles to bond. The results showed that, a decrease in diamond grain size yields increased volume fraction of liquid phase and also promote reduction in porosity there by increasing the metal phase content and the material density.

The magnetic saturation of the PCD compacts increases as the cobalt phase content increases, indicating the existence of the ferromagnetic nature of the materials. The PCD compacts show a very low induction saturation with nonmagnetic behaviour as well as, the magnetic coercivity measurements shows that as the porosity increases, coercivity increases.

The image analysis can be used to determine the mean grain size of solid-state sintered and sintered WC–Co and correlated them with magnetic coercivity, which is related to the WC–Co interfacial area.

The diamond powders cold compaction shows more densification of coarser powders due to larger pore sizes than the case at a given pressure with the finer powders. Conversely, the densification of the hot compaction stage is influenced by crushing and the reordering of the crushed particles up to 700 °C. If the temperature is exceeded, plastic deformation occurs while densification continues to take place. The temperature and pressure are the main drivers behind the plastic deformation. The rate at which the pore sizes reduce is much quicker for coarser pores than it is for the finer pores due to larger distance between two diamond particles.

The hardness as well as the wear resistance of the sintered diamond compacts are influenced by the levels of graphitization and plastic deformation that take place during hot compaction stage. At the time when both plastic deformation and graphitization are taking place the material properties are more sensitive to the plastic deformation until the bulk diamond grains graphitization begins.

The pressure gradients during synthesis influenced by the rate of Infiltration of cobalt binder from the substrate produced when the external load is applied.

In the vicinity of an *H* field, the magnetic moments in a material have a tendency to align with the field and to reinforce it by virtue of their magnetic fields. The magnetic saturation is resolved just by the composition of the material.

Coercivity (H_c), is measured from the hysteresis curve, is structural sensitive as opposed to its composition. For instance, a low estimation of coercivity relates to the simple domain walls movement when the magnetic field changes magnitude and direction. The structural defects, for example, particles of a non-magnetic phase or voids in the magnetic material have a tendency to limit the movement of domain walls, and along these lines increase the coercivity as do finer particles.

Hysteresis is identified with simplicity at which the magnetic domain wall move by hindering domain wall movement. The coercivity and susceptibility are enhanced, such that a large external field is needed for demagnetization. The microstructure of the material is related to its physical and characteristics. The grain size of diamond was varied into three sizes to evaluate the effect it had on magnetic properties.

IA results show that diamond starting particle size has significant influence on the Co phase microstructure and magnetic properties. It was also found that magnetic saturation measurements are independent of the shape and size of the specimen. For coarse grained diamond, the coercive force decreases. Cobalt content increases in PCD with decreasing grain size and so does the magnetic saturation.

A clear correlation between the metal phase content, magnetic saturation, cobalt mean free path and coercivity exists. The XRD did not detect HCP cobalt but only the FCC cobalt phase was present in Syndrill PCD disks. This could be due to the significant amount of WC in the PCD which is present in solid solution after cooling from the sintering temperature.

The EDS results have shown significant differences in metal content as a result of changing the size of the starting diamond powder.

It is shown that x-ray diffraction and x-ray fluorescence methods can be used in a quantitative manner for the characterisation of polycrystalline diamond products. However, as in all analytical methods, sample preparation is important in the generation of meaningful data. In addition to the need to carefully prepare the samples prior to analysis, it has been observed that the analysis results are dependent upon the diamond grain size. It should be possible to develop correlations between the composition of the final PCD layer matrix and the process conditions used in the synthesis process.

The change in diamond grain size significantly affect the cobalt content infiltrated into the PCD and therefore significantly affected the magnetic saturation and coercivity. As the diamond grain size is increased, the magnetic saturation and cobalt content decrease affecting the wear resistance of the PCD. The coercivity however increases with decreasing diamond grain size.

Recommendation

When the sintered nano-crystalline WC–Co powders are characterized in future, they should include the magnetic coercivity measurements, hardness and toughness data for the development of models to link microstructure and properties at the nano-scale.

REFERENCES

[1] G. Davies, “1 Basic Properties of Diamond : Phonon Spectra , Thermal Properties , Band Structure,” 2009.

[2] R. H. Wentorf, R. C. Devries, and F. P. Bundy, “Sintered superhard materials.,” *Science*, vol. 208, no. 4446, pp. 873–80, 1980.

[3] L. Jaworska, M. Szutkowska, P. Klimczyk, M. Sitarz, M. Bucko, P. Rutkowski, P. Figiel, and J. Lojewska, “Int . Journal of Refractory Metals and Hard Materials Oxidation , graphitization and thermal resistance of PCD materials with the various bonding phases of up to 800 ° C,” *RMHM*, vol. 45, pp. 109–116, 2014.

[4] J. Ewald, N. Dubrovinskaia, J. Henoch, and I. Sigalas, “Thermally stable polycrystalline diamond sintered with calcium carbonate,” vol. 16, pp. 1929–1935, 2007.

[5] T. Caetano, S. Bobrovnitchii, D. Skury, A. Lucia, P. Junior, M. Soares, and M. Universidade, “Liquid phase diamond composite sintering,” p. 40102601, 2008.

[6] A. M. Technology, “Diamond – Ceramic Bonding Phase Composites for Application in Cutting Tools,” pp. 131–137, 2011.

[7] F. Bellin, A. Dourfaye, W. King, M. Thigpen, and V. International, “The current state of PDC bit technology,” no. September, 2010.

[8] “3-D FEA OF HARD TURNING : INVESTIGATION OF PCBN CUTTING TOOL MICRO-GEOMETRY EFFECTS Yi ğ it Karpat and Tu ğ rul Özel Department of Industrial and Systems Engineering Transactions of NAMRI / SME Transactions of NAMRI / SME,” vol. 35, pp. 1–8, 2007.

[9] H. Sumiya and T. Irifune, “Indentation hardness of nano-polycrystalline diamond prepared from graphite by direct conversion,” *Diam. Relat. Mater.*, vol. 13, no. 10, pp. 1771–1776, 2004.

[10] V. P. Astakhov, *Science and Technology of Advanced Operations Science and Technology of*. CRC Press, 2014.

[11] R. Riedel, *Handbook of Ceranic Hard Materials*. 2000.

[12] E. Abele and Æ. B. Schramm, “Using PCD for machining CGI with a CO 2 coolant system,” pp. 165–169, 2008.

[13] Y. L. German, Randall M, “Grain Agglomeration in Liquid Phase Sintering,” *J. Mater. Synth. Process.*, vol. 4, no. 1, pp. 23–24, 1996.

[14] H. Search, C. Journals, A. Contact, M. Iopscience, and I. P. Address, “The mechanical and strength properties of diamond,” vol. 126505.

[15] H. Samkelo and L. Sithebe, “THE PREPARATION AND CHARACTERISTICS OF cBN CERAMICS WITH AL-BASED BINDER by,” 2007.

[16] R. J. Sigalas, I, Caveney, “Diamond Materials and their Applications,” in *Handbook of Ceramic Hard Materials*, 2000, pp. 485–486.

[17] F. P. Bundy, “DIAGRAM FOR CARBON ; UPDATED,” vol. 34, no. 2, pp. 141–153, 1996.

[18] F. P. Bundy, “Proceedings of the IV Advanced Ceramics and Applications Conference,” *J. Geophys*, vol. 85(B12), no. 6930, 1980.

[19] H. Sumiya and T. Irifune, “Synthesis of High-Purity Nano-Polycrystalline Diamond and Its Characterization,” no. 3, pp. 52–59, 2000.

[20] J. Robertson, “Properties of diamond-like carbon,” *Surf. Coatings Technol.*, vol. 50, no. 3, pp. 185–203, 1992.

[21] A.L. Ruoff, “High Pressure Science and Technology,” in *High Pressure Science and Technology*, 1979, p. 525.

[22] J. E. Field, *The Properties of Natural and Synthetic Diamond*. 1992.

[23] A. Ersoy and M. D. Waller, “Drilling Detritus and the Operating Parameters of Thermally Stable PDC Core Bits,” *Int. J. Rock Mech. Min. Sci.*, vol. 34, no. 7, pp. 1109–1123, 1997.

[24] J. N. Boland and X. S. Li, “Microstructural Characterisation and Wear Behaviour of Diamond Composite Materials,” pp. 1390–1419, 2010.

[25] A. Lammer, “Mechanical properties of polycrystalline diamonds,” vol. 4, no. November, pp. 949–955, 1988.

[26] D. Blanks, “The History and Impact of Synthetic Diamond Cutters and Diamond Enhanced Inserts on the Oil and Gas Industry,” no. Figure 1, 1976.

[27] M. P. D’Evelyn and K. Zgonc, “Elastic properties of PCBN and diamond by dynamic resonance measurements,” *Diam. Relat. Mater.*, vol. 6, no. 96, pp. 812–816, 1997.

[28] K. Uehara and S. Yamaya, “High pressure sintering of diamond by cobalt infiltration,” *Science and Technology of New Diamond*. pp. 203–209, 1990.

[29] “Private Communication (Since no one else can view this).”

[30] A. L. Mckie, “CARBON ENRICHED THERMAL SPRAYED HARD METAL COATINGS USED IN PCD SINTERING,” 2012.

[31] R. M. German, *Æ*. P. Suri, and *Æ*. S. Jin, “Review : liquid phase sintering,” pp. 1–39, 2009.

[32] Bruce A. Averill, “Solids,” in *Principles of General Chemistry*, vol. 1, 2012, p. 1512.

[33] O.-H. Kwon, *Liquid-Phase Sintering, Advanced Ceramics, Norton company*. .

[34] G. C. Kuczynski, “Physics and chemistry of sintering,” *Adv. Colloid Interface Sci.*, vol. 3, no. 3, pp. 275–330, 1972.

[35] D. Miess and G. Rai, “Fracture toughness and thermal resistance of polycrystalline diamond compacts,” *Mater. Sci. Eng. A*, vol. 209, no. 1–2, pp. 270–276, 1996.

[36] L. Froschauer and R. M. Fulrath, “Direct observation of liquid-phase sintering in the system tungsten carbide-cobalt,” *J. Mater. Sci.*, vol. 11, no. 1, pp. 142–149, 1976.

[37] S. P. and W. A. K. V. Smolej, “Rearrangement during Liquid Phase Sintering of Large Particles,” *Powder Met. Int.*, vol. 14, pp. 126–128, 1981.

[38] A. Petersson, “Cemented Carbide Sintering : Constitutive Relations and Microstructural Evolution,” 2004.

[39] I. H. Buckle, “Progress in Micro-identation Hardness Testing,” *Mater. Revis.*, no. 4, pp. 49–100, 1959.

[40] R. P. Herber, W. D. Schubert, and B. Lux, “Hardmetals with ‘rounded’ WC grains,” *Int. J. Refract. Met. Hard Mater.*, vol. 24, no. 5, pp. 360–364, 2006.

[41] X. Wang, Z. Z. Fang, and H. Y. Sohn, “Grain growth during the early stage of sintering of

nanosized WC-Co powder," *Int. J. Refract. Met. Hard Mater.*, vol. 26, no. 3, pp. 232–241, 2008.

[42] R. M. German, *Liquid Phase Sintering*. 1985.

[43] and T. I. H Sumiya, "Microstructure and Mechanical Properties of High-Hardness Nano-Polycrystalline Diamonds," *SEI Tech. Rev.*, vol. 66, pp. 85 – 91, 2008.

[44] Z. D. Sha, P. S. Branicio, V. Sorkin, Q. X. Pei, and Y. W. Zhang, "Effects of grain size and temperature on mechanical and failure properties of ultrananocrystalline diamond," *Diam. Relat. Mater.*, vol. 20, no. 10, pp. 1303–1309, 2011.

[45] R. M. German, *Sintering Theory and Practice*. John Wiler & Sons, 1996.

[46] J. Weidow, *Effect of metal and cubic carbide additions on interface chemistry , phase composition and grain growth in WC-Co based cemented carbides Department of Applied Physics*. 2010.

[47] S. Ozbayraktar, "Mechanism of Liquid Phase Sintering of PCD," 1997.

[48] A. L. Mckie, "Mechanical Properties of cBN-Al Composite Materials Dependence on Grain Size of cBN and Binder Content," no. October, 2009.

[49] M. Naidoo, "Preparation of (Ti , Ta)(C , N) by Mechanical Alloying," no. August, 2012.

[50] J. Trefil, *The Sciences: An integrated approach*, 2nd ed. New York: John Wiley & Sons, 2000.

[51] M. Properties, "Magnetic Properties," pp. 19–56.

[52] B. R. M., *Ferromagnetism*. New York/Piscataway: Wiley-IEEE Press, 1993.

[53] P.-G. de Gennes, "Effects of Double Exchange in Magnetic Crystals," *Phys. Rev. 118*, vol. 114, 1960.

[54] S.B Luyckx, "The preparation and properties of hardmetals," 1997.

[55] R. S. Iskhakov, G. I. Frolov, V. S. Zhigalov, and D. E. Prokof, "Magnetic Interaction between Superparamagnetic Particles in Nanogranular Cobalt Films," vol. 30, no. 8, pp. 687–689, 2004.

[56] S. J. Park, K. Cowan, J. L. Johnson, and R. M. German, "Grain size measurement methods and models for nanograined WC – Co," vol. 26, pp. 152–163, 2008.

[57] B. Wittmann, W. D. Schubert, and B. Lux, "WC grain growth and grain growth inhibition in nickel and iron binder hardmetals," *Int. J. Refract. Met. Hard Mater.*, vol. 20, no. 1, pp. 51–60, 2002.

[58] B. R. and E. A. Almond, *Recent Advances in Hardmetal Production*. Shrewsbury, 1979.

[59] P. Information, "Koerzimat ® 1.097 hcj," pp. 1–12.

[60] J. Qian, C. Hills, and J. Wiggins, "(19) United States (12)," vol. 1, no. 19, 2011.

[61] "What is the physical difference between magnetic flux density B and magnetic field strength H." [Online]. Available: https://www.quora.com/.

[62] "Magnetism." [Online]. Available: https://www.nde-ed.org/EducationResources/HighSchool/Magnetism/magneticdomain.htm.

[63] M. Domain, "No Title." [Online]. Available: https://en.wikipedia.org/wiki/Magnetic_domain.

[64] C. d'information du Cobalt, *Cobalt Monograph*. 1960.

[65] Cobalt, “No Title.” [Online]. Available: https://en.wikipedia.org/wiki/Cobalt.

[66] H. J. Scussel, “Friction and Wear of Cemented Carbides,” *ASM*, vol. 18, pp. 795–800, 1992.

[67] C. Wu, “Low Energy-Consumption Industrial Production of Ultra-Fine Spherical Cobalt Powders.”

[68] W. Betteridge, *Cobalt and its Alloys*. New York: John Wiley and Sons, 1982.

[69] G. . Upadhyaya, *Cemented Tungsten Carbide Production*. 1998.

[70] J. Y. Huang, Y. K. Wu, and H. Q. Ye, “Allotropic transformation of cobalt induced by ball milling,” *Acta Mater.*, vol. 44, no. 3, pp. 1201–1209, 1996.

[71] V. A. S. V. M. Schastlivtsev, Yu. V. Khlebnikova, T. I. Tabatchikova, D. P. Rodionov, “Formation of a structure in cobalt single crystals at the β→ α transformation,” *Dokl. Phys.*, vol. 54, no. 1, pp. 21–24, 2009.

[72] M. J. W. and L. C. S.B. Luyckx, D.J. Whitefield, “The Development of WC-VC-Co Hard Metal: A Review of Past Work and New Results,” *Proc. Int. Con. Powd. Met.*, vol. 1, pp. 85–91, 1998.

[73] K. J. A. Brookes, *Hardmetal and other Hard Materials*. Hertfordshire: International Carbide Data, 1975.

[74] L. G. C Salvatore, A Rodolfo, *Electromagnetic shielding*. New Jersey: John Wiley & Sons, 2008.

[75] A. A. O. and T. J. Davies, “Proposed selection rules for suitable binders in cemented hard metals with possible applications for improving ductility in intermetallics,” *J. Mater. Sci.*, vol. 27, pp. 5382–5388, 1992.

[76] G. W. and G. L. Dunlop, “Phase transformations in the binder phase of Co-W-C cemented carbides,” *Proc. 1st Int. Conf. Sci. Hard Mater.*, pp. 311–325, 1981.

[77] H. E. Exner, “Qualitative and quantitative interpretation of microstructures in cemented carbides,” *Proc1st Int. Conf. Sci. hard Mater.*, pp. 311–325, 1981.

[78] K. J. and T. . Fischer, “Microstructure, hardness and toughness of nanostructured and conventional WC-Co composites,” *Nanostructured Mater.*, vol. 10, no. 5, pp. 875–891, 1998.

[79] “Scanning Electron Microscope.” [Online]. Available: https://en.wikipedia.org/wiki/Scanning_electron_microscope.

[80] E. Goldstein, G. I.; Newbury, D. E.; Echlin, P.; Joy, D. C.; Fiori, C.; Lifshin, *Scanning electron microscopy and x-ray microanalysis*. New York: Plenum Press, 1981.

[81] “D2 Phaser - Overview, X-ray diffractometer on desktop.,” 2017. .

[82] A. Monshi, “Modified Scherrer Equation to Estimate More Accurately Nano-Crystallite Size Using XRD,” *World J. Nano Sci. Eng.*, vol. 2, no. 3, pp. 154–160, 2012.

[83] D. Jianxin, Z. Hui, W. Ze, and L. Aihua, “Int . Journal of Refractory Metals and Hard Materials Friction and wear behavior of polycrystalline diamond at temperatures up to 700 ° C,” vol. 29, pp. 631–638, 2011.

[84] K. E. Bertagnolli, C. Hills, J. Qian, J. Wiggins, and M. Vail, “Polycrystalline Diamond,” 12/846,604, 2010.

[85] G. Herzer, V. Gmbh, D.- Hanau, and F. R. Germany, “GRAIN S I Z E DEPENDENCE OF

COERCIVITY AND PERMEABILITY," vol. 26, no. 5, pp. 1397–1402, 1990.

[86] W. M. Daoush, K. H. Lee, H. S. Park, and S. H. Hong, "Int . Journal of Refractory Metals & Hard Materials Effect of liquid phase composition on the microstructure and properties of (W , Ti) C cemented carbide cutting tools," *Int. J. Refract. Met. Hard Mater.*, vol. 27, no. 1, pp. 83–89, 2009.

APPENDICES:

APPENDIX A

A1. PRESENTATIONS RESULTING FROM THIS DISSERTATION

T.T Ngwekhulu, S.R Naidoo, I Sigalas. Effect of diamond grain size on magnetic properties of cobalt phase in PCD compacts, DST-NRF Centre of Excellence for Strong Materials student presentation workshop hosted by the University of Witwatersrand, 16th April 2014, Johannesburg, South Africa. *Poster presentation*.

T.T Ngwekhulu, S.R Naidoo, I Sigalas. Effect of diamond grain size on magnetic properties of cobalt phase in PCD compacts, The 59th Annual Conference of the South African Institute of Physics hosted by the University of Johannesburg, 07 - 11 July 2014, Aucklandpark, Johannesburg, South Africa. *Poster presentation*.

A.2. Calculation of the densities of PCD disks of fine grain diamond

Dry Mass = 0.491 g

Wet Mass = 0.371 g

Mass Different = 0.120 g

$$\textit{Density}_{(PCD)} = \frac{Mass(dry)}{Mass(dry) - Mass(wet)}$$

$$= \frac{0.491}{0.491 - 0.371)}$$

$$= 4.0917\ g.cm^{-3}$$

A.3. Calculation of the metal content of PCD disks of fine grain diamond

$$\% \text{ Cobalt Content} = \frac{Density\ (pcd) - Density\ (diamomd)}{Density\ (diamond)}$$

$$= \frac{4.0917 - 3.52}{3.52}$$

$$= 16.24\%$$

Similarly, the other eleven values of densities and metal content for Fine, Medium, and Coarse grain diamond were calculated as 16.24%. For metal content calculations, the density of diamond used was 3.52 g.cm^{-3}

A.4. Image Analysis results of sintered PCD disks of the same composition

IMAGE ANALYSIS RESULTS SHEET Sheet Rev. Rev12b RSN R3.0 (Saltikov Allowed)

14ZA0079 **Prepared by** Maggie

Sample name: Fine Grain **Date:** 20140206

Diamond Grain Size [µm]

Mean	stdev	d10	d50	d75	d90	Maximum
3.25	1.11	1.80	3.24	4.08	4.80	5.88

Binder Pool Size [µm]

Mean	stdev	d10	d50	d75	d90	Maximum
1.30	0.64	0.54	1.20	1.74	2.16	2.94

Diamond Area [%Area]				Binder Area [%Area]			
Mean	stdev	Lower (95%)	Upper (95%)	Mean	stdev	Lower (95%)	Upper (95%)
89.61	0.48	89.36	89.87	10.39	0.48	10.13	10.64

Diamond MFP [µm]

Mean	stdev	d10	d50	d75	d90	Maximum
2.54	3.32	0.03	1.19	3.75	6.91	30.34

Binder MFP [µm]

Mean	stdev	d10	d50	d75	d90	Maximum
0.34	0.37	0.03	0.22	0.47	0.81	3.50

Diamond Contiguity [%Area]

Mean	stdev	Lower (95%)	Upper (95%)
63.82	1.96	62.77	64.86

WC Phase Area [%Area]

Mean	stdev	Lower (95%)	Upper (95%)
0.34	0.13	0.26	0.41

IMAGE ANALYSIS RESULTS SHEET

Sheet Rev: Rev12b RSN R3.0 (Saltikov Allowed)

14ZA0079

Prepared by Maggie

Sample name: Medium Grain

Date: 20140206

Diamond Grain Size [µm]

Mean	stdev	d10	d50	d75	d90	Maximum
8.71	4.36	3.52	7.92	11.88	15.40	20.68

Binder Pool Size [µm]

Mean	stdev	d10	d50	d75	d90	Maximum
1.91	0.99	0.80	1.80	2.40	3.30	4.90

Diamond Area [%Area]

Mean	stdev	Lower (95%)	Upper (95%)
90.82	0.34	90.64	91.00

Binder Area [%Area]

Mean	stdev	Lower (95%)	Upper (95%)
9.18	0.34	9.00	9.36

Diamond MFP [µm]

Mean	stdev	d10	d50	d75	d90	Maximum
5.66	6.80	0.38	3.02	7.92	14.81	65.66

Binder MFP [µm]

Mean	stdev	d10	d50	d75	d90	Maximum
0.62	0.53	0.09	0.47	0.85	1.32	5.19

Diamond Contiguity [%Area]

Mean	stdev	Lower (95%)	Upper (95%)
62.27	0.82	61.83	62.71

WC Phase Area [%Area]

Mean	stdev	Lower (95%)	Upper (95%)
0.37	0.06	0.34	0.40

IMAGE ANALYSIS RESULTS SHEET

Sheet Rev. Rev12b RSN R3.0 (Saltikov Allowed)

13ZA2079

Prepared by Maggie

Sample name: Coarse Grain

Date: 20140225

Diamond Grain Size [µm]

Mean	stdev	d10	d50	d75	d90	Maximum
11.84	5.64	4.80	11.04	15.84	20.16	23.52

Binder Pool Size [µm]

Mean	stdev	d10	d50	d75	d90	Maximum
2.79	1.44	0.98	2.66	3.78	4.90	6.58

Diamond Area [%Area]

Mean	stdev	Lower (95%)	Upper (95%)
91.54	0.47	91.29	91.79

Binder Area [%Area]

Mean	stdev	Lower (95%)	Upper (95%)
8.46	0.47	8.21	8.71

Diamond MFP [µm]

Mean	stdev	d10	d50	d75	d90	Maximum
7.56	9.31	0.38	3.77	10.85	20.19	81.23

Binder MFP [µm]

Mean	stdev	d10	d50	d75	d90	Maximum
0.80	0.74	0.09	0.57	1.04	1.70	10.28

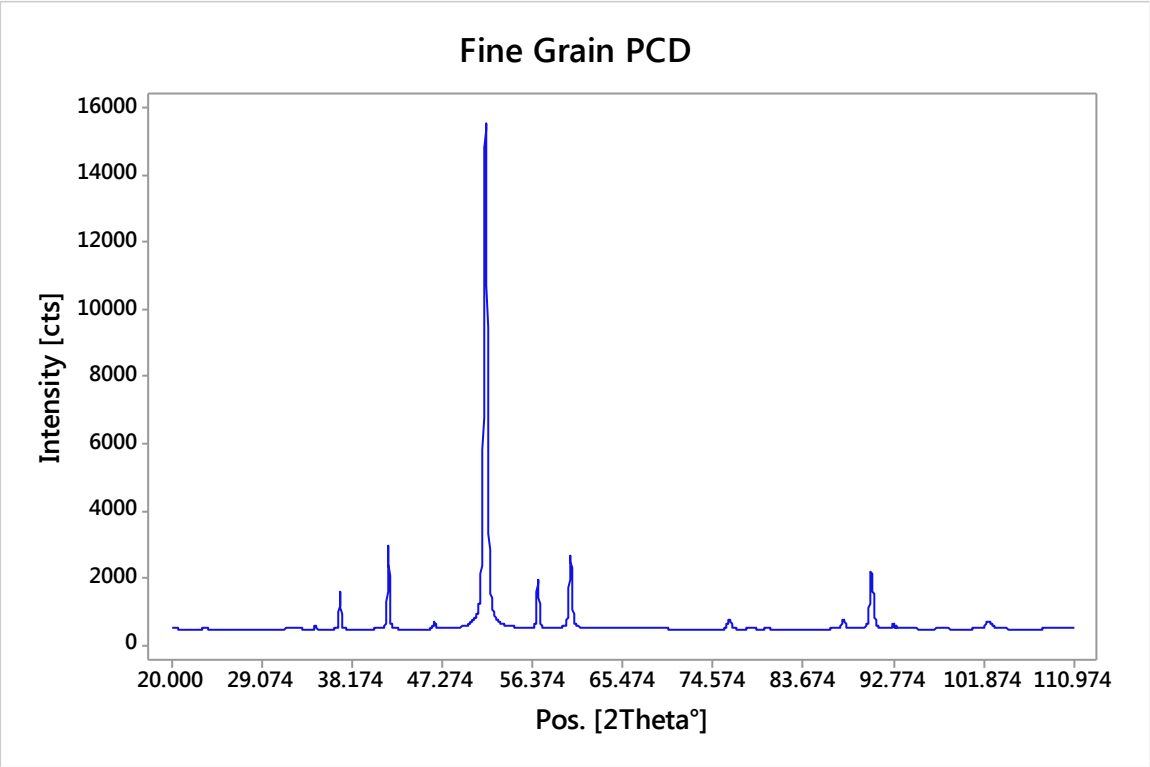
Diamond Contiguity [%Area]

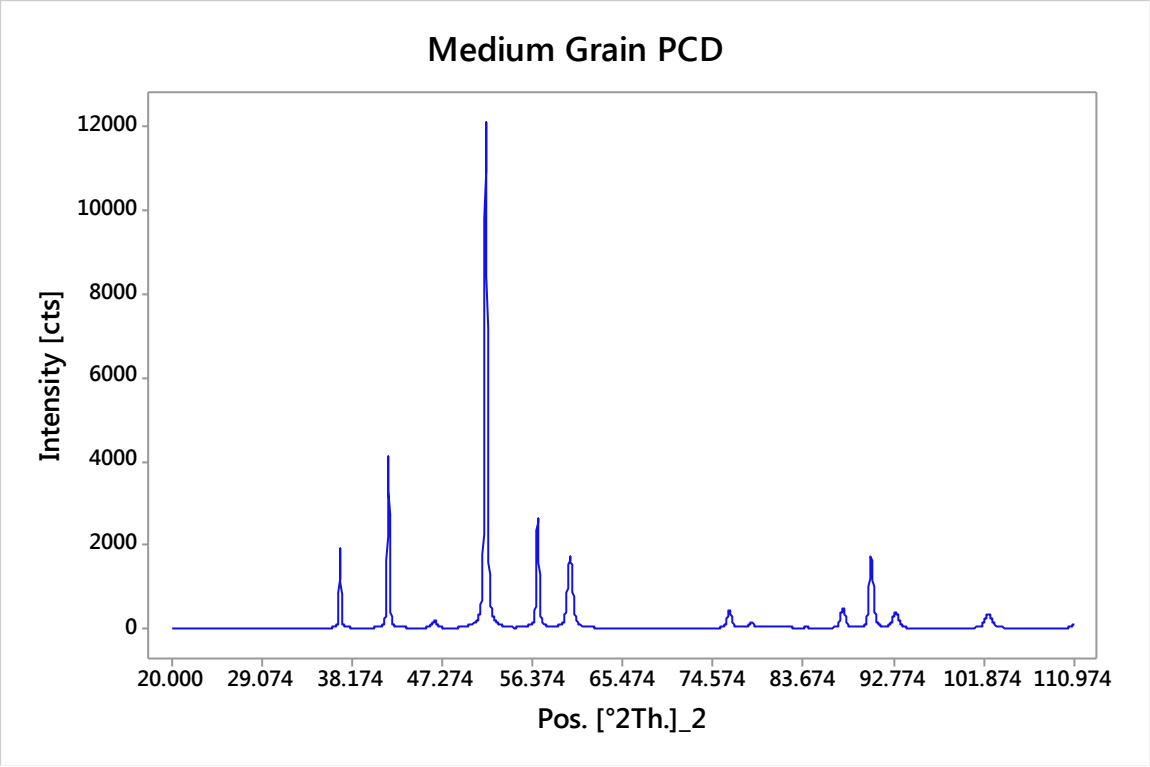
Mean	stdev	Lower (95%)	Upper (95%)
66.55	1.42	65.79	67.30

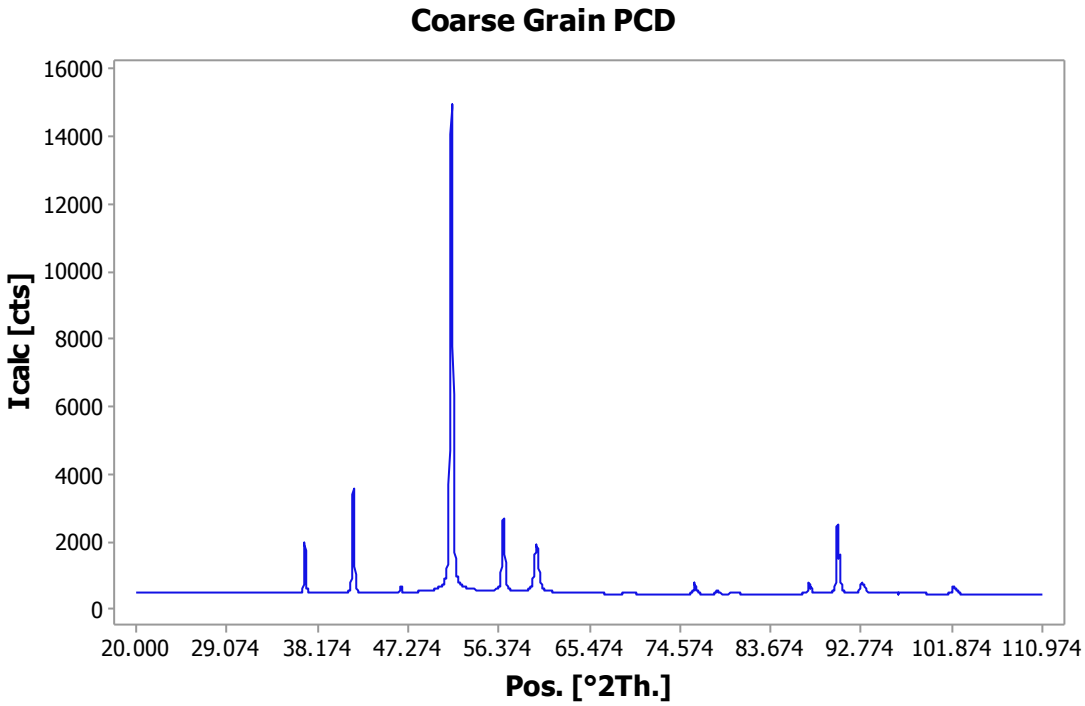
WC Phase Area [%Area]

Mean	stdev	Lower (95%)	Upper (95%)
0.37	0.07	0.33	0.40

A.5 XRD Spectrums






Coarse Grain PCD
16000
14000
12000
10000
8000
6000
4000
2000
0
Icalc [cts]
20.000
29.074
38.174
47.274
56.374
65.474
74.574
83.674
92.774
101.874
110.974
Pos. [°2Th.]